Strojniški vestnik
Journal of Mechanical Engineering

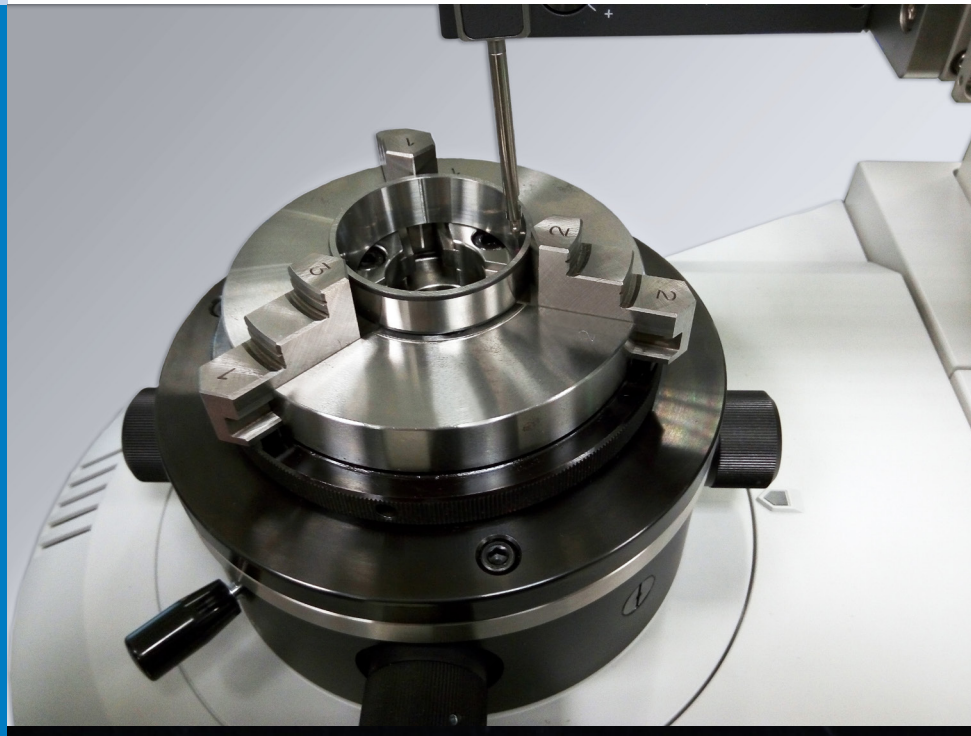

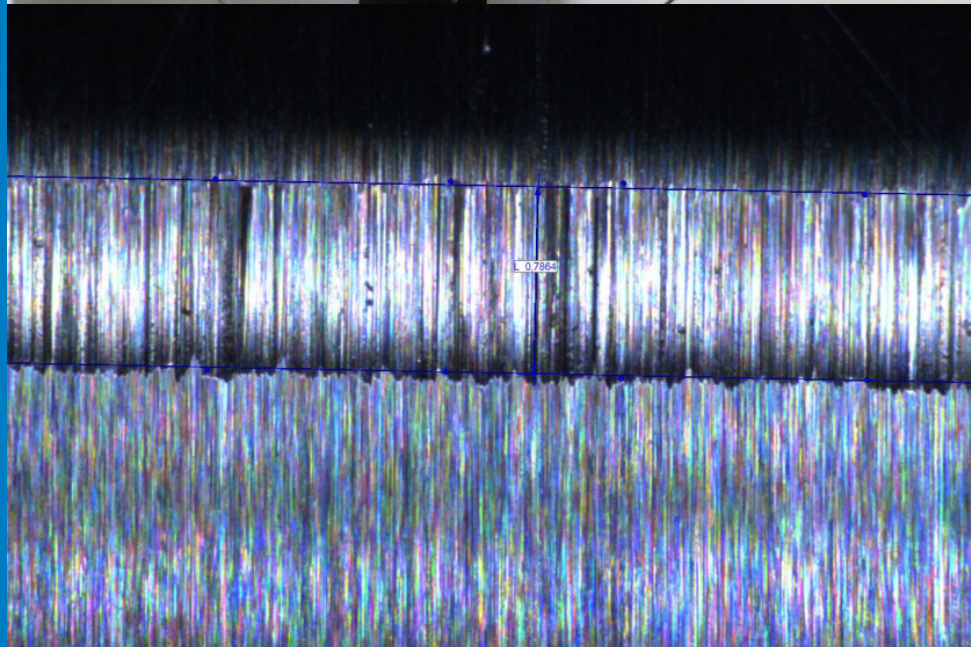

no. 1
year 2017
volume 63

Strojniški vestnik – Journal of Mechanical Engineering (SV-JME)

Aim and Scope

The international journal publishes original and (mini)review articles covering the concepts of materials science, mechanics, kinematics, thermodynamics, energy and environment, mechatronics and robotics, fluid mechanics, tribology, cybernetics, industrial engineering and structural analysis.

The journal follows new trends and progress proven practice in the mechanical engineering and also in the closely related sciences as are electrical, civil and process engineering, medicine, microbiology, ecology, agriculture, transport systems, aviation, and others, thus creating a unique forum for interdisciplinary or multidisciplinary dialogue.

The international conferences selected papers are welcome for publishing as a special issue of SV-JME with invited co-editor(s).

Editorial Office
University of Ljubljana, Faculty of Mechanical Engineering
SV-JME, Aškerčeva 6, SI-1000 Ljubljana, Slovenia
Phone: 386 (0)1 4771 137
Fax: 386 (0)1 2518 567
info@sv-jme.eu, http://www.sv-jme.eu

Print: Birografika Bori, d.o.o., printed in 300 copies

Founders and Publishers
University of Ljubljana, Faculty of Mechanical Engineering, Slovenia
University of Maribor, Faculty of Mechanical Engineering, Slovenia
Association of Mechanical Engineers of Slovenia
Chamber of Commerce and Industry of Slovenia, Metal Processing Industry Association

Cover:
Front cover shows the contact measurement of a manufacturing defect on a tapered roller bearing outer race with a high-quality Mahr MMQ 200 form measuring equipment. It capables of producing precise roundness measuring by its motorized probe, adjustable table, well-defined measuring axises and ergonomic control panel. Another image shows an optical measurement of the defect geometrical parametres by a Garant MM1-200 video measuring microscope with incremental measuring system.
Image Courtesy:
Laboratory of Diagnostics, Department of Mechanical Engineering, Faculty of Engineering, University of Debrecen, Hungary
Photo: Sándor Szabó

ISSN 0039-2480

General information
Strojniški vestnik – Journal of Mechanical Engineering is published in 11 issues per year (July and August is a double issue).

Institutional prices include print & online access: institutional subscription price and foreign subscription €100,00 (the price of a single issue is €10,00); general public subscription and student subscription €50,00 (the price of a single issue is €5,00). Prices are exclusive of tax. Delivery is included in the price. The recipient is responsible for paying any import duties or taxes. Legal title passes to the customer on dispatch by our distributor.

Single issues from current and recent volumes are available at the current single-issue price. To order the journal, please complete the form on our website. For submissions, subscriptions and all other information please visit: *http://en.sv-jme.eu/*.

You can advertise on the inner and outer side of the back cover of the journal. The authors of the published papers are invited to send photos or pictures with short explanation for cover content.

We would like to thank the reviewers who have taken part in the peer-review process.

The journal is subsidized by Slovenian Research Agency.

Strojniški vestnik - Journal of Mechanical Engineering is available on http://www.sv-jme.eu, where you access also to papers' supplements, such as simulations, etc.

Contents

Strojniški vestnik - Journal of Mechanical Engineering
volume 63, (2017), number 1
Ljubljana, January 2017
ISSN 0039-2480

Published monthly

Papers

Strojniški vestnik - Journal of Mechanical Engineering 63(2017)1, 3-14
DOI:10.5545/sv-jme.2016.3989
Original Scientific Paper
Received for review: 2016-08-24
Received revised form: 2016-11-02
Accepted for publication: 2016-11-18

Optimal Wavelet Selection for the Size Estimation of Manufacturing Defects of Tapered Roller Bearings with Vibration Measurement using Shannon Entropy Criteria

Krisztián Deák* – Tamás Mankovits – Imre Kocsis
University of Debrecen, Faculty of Engineering, Hungary

Fault diagnosis of bearings is essential in manufacturing to increase quality. Traditionally, fault diagnosis of tapered roller element bearings is performed by signal processing methods, which handle the nonstationary behaviour of the signal. The wavelet transform is an efficient tool for analysing the vibration signal of the bearings because it can detect the sudden changes and transient impulses in the signal caused by faults in the bearing elements. In this article, manufacturing faults on the outer ring of tapered roller bearings due to the grinding process in manufacturing are investigated. Nine different real values wavelets (Symlet-2, Symlet-5, Symlet-8, db02, db06, db10, db14, Meyer, and Morlet) are compared according to the Energy-to-Shannon-Entropy ratio criteria, and which is efficient for detecting the manufacturing faults is determined. Finally, experiments are carried out on a test rig for determining the geometrical size of the manufacturing faults with all wavelets directly from the vibration signature the result of db02, Symlet-5, and Morlet wavelets are presented. When modelling the bearing structure as an under-damped second-order mass-spring-damper mechanical system, its unit impulse response function is compared to the wavelets on the basis of their Energy-to-Shannon-Entropy ratio to determine the fault size from the vibration signal. The proposed technique has been successfully implemented for measuring defect widths. The maximum deviation in result has been found to be 4.12 % for the defect width which was verified with image analysis methods using an optical microscope and contact measurement.
Keywords: condition monitoring, bearing vibration analysis, wavelet, entropy, dynamic model

Highlights
- *A new method for diagnosis of manufacturing faults of tapered roller bearings has been developed.*
- *The geometrical size of the fault has been calculated from the vibration signature.*
- *Nine different wavelets have been compared as regards to their efficiency for fault diagnosis on the basis of Energy-to-Shannon-Entropy ratio criteria to reveal the faults.*
- *A sensitive and accurate test rig has been developed with high-quality data acquisition system to obtain precise measurement data.*
- *Verification using an optical microscope and contact measurement showed a slight deviation from the measured values; the method could be applied in industrial applications.*

0 INTRODUCTION

Production of tapered roller bearings is a sophisticated process influenced by several factors, such as worn table traverse mechanisms, inappropriate technological parameters, incorrect grinding wheels, vibrations due to the spindle mechanism, or dirty coolant. Investigation of the effects of the different manufacturing faults to the vibration generated is still an important and demanding task.

Research on various bearing defects by vibration analysis mostly focus on operational defects caused by wear and cracks. Patel et al. [1] used envelope methods to reveal local faults on the races of deep groove ball bearings. Kalman and H filters were applied by Khanam et al. [2] to measure bearing faults, especially in noisy condition with low signal-to-noise ratios when it was difficult to identify the useful components of the vibration signal. Acoustic emission measurement is a powerful method to detect cracks inside the bearing material, which are the initial reasons of fatigue spallings. Al-Ghamd and Mba [3] applied this method combined with the traditional vibration analysis to determine the bearing outer race defect width directly from the raw signal. Elforjani and Mba [4] emphasized the effectiveness of acoustic emission methods in the case of slow-speed bearings. Sawalhi and Randall [5] execute their research to determine the fault size of the bearings from the vibration signal by analysing the entry and exit impulses.

Because of their flexibility and computational efficiency, wavelets are perfect tools for fault feature extraction, singularity detection for signals, denoising, and extraction of the weak signals from the vibration signals. These applications were presented by Peng and Chu [6]. Discrete wavelet transform with Daubechies-4 (db04) mother wavelets to analyse the combination of different faults on the races of ball bearings were used by Prabhakar et al. [7]. The

*Corr. Author's Address: University of Debrecen, Faculty of Engineering, 2-4 Ótemető, 4028 Debrecen, Hungary, deak.krisztian@eng.unideb.hu

combination of envelope spectrum and wavelet transform for the extraction of defect problems in bearings were used by Shi et al. [8].

Nikolaou and Antoniadis [9] applied complex shifted Morlet wavelets to analyse vibration signals generated by rolling element bearings.

Qiu et al. [10] successfully used a wavelet filter-based weak signature detection method and its application for diagnosis of rolling element bearings.

Junsheng et al. [11] pointed out the effectiveness of impulse response wavelet to the fault diagnosis of rolling element bearings.

Symlet wavelets were used efficiently in the study of Kumar and Singh [12]. In their study, tapered roller bearings were analysed to determine the fault size on the outer ring.

Symlet wavelet is an effective tool for noise reduction in ECG signals because it can filter out the useful components of the complex signal from the noisy background [13]. Symlet-5 wavelet represents the entry and impact events as the roller hits the defects during operation of the bearing. A detailed study was presented about the decomposition of the vibration signals using discrete wavelet transform with Symlet-5 by Kumar et al. [14].

Analytical Wavelet Transform-(AWT) based acoustic emission techniques for identifying the inner race of the radial ball bearing were applied by Kumar et al. [15].

Yan and Gao [16] revealed localized structural defects and conducted experiments in their studies using multi-scale enveloping spectrogram for the vibration analysis of bearings.

Patil et al. [17] developed an analytical model and simulation to predict the effect of a localized defect on the ball bearing vibrations by considering the contact between the ball and the races as non-linear springs.

Optimal wavelet filtering and sparse code shrinkage were presented by He et al. [18]. To extract the impulsive features buried in the vibration signal, a hybrid method which combines a Morlet wavelet filter and sparse code shrinkage (SCS) was proposed. First, the wavelet filter was optimized using differential evolution (DE) to eliminate the interferential vibrations and obtain the fault characteristic signal. Then, to further enhance the impulsive features and suppress residual noise, SCS, which was a soft-thresholding method based on maximum likelihood estimation (MLE), was applied to the filtered signal.

Simulations and signal processing techniques to track the spall size were used by Sawalhi and Randall [19].

Kumar and Singh [20] applied the discrete wavelet transform of the vibration signal to determine the outer race defect width measurement in tapered roller bearings, which was previously prepared using an electric discharging machine.

Khanam et al. [21] estimated the fault size in the outer race of ball bearings using the discrete wavelet transform of the vibration signal.

Tóth and Tóth [22] and [23] revealed artificial faults of the inner rings of deep groove bearings by wavelet analysis. A realistic signal model of ball bearings with inner race fault was created to design a new wavelet to reveal the defect more efficiently from the vibration signature.

Beyond vibration analysis, there are other diagnosis methods, e.g. oil analysis, which could enhance the efficiency of methods [24].

Zhuang Li et al. applied wavelet transform with an artificial neural network for the diagnosis of gearboxes [25].

Machine-learning methods for the optimization of parameters such as support vector machines were used by Mankovits et al. [26].

Khanam et al. [27] presented a theoretical model for the force function as a bearing rolling element hits a spall-like defect on the inner race. The vibratory response was simulated with a fourth-order Runge Kutta method and analysed in both time and frequency domain. It offers a platform for monitoring the size defect.

Borghesani et al. [28] applied cepstrum pre-whitening for diagnostics of rolling element bearings. Due to its moderate computational requirements, it was an appropriate tool for an automatic damage recognition algorithm. A comparison with the traditional pre-whitening techniques revealed that cepstrum pre-whitening was a more suitable and efficient tool for automatic fault detection.

Figlus and Stanczyk [29] presented a method of diagnosing damage to rolling bearings near toothed gears of processing lines. Vibration response was measured with a laser vibrometer. Discrete wavelet transform was successfully applied to detect damage.

Tabaszewski [30] researched the classification of defects of rolling bearings by k-NN classifier with regard to the proper selection of the observation place. Typical parameters, such as root mean square (r.m.s) and peak values of the vibration signal and the energy of acoustic emission pulses was found to be effective for revealing cracks in the outer rings.

Gligorijevic et al. [31] presented an automated technique for the early fault detection of rolling element bearings by dividing the signal to sub-

bands by means of wavelet decomposition. A two-dimensional feature space was used for fault detection of the bearing elements by quadratic classifiers with high accuracy.

Strączkiewicz et al. [32] applied supervised and unsupervised pattern recognition methods for damage classification and the clustering of rolling bearings. Clustering analysis was effective for determining the number of bearing state conditions.

Slavič et al. [33] used force measurement instead of the traditional acceleration measurement to identify bearing faults. The signal was processed using an envelope technique. The research showed that frequency domain analysis could successfully be applied to identify both amplitude and frequency of the force signal. The procedure was also applied to a high-series production line.

Abboud et al. [34] characterized bearing fault vibrations and explored angle/time cyclo-stationary properties. They experimentally validated their results on real vibration signals and the possible application for bearing fault detection.

Paya et al. [35] analysed drive lines with multiple faults that consist of an automotive gearbox, disc brake, and bearings. The paper presented an investigation to study both bearing and gear faults by wavelet transform then classified by multilayer back-propagation artificial neural networks to classify the faults into groups.

Antoni [36] applied a cyclic spectral tool for the incipient fault diagnosis of rolling element bearings. They demonstrated the optimality of cyclic coherence. It was proved that the diagnostic information is perfectly preserved in the cyclic frequency domain as a symptomatic pattern of spectral lines.

1 FEATURE EXTRACTION FROM THE VIBRATION SIGNAL

1.1 Optimal Wavelet Selection

The wavelet transform is continuous or discrete, and it is calculated by the convolution of the signal and a wavelet function. A wavelet function is a small oscillatory wave, which contains both the analysis and the window function. Continuous wavelet transform (CWT) generates the two-dimensional maps of coefficients that are called scalograms:

$$CWT_f(a,b)=\frac{1}{\sqrt{a}}\int_{-\infty}^{\infty} f(t)\cdot\psi^*\left(\frac{t-b}{a}\right)dt, \qquad (1)$$

where a is the scale parameter, b is the translation parameter, $f(t)$ is the signal in time domain, ψ is the 'mother' wavelet, and ψ^* is the complex conjugate of ψ [37].

The benefit of CWT is that by changing the scale parameter, the duration and bandwidth of wavelet are both changed, providing better time or frequency resolution, but its shape remains the same. The scale parameter can be continuous or dyadic. The CWT uses short windows at high frequencies and long windows at low frequencies.

The scalogram, defined as the squared magnitude of CWT, always has non-negative, real-valued time-frequency (scale) distribution. Its resolution in the time-frequency plane depends on the scale parameter.

$$SC\{f(a,b)\}=\left|CWT_f(a,b)\right|^2= \\ =\left|\int_{-\infty}^{\infty} f(t)\cdot\frac{1}{\sqrt{a}}\psi^*\left(\frac{t-b}{a}\right)dt\right|^2. \qquad (2)$$

Consider the family of functions obtained by shifting and scaling a "mother wavelet" ψ;

$$\psi_{a,b}=\frac{1}{|a|}\psi^*\left(\frac{t-b}{a}\right), \qquad (3)$$

where $a,b\in\mathbb{R}$ ($a\neq 0$), and the normalization ensures that $||\psi_{a,b}(t)||=||\psi(t)||$. The wavelet should satisfy the admissibility condition:

$$c_\psi=\int_{-\infty}^{\infty}\frac{|\Psi(w)|^2}{|w|}dw<\infty, \qquad (4)$$

where Ψ is the Fourier transform of ψ, w is the frequency. In practice, Ψ will always have sufficient decay so that the admissibility condition reduces to the requirement that $\Psi(0)=0$ (from discrete Fourier transform):

$$\int_{-\infty}^{\infty}\psi(t)\,dt=\Psi(0)=0. \qquad (5)$$

Because the Fourier transform is zero at the origin and the spectrum decays at high frequencies, the wavelet has bandpass behaviour. The wavelet should be normalized so that it has unit energy:

$$\left\|\psi(t)\right\|^2=\int_{-\infty}^{\infty}\left|\psi(t)\right|^2dt=\frac{1}{2\pi}\int_{-\infty}^{\infty}\left|\psi(w)\right|^2dw=1. \qquad (6)$$

As a result, $||\psi_{a,b}(t)||^2=||\psi(t)||^2=1$ the continuous wavelet transform of a function $f\in L^2(\mathbb{R})$ is defined as:

$$CWT_f(a,b)=\int_{-\infty}^{\infty}\psi_{a,b}(t)\cdot f(t)\,dt. \qquad (7)$$

Discrete wavelet transform (DWT) applies filter banks for the analysis and synthesis of a signal. Filter banks contain wavelet filters and extract the frequency content of the signal in the pre-determined subbands. The discrete wavelet transform is derived from the discretization of continuous wavelet transform by adopting the dyadic scale and translation to reduce the computational time and can be expressed by the following equation [24]:

$$DWT_s(j,k) = \frac{1}{\sqrt{2^j}} \int_{-\infty}^{\infty} s(t) \cdot \psi^* \left(\frac{t - 2^j k}{2^j} \right) dt, \quad (8)$$

where j and k are integers, 2^j and $2^j k$ represent the scale and translation parameter respectively. The original signal $s(t)$ passes through a set of low pass and high pass filters emerging as low frequency (approximations, a_i) and high frequency (details, d_i) signals at each decomposition level i. They are usually finite impulse response filters whose impulse response (or response to any finite length input) is of finite duration, because it settles to zero in finite time. Therefore, the original signal $s(t)$ can be written as:

$$s(t) = a_n + \sum_{i=1}^{n} d_i. \quad (9)$$

The wavelet function ψ and scaling function φ can be defined as follows:

$$\psi_{j,k}[t] = 2^{\frac{j}{2}} \sum_k d_{j,k} \psi[2^j t - k], \quad (10)$$

$$\phi_{j,k}[t] = 2^{\frac{j}{2}} \sum_k c_{j,k} \phi[2^j t - k], \quad (11)$$

where $d_{j,k}$ and $c_{j,k}$ are the wavelet and scaling coefficients at scale j [38].

Assuming the signal $X[t]=(v_0, ..., v_{N-1})$, the sampling number is $N=2^j$, where j is an integer. For $X_j[t]$ at scale j decomposed to the scale $j-1$ of DWT model can be defined as [39]:

$$DWT(X_j[t]) = \\ = 2^{\frac{j-1}{2}} \cdot \left(\sum_{k=0} cA_{j-1,k} \phi[2^{j-1} t - k] + \sum_{k=0} cD_{j-1,k} \psi[2^{j-1} t - k] \right), \\ 0 \le k \le \frac{N}{2^j} - 1, \quad (12)$$

where

$$cA_{j-1,k} = \sum_{h=0}^{\frac{N}{2^j}-1} c_{j,h} v_{j,h+2n}, \quad cD_{j-1,k} = \sum_{h=0}^{\frac{N}{2^j}-1} d_{j,h} v_{j,h+2n},$$

$$d_h = (-1)^h c_{2p-1-h}, \quad p = N / 2^j.$$

The frequency band of each wavelet level is defined by Parameswariah and Cox [40]:

$$f = 2^j \cdot F_s / N, \quad (13)$$

and the maximum frequency is:

$$f_{\max} = F_s / 2, \quad (14)$$

where f is the higher frequency limit of the frequency band represented by the level j, F_s is the sampling frequency and N is the number of data points in the input signal.

1.2 Maximum Energy to Shannon Entropy Ratio Criteria

Fault detection procedures based on time-frequency methods usually rely on the visual observation of contour plots. It is also known that if the wavelet matches well with the shape of the signal at a specific scale and location, a large transform value is obtained. However, a low transform value is obtained if the signal and wavelet do not correlate well. To avoid defects of visual observation, a more precise way of determining the best-suited wavelet is presented here.

The combination of the energy and Shannon entropy content of the wavelet coefficients of the signal, denoted by the Energy-to-Shannon-Entropy ratio is an appropriate indicator to choose the best wavelet for diagnosis, and it can be calculated in the following form [41] and [42]:

$$\xi(n) = E(n) / S_{entropy}(n). \quad (15)$$

The energy content of signal wavelet coefficients is given by:

$$E(n) = \sum_{i=1}^{m} \left| C_{n,i} \right|^2, \quad (16)$$

where m is the number of wavelet coefficients, $C_{n,i}$ is the i^{th} wavelet coefficient of n^{th} scale.

The entropy of signal wavelet coefficients is given by:

$$S(n) = -\sum_{i=1}^{m} p_i \log_2 p_i, \quad (17)$$

where $(p_1, ..., p_n)$ is the energy probability distribution of the wavelet coefficients, defined as:

$$p_i = \left| C_{n,i} \right|^2 / E(n). \quad (18)$$

1.3 Fault Size Estimation

When there is a defect in the rolling element bearing, the rolling element hits the raceway, and a transient impulse is produced. Because the impulse with short time duration is a transient excitation, the response of

the bearing system's natural frequency would arise. Modelling the bearing vibration system as an under-damped second order mass-spring-damper dynamic mechanical system, its unit-impulse response function can be described as follows:

$$h(t) = \frac{1}{m\omega_d} e^{-(\xi/\sqrt{(1-\xi^2)\omega_d t})} \sin(\omega_d t), \quad (19)$$

where m is the mass of the bearing vibration system, ξ is the damping ratio of the mechanical system and ω_d is the damped natural frequency of the bearing structure **[43]**.

To determine the defect size, multiresolution analysis (MRA) is applied by filter banks, which is a design method of most of the practically relevant discrete wavelet transforms.

Usually, two or three harmonics of the characteristic defect frequency are necessary for bearing fault diagnosis. In order to diagnose the modulation effects, the width of each band (F_j) should be three times greater than the bearing pass frequency of the inner race, and it can be calculated by **[44]**:

$$F_j \approx F_s / 2^{j+1}. \quad (20)$$

This implies that the final level J_f should satisfy:

$$J_f \leq \log_2 \frac{F_S}{3rF_R} - 1, \quad (21)$$

where F_R is the frequency of the shaft, here is 30 Hz and F_S is the sampling rate that is now 25.6 kHz. Practically, J_f=3 and J_f=4 values are found to be large enough for bearing vibration diagnosis **[44]**.

In our investigation, the value of J_f=3 is proposed. In the case of No. 30205, the tapered roller bearing in the experiment BPFO is 206.18 Hz. Down to 3rd level, where the transient impulse is analysed for defect width measurement, wavelet band is 1.25 kHz, which is more than 3 times greater than BPFO. However, decomposition is down to the 4th level because of deeper resolution.

The defect size on the outer race of the bearing can be estimated from the knowledge of the duration between the entry and exit events extracted from the signal after decomposition for the wavelet. The duration of the signal is estimated by wavelet decomposition using the fundamental train frequency (FTF) and average outer race inner diameter of the bearing (D_{OI}). The outer race defect width D_{OD} is **[12]**:

$$L_{OD} = \pi \cdot \Delta t \cdot D_{OI} \cdot FTF. \quad (22)$$

This method is very useful because the defect width of the bearing can be determined only from the vibration signature. Bearing defects generate transient impulses in the vibration signal when the rollers pass through the defects. The fault frequencies can be calculated by numerically: bearing pass frequency of outer race (BPFO), bearing pass frequency of inner race (BPFI), fundamental train frequency (FTF), ball spin frequency (BSF). FTF can be calculated using the Eq. 22. **[5]** and **[7]**:

$$FTF = \frac{f_r}{2}\left(1 - \frac{d}{D}\cos\Phi\right), \quad (23)$$

where f_r is the rotational frequency of the shaft, Φ is the contact angle, d is the inner ring diameter, D is the outer ring diameter. Practically, skipping phenomena could change this theoretical value.

Analysis of the de-stressing and re-stressing points of the entry and exit events from the manufacturing defect is necessary for the fault size estimation. The peaks in signal with negative and positive sign describe the position of the ball in the defect.

2 EXPERIMENTAL SETUP

In this study, an experimental test rig (Figs. 1 and 2.) has been constructed to measure the vibration signatures of the tapered roller bearings properly.

The shaft in the test rig is supported by two tapered roller bearings. The one under investigation is No. 30205. Four tapered roller bearings with different manufacturing defect widths on the outer race (OR1-4) were investigated in our experiments (Table 1). The defect on the outer race is a line (rectangular) shape-grinding defect (Fig. 3). The shaft is driven by an alternating current motor of 0.75 kW (made by Cemer), the frequency of 50 Hz, and the nominal speed of 2770 rpm, which is reduced to 1800 rpm with a variable speed drive device. A rubber V-belt between the electric engine and the shaft provides smooth running and low vibration which aid in accurate and precise measurements. Rubber bumpers are installed to reduce vibration of the electric motor to the bearing housing to minimize harmful vibrations. The arrangement provides the option of different speeds controlled by a Schneider ATV32HU22M2 variable speed drive device. In the experiment, the speed of the shaft is measured using an optical tachometer with digital display to check the speed fluctuations. Additionally, the test rig can also be used for acoustic measurements because an anechoic chamber is installed around the test bearing house with appropriate features to suppress outside noises

and reduce echo time. Test bearing is spanned by a screw mechanism to supply the sufficient axial force to the measurements. Constant spanning force during the measurements is measured by strain gauges in a Wheatstone-bride mode on the basis of the difference in voltage measurement.

NI 9234 dynamic signal acquisition is used in the experiments with 4 channels to vibration measurements from integrated electronic piezoelectric (IEPE) and non-IEPE sensors. The NI 9234 delivers 102 dB of dynamic range. Input channels simultaneously digitize signals at rates up to 51.2 kHz per channel with built-in anti-aliasing filters [45]. A PCB IMI 603C01 vibration transducer is used, which is an industrial type platinum stock piezoelectric sensor with low noise levels, the sensitivity of 100 mV/g and frequency range of 0.27 kHz to 10 kHz with a top exit 2-pin connector [46]. The accelerometer is placed on the previously ground surface of the top of the bearing house with a screw mechanism perpendicular to the axis of the rotation of the shaft. A 32-bit AMD Athlon II X2 M300 2.0 GHz processor is used for data processing which is carried out in Matlab and Labview environments. For visual validation of the defect sizes on the bearing rings Garant MM1-200 video microscope is applied, which is an incremental measuring system, with a built-in image processing with a 1.3-megapixel colour camera. Furthermore, Mahr MMQ 200 with precision roundness measuring axis, motorized vertical and horizontal measuring axis is used for roundness deviation measurement to determine both width and depth of the grinding marks.

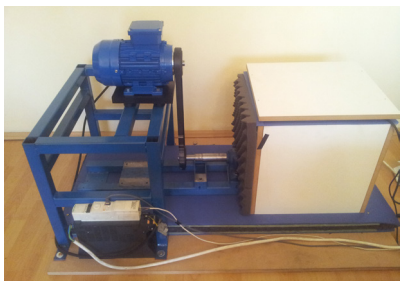

Fig. 1. *Test rig for tapered roller bearing measurement*

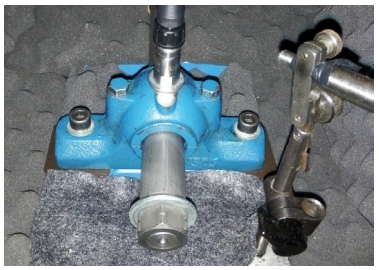

Fig. 2. *Test rig for tapered roller acoustic chamber*

Table 1. Geometrical parameters of grinding defects of outer rings (OR)

Type	Width [mm]	Depth [μm]
OR1 defect	0.6311	6.5
OR2 defect	1.2492	33.6
OR3 defect	1.4751	42.3
OR4 defect	1.6236	51.4

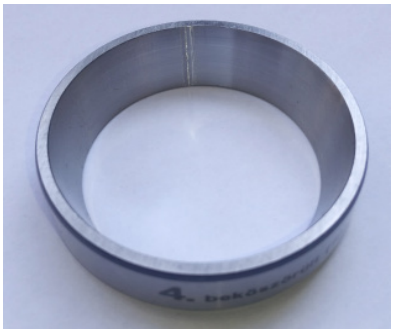

Fig. 3. *Outer ring of the tapered roller bearing with grinding defect of 1.6236 mm*

3 RESULT AND DISCUSSION

3.1 Optimal Wavelet Selection

A total of nine different wavelets is considered for the present study. An appropriate base wavelet should extract the maximum amount of energy, and minimize the Shannon entropy of the corresponding wavelet coefficients. Calculated values of the energy to Shannon entropy ratios are in Tables 2 to 4.

E/S values are calculated from the vibration signal at the wavelet centre frequency (F_c) of 2.09 kHz (Table 2).

Table 2. *Calculated values of energy to Shannon entropy ratios of wavelet functions, Fc = 2.09 kHz*

E/S	OR1	OR2	OR3	OR4	Mean
Sym2	59.96	80.20	100.87	109.16	87.55
Sym5	65.58	95.37	117.07	119.92	99.48
Sym8	82.81	113.77	120.16	118.48	108.81
db02	60.91	81.09	101.12	113.46	89.14
db06	71.74	89.02	120.42	117.40	99.65
db10	77.76	104.69	120.34	120.45	105.81
db14	85.02	120.03	121.37	123.78	112.55
Meyer	92.31	160.31	126.20	105.70	121.13
Morlet	113.15	194.15	142.18	138.14	146.90

After calculating the mean values of E/S ratio values are presented in Table 2. It is observed that Morlet wavelet gives the highest value that indicates

to be the most efficient wavelet for both fault detection and fault size estimation.

3.2 Fault Size Estimation

Bearing defects generate transient impulses in the vibration signal when the rollers pass through the defects.

For fault size estimation, fault frequencies are calculated which are $BPFO = 206.18$ Hz, $BPFI = 287.15$ Hz, $FTF = 12.88$ Hz, $BSF = 89.96$ Hz in this experiment at 1800 rpm.

$$L_{OD} = \pi \cdot \Delta t \cdot D_{OI} \cdot FTF = 1713.74 \cdot \Delta t. \quad (24)$$

With Eq. (24), the width of the defect can be calculated, where D_{OI} is the outer ring diameter on the raceways; Δt is the time duration between the contact points of the bearing elements. In the raw signal, entry and exit points of the groove are not identifiable because the signal at these points is weak, but wavelet decomposition makes it possible to analyse the entry and exit events. The best wavelet previously chosen by the Shannon entropy criteria gives the best method to determine the fault size from the vibration signature because it presents the best correlation with the transient impulse.

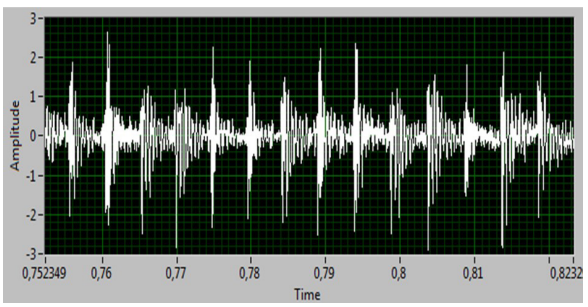

Fig. 4. *Typical raw time domain signal of bearing with 0.6311 mm of ground fault width on the outer race*

Fig. 4 presents the spectra of outer race defect of 0.6311 mm. The highest periodic transient impulse related energy content of the burst occurs at 2.09 kHz that causes a 5 ms rate of periodicity which is equal to 206.18 Hz *BPFO* frequency (Fig. 5). The spectrum was measured in all outer rings with different fault sizes, and they showed a similar manner around the peak of 2.09 kHz.

Multiresolution analysis (MRA) is made down to the 4th level to obtain precise frequency analysis. Fig. 6 presents the wavelet decomposition tree down to the 4th level. Higher decomposition is not necessary because it might not reveal any further information of the signal. Regarding the *BPFO* frequency, analysis was made at 3rd detail level (cD_3) from 1.25 kHz to 2.5 kHz.

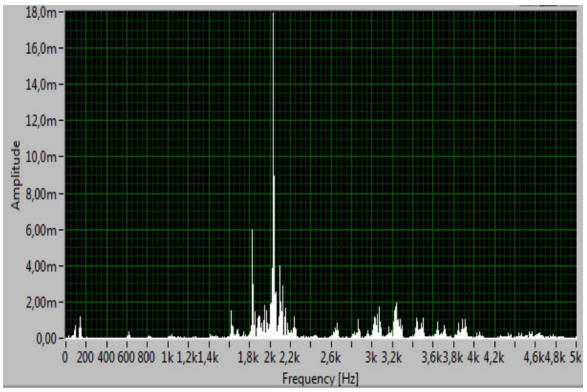

Fig. 5. *Frequency domain spectrum of bearing with 0.6311 mm of ground fault width on the outer race, transient frequency of 2.09 kHz*

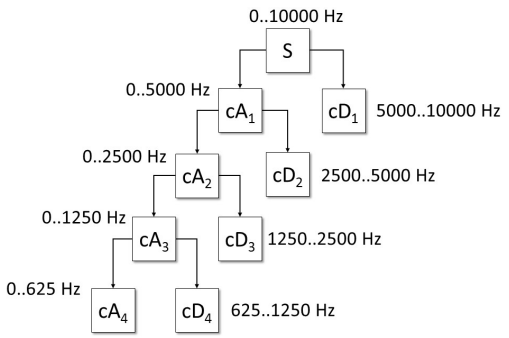

Fig. 6. *Wavelet decomposition graph of the original vibration signal by MRA with frequency ranges*

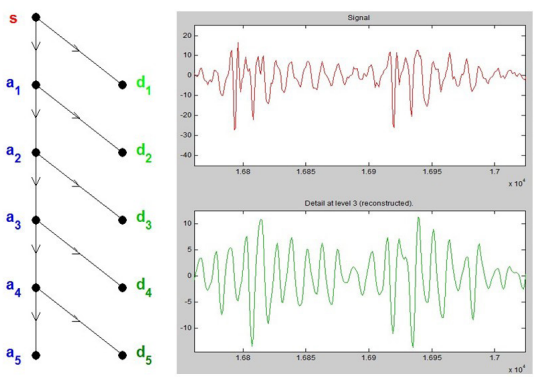

Fig. 7. *Tree decomposition graph of the original vibration signal of 0.6311 mm fault width down to 4th level*

Fig. 7 shows the decomposition graph of the original vibration signal of 0.6311 mm fault width down to 4th level. A is the entry point of the roller into the outer race defect, B is the maximum de-stressing, C is the exit point of the roller from the defect. In

the experiment, 20 impulses were measured and the average time values of the entry, de-stressing and exit point of all four outer rings were determined for precise calculation, which yielded 240 time data points.

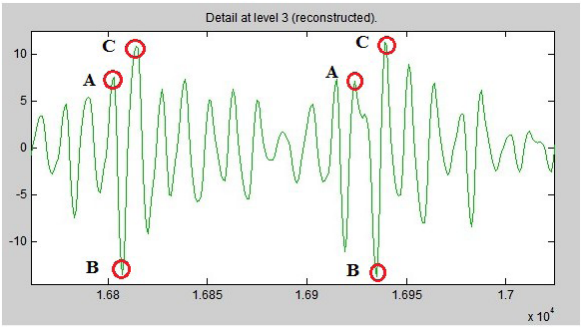

Fig. 8. *Detail graph of the MRA of the original vibration signal of 0.6311 mm fault width at detail 3rd level with two transient impulses, entry point (A), de-stressing point (B) and exit point (C) are highlighted in red*

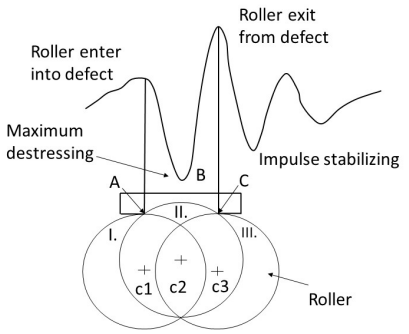

Fig. 9. *Analysis of the transient impulse presenting the entry and exit points of the roller into the grinding defects on the outer ring*

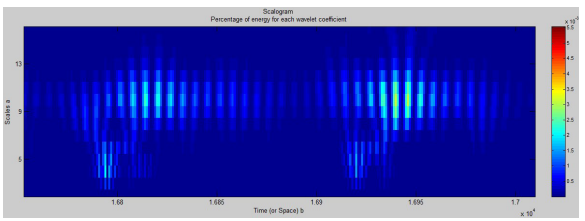

Fig. 10. *Scalogram of the Morlet wavelet of the outer ring with 0.6311 mm fault width*

Figs. 8 to 10 show the analysis of the entry point, the exit point and the de-stressing point of the roller for the purpose of fault size calculation. At point A, the roller strikes the groove base with a high impact which results in re-stressing and high impulse in the signal. After this event, the roller remains in contact with the groove base for some time and during this period impulses due to the rough surface of the groove are observed.

When the roller comes in contact with point B, it again generates high amplitude in the signal, and beyond this (i.e. after B) progressive decreases in the amplitude of the signal are observed due to elastic damping of bearing element. The roller may spin or slide during the operation of the bearing. Change in signal takes place when it slides. Furthermore, varying clearance between cage and roller changes the signal when the roller enters and exits the groove defect.

There is variation in data points for each roller crossing over the defect. Average data points for 16 successive bursts are calculated for estimating the time taken by roller to pass over the groove defect. The average of data points so calculated is converted into the time duration to cross over from A to B, considering the sampling frequency. Further using Eq. (24), the defect width was calculated in the case of all outer rings. A scalogram was applied in addition to the multiresolution analysis as was presented in Fig. 10.

4 VERIFICATION OF THE MEASUREMENT BY IMAGE PROCESSING

To verify the precision of the previous measurements, image processing is applied to reveal the exact geometrical size of the ground defect on the outer race. A Garant MM1-200 video microscope is used to analyse and measure the grinding marks on the rings and Mahr MMQ 200 contact equipment is applied for roundness deviation measurement of the outer rings to determine the depth of the grinding marks on the rings as Figs. 11 to 16 present.

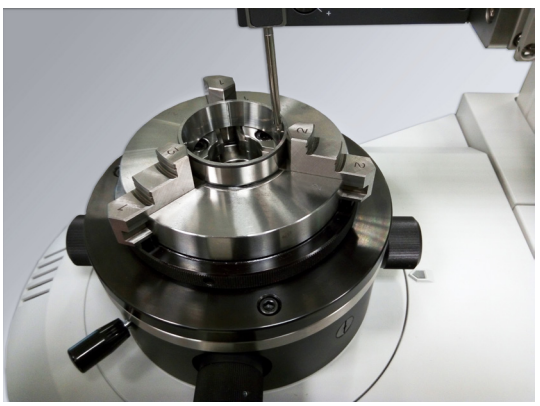

Fig. 11. *Contact measurement of the outer race defect geometrical size with Mahr MMQ 200 equipment*

To find the edges of the grinding marks on the outer race made by the Garant MM1-200 video microscope, Prewitt and Sobel edge detection algorithms are used as image processing technique. In

our investigations, the Prewitt algorithm is found to be more efficient.

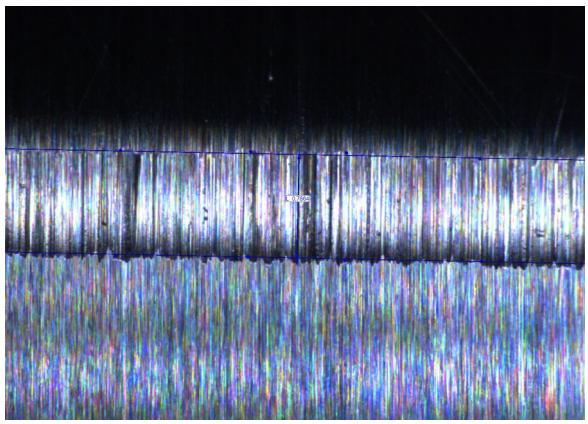

Fig. 12. *Image of the optical measurement of the outer race defect width with Garant MM1-200 video microscope*

The maximum difference in result has been obtained to be 4.12 % for a defect width of 0.6311 mm by db02 wavelet. The width calculation and the deviation from the visually measured data using the worst wavelet for fault detection (db02), the traditionally widely used Symlet-5, and the best Morlet wavelet are found in Tables 3 to 5. The Morlet wavelet provides the most accurate width measurement from the vibration signal.

Table 3. *Deviation values of geometrical width of the fault from the vibration signal and optically measured values with db02 wavelet*

	OR1 defect	OR2 defect	OR3 defect	OR4 defect
Calculated defects width [mm]	0.657	1.521	1.277	1.653
Optically measured defect width [mm]	0.6311	1.4751	1.2492	1.6236
Deviation between calculated and measured data [%]	4.12	3.11	2.24	1.78
Mean deviation [%]	2.81			

Table 4. *Deviation values of geometrical width of the fault from the vibration signal and optically measured values with Symlet-5 wavelet*

	OR1 defect	OR2 defect	OR3 defect	OR4 defect
Calculated defects width [mm]	0.646	1.4481	1.269	1.639
Optically measured defect width [mm]	0.6311	1.4751	1.2492	1.6236
Deviation between calculated and measured data [%]	2.41	1.83	1.56	0.92
Mean deviation [%]	1.68			

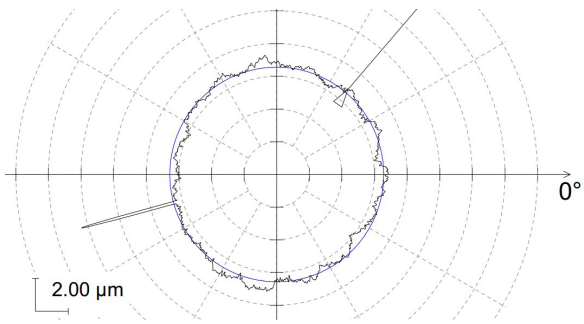

Fig. 13. *Result of the roundness measurement of the outer race defect with Mahr MMQ 200 equipment, OR1 defect*

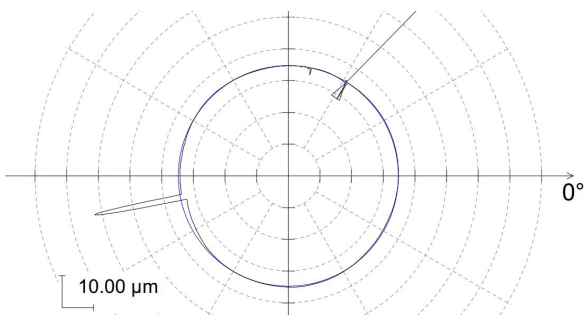

Fig. 14. *Result of the roundness measurement of the outer race defect with Mahr MMQ 200 equipment, OR2 defect*

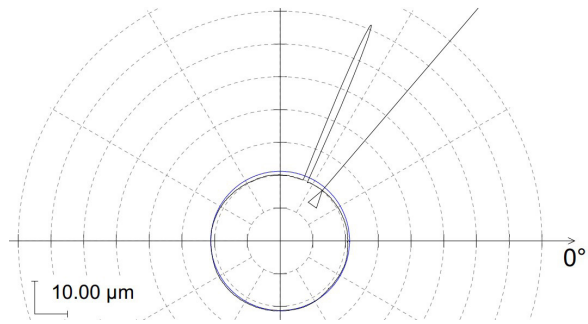

Fig. 15. *Result of the roundness measurement of the outer race defect with Mahr MMQ 200 equipment, OR3 defect*

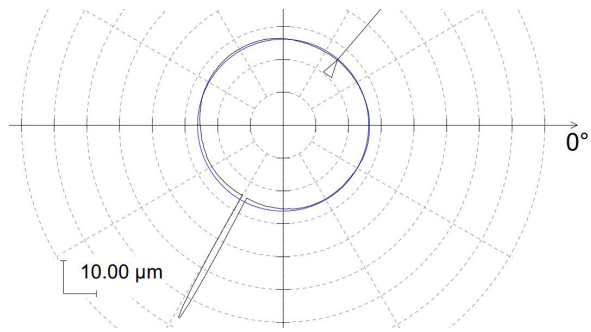

Fig. 16. *Result of the roundness measurement of the outer race defect with Mahr MMQ 200 equipment, OR4 defect*

Table 5. *Deviation values of geometrical width of the fault from the vibration signal and optically measured values with Morlet wavelet*

	OR1 defect	OR2 defect	OR3 defect	OR4 defect
Calculated defects width [mm]	0.644	1.502	1.266	1.637
Optically measured defect width [mm]	0.6311	1.4751	1.2492	1.6236
Deviation between calculated and measured data [%]	2.06	1.69	1.38	0.84
Mean deviation [%]	1.49			

5 CONCLUSIONS

A technique based on wavelet transform using nine different real-valued wavelets has been proposed for measuring the outer race manufacturing defect widths of tapered roller bearings.

Wavelet coefficients were determined at constant scale value of the scalograms of four outer rings with grinding manufacturing defects. Then, wavelet coefficients at the highest local maxima of the scalograms were calculated. Moreover, Butterworth filter was applied near the fault generated transient impulse with the frequency of 2.09 kHz to suppress noise related frequency components and enhance the useful information from the vibration signature. Nine real-valued wavelets were analysed, and it was determined that Morlet wavelet was the best for the manufacturing fault detection in all cases on the basis of the Shannon Entropy Criteria. Furthermore, the width measurement of the outer ring grinding fault was executed with all nine wavelets. The best wavelet previously chosen by Shannon Entropy Criteria creates the opportunity to determine the manufacturing defect width in the most accurate way because it presents the best correlation with the transients. The proposed technique has been successfully implemented for measuring defect width over a range of 0.6311 mm to 1.6236 mm. The defect width has also been verified by an optical microscope and contact roundness measurement device using image processing techniques. The maximum deviation of the two values of defect width obtained using the aforementioned two different visual measurement validation approaches is 4.12 % for a defect width of 0.6311 mm.

6 REFERENCES

[1] Patel, V.N., Tandon, N., Pandey, R.K. (2012). Defect detection in deep groove ball bearing in the presence of external vibration using envelope analysis and Duffing oscillator. *Measurement*, vol. 45, no. 5, p. 960-970, **DOI:10.1016/j.measurement.2012.01.047**.

[2] Khanam, S., Tandon, N., Dutt, J.K. (2012). Fault identification of rolling element bearings from vibration signals: An application of Kalman and H∞ filters. *10th International Conference on Vibrations in Rotating Machinery*, p. 703-713, **DOI:10.1533/9780857094537.11.703**.

[3] Al-Ghamd, A.M., Mba, D. (2006). A comparative experimental study on the use of acoustic emission and vibration analysis for bearing defect identification and estimation of defect size. *Mechanical Systems and Signal Processing*, vol. 20, no. 7, p. 1537-1571, **DOI:10.1016/j.ymssp.2004.10.013**.

[4] Elforjani, M., Mba, D. (2010). Accelerated natural fault diagnosis in slow speed bearings with acoustic emission. *Engineering Fracture Mechanics*, vol. 77, no. 1, p. 112-127, **DOI:10.1016/j.engfracmech.2009.09.016**.

[5] Sawalhi, N., Randall, R.B. (2011). Vibration response of spalled rolling element bearings: Observations, simulations and signal processing techniques to track the spall size. *Mechanical Systems and Signal Processing*, vol. 25, no. 3, p. 846-870, **DOI:10.1016/j.ymssp.2010.09.009**.

[6] Peng, Z.K., Chu, F.L. (2004). Application of the wavelet transform in machine condition monitoring and fault diagnostics. *Mechanical Systems and Signal Processing*, vol. 18, no. 2, p. 199-221, **DOI:10.1016/S0888-3270(03)00075-X**.

[7] Prabhakar, S., Mohanty, A.R., Sekhar, A.S. (2002). Application of discrete wavelet transform for detection of ball bearing race faults. *Tribology International*, vol. 35, no. 12, p. 793-800, **DOI:10.1016/S0301-679X(02)00063-4**.

[8] Shi, D.F., Wang, W.J., Qu, L.S. (2004). Defect detection for bearings using envelope spectra of wavelet transform. *ASME Journal of Vibration and Acoustics*, vol. 126, no. 4, p. 567-357, **DOI:10.1115/1.1804995**.

[9] Nikolaou, N.G., Antoniadis, I.A. (2002). Demodulation of vibration signals generated by defects in rolling element bearings using complex shifted morlet wavelets. *Mechanical Systems and Signal Processing*, vol. 16, no. 4, p. 677-694, **DOI:10.1006/mssp.2001.1459**.

[10] Qiu, H., Lee, J., Lin, J., Yu, G. (2006). Wavelet filter-based weak signature detection method and its application on rolling element bearing prognostics. *Journal of Sound and Vibration*, vol. 289, no. 4-5, p. 1066-1090, **DOI:10.1016/j.jsv.2005.03.007**.

[11] Junsheng, C., Dejie, Y., Yu, Y. (2007). Application of an impulse response wavelet to fault diagnosis of rolling bearings. *Mechanical Systems and Signal Processing*, vol. 21, no. 2, p. 920-929, **DOI:10.1016/j.ymssp.2005.09.014**.

[12] Kumar, R., Singh, M. (2013). Outer race defect width measurement in tapered roller bearing using discrete wavelet transform of vibration signal. *Measurement*, vol. 46, no. 1, p. 537-545, **DOI:10.1016/j.measurement.2012.08.012**.

[13] Awal, M. A., Mostafa, S. S., Ahmad, M. (2012). Quality assessement of ECG signal using symlet wavelet transform. *Proceedings of International Conference on Advances in Electrical Engineering*, p. 129-134.

[14] Chavan, M. S., Mastorakis, N., Chavan, M. N., Gaikwad, M. S. (2012). Implementation of SYMLET Wavelets to Removal of Gaussian Additive Noise from Speech Signal.

Recent Researches in Communications, Automation, Signal Processing, Nanotechnology, Astronomy and Nuclear Physics, p. 37-41.

[15] Kumar, R., Jena, D.P., Bains, M. (2010). Identification of inner race defect in radial ball bearing using acoustic emission and wavelet analysis. *Proceedings of ISMA 2010 including USD 2010 Leuven*, p. 2883–2891.

[16] Yan, R., Gao, R.X. (2009). Multi-scale enveloping spectrogram for vibration analysis in bearing defect diagnosis. *Tribology International*, vol. 42, no. 2, p. 293-302, **DOI:10.1016/j.triboint.2008.06.013**.

[17] Patil, M.S., Mathew, J., Rajendrakumar, P.K., Desai, S. (2010). A theoretical model to predict the effect of localized defect on vibrations associated with ball bearing. *International Journal of Mechanical Sciences*, vol. 52, no. 9, p. 1193-1201, **DOI:10.1016/j.ijmecsci.2010.05.005**.

[18] He, W., Jiang, Z., Feng, K. (2009). Bearing fault detection based on optimal wavelet filter and sparse code shrinkage. Measurement, vol. 42, no. 7, p. 1092-1102, **DOI:10.1016/j.measurement.2009.04.001**.

[19] Sawalhi, N., Randall, R.B. (2011). Vibration response of spalled rolling element bearings: observations, simulations and signal processing techniques to track the spall size. *Mechanical Systems and Signal Processing*, vol. 25, no. 3, p. 846-870, **DOI:10.1016/j.ymssp.2010.09.009**.

[20] Kumar, R., Singh, M. (2013). Outer race defect width measurement in tapered roller bearing using discrete wavelet transform of vibration signal. *Measurement*, vol. 46, no. 1, p. 537-545, **DOI:10.1016/j.measurement.2012.08.012**.

[21] Khanam, S., Tandon, N., Dutt, J.K. (2014). Fault size estimation in the outer race of ball bearing using discrete wavelet transform of the vibration signal. *Procedia Technology, 2nd International Conference on Innovations in Automation and Mechatronics Engineering*, vol. 14, p. 12-19, **DOI:10.1016/j.protcy.2014.08.003**.

[22] Tóth, L., Tóth, T. (2013). Construction of a realistic signal model of transients for a ball bearing with inner race fault. *Acta Polytechnica Hungarica*, vol. 10, no. 1, p. 63-80.

[23] Tóth, L., Tóth T. (2013). On finding wavelet basis for bearing fault detection. *Acta Polytechnica Hungarica*, vol. 10, no. 3, p. 17-35.

[24] Salguerio, J., Persin, G., Vizintin, J., Ivanovic, M., Dolenc, B. (2013). On-line oil monitoring and diagnosis. *Strojniški vestnik - Journal of Mechanical Engineering*, vol. 59, no. 10, p. 604-612, **DOI:10.5545/sv-jme.2013.973**.

[25] Li, Z., Ma, Z., Liu, Y., Teng, W., Jiang, R. (2015). Crack fault detection for a gearbox using discrete wavelet transform and an addaptive resonance theory neural network. *Strojniški vestnik - Journal of Mechanical Engineering*, vol. 61, no. 1, p. 63-73, **DOI:10.5545/sv-jme.2014.1769**.

[26] Mankovits, T., Szabó, T., Kocsis, I., Páczelt, I. (2014). Optimization of the Shape of Axi-Symmetric Rubber Bumpers. *Strojniški vestnik - Journal of Mechanical Engineering*, vol. 60, no. 1, p. 61-71, **DOI:10.5545/sv-jme.2013.1315**.

[27] Khanam, S., Tandon, N., Dutt, J.K. (2016). Multi-event excitation force model for inner race defect in a rolling element bearing. *Journal of Tribology*, vol. 138, no. 1, art. No. 011106, **DOI:10.1115/1.4031394**.

[28] Borghesani, P., Pennacchi, P., Randall, R.B., Sawalhi, N., Ricci, R. (2013). Application of cepstrum pre-whitening for the diagnosis of bearing faults under variable speed conditions. *Mechanical Systems and Signal Processing*, vol. 36, no. 2, p. 370-384, **DOI:10.1016/j.ymssp.2012.11.001**.

[29] Figlus, T., Stanczyk, M. (2016). A method for detecting damage to rolling bearings in toothed gears of processing lines. *Metalurgija*, vol. 55 no. 1, p. 75-78.

[30] Tabaszewski, M. (2014). Optimization of a nearest neighbors classifier for diagnosis of condition of rolling bearings. *Diagnostyka*, vol. 15, no. 1, p. 37-42.

[31] Gligorijevic, J., Gajic, D., Brkovic, A., Savic-Gajic, I., Georgieva, O., Di Gennaro, S. (2016). Online condition monitoring of bearings to support total productive maintenance in the packaging materials industry. *Sensors*, vol. 16 no. 3, p. 316, **DOI:10.3390/s16030316**.

[32] Strączkiewicz, M., Czop, P., Barszcz, T. (2016). Supervised and unsupervised learning process in damage classification of rolling element bearings. *Diagnostyka*, vol. 17, no. 2, p. 71-80.

[33] Slavič, J., Brković, A., Boltežar, M. (2011). Typical bearing-fault rating using force measurements: application to real data. *Journal of Vibration and Control*, vol. 17, no 14, p. 2164-2174, **DOI:10.1177/1077546311399949**.

[34] Abboud, D., Antoni, J., Eltabach, M., Sieg-Zieba, S. (2015). Angle\time cyclostationarity for the analysis of rolling element bearing vibrations. *Measurement*, vol. 75, p. 29-39, **DOI:10.1016/j.measurement.2015.07.017**.

[35] Paya, B.A., Esat, I.I., Badi, M.N.M. (1997). Artificial neural network based fault diagnostics of rotating machinery using wavelet transforms as a preprocessor. *Mechanical Systems and Signal Processing*, vol. 11, no. 5, p. 751-765, **DOI:10.1006/mssp.1997.0090**.

[36] Antoni, J. (2007). Cyclic spectral analysis of rolling-element bearing signals: Facts and fictions. *Journal of Sound and Vibration*, vol. 304, no. 3-5, p. 497-529, **DOI:10.1016/j.jsv.2007.02.029**.

[37] Misiti, M., Misiti, Y., Oppenheim, G., Poggi, J.-M. (eds.) (2007). Wavelets and their Applications. ISTE, London, **DOI:10.1002/9780470612491**.

[38] Wu, J.D., Liu, C.H. (2008). Investigation of engine fault diagnosis using discrete wavelet transform and neural network. *Expert Systems with Applications*, vol. 35, no. 3, p. 1200-1213, **DOI:10.1016/j.eswa.2007.08.021**.

[39] Teng, W., Wang, F., Zhang, K., Liu, Y., Ding, X. (2014). Pitting fault detection of a wind turbine gearbox using empirical mode decomposition. *Strojniški vestnik - Journal of Mechanical Engineering*, vol. 60, no. 1, p. 12-20, **DOI:10.5545/sv-jme.2013.1295**.

[40] Parameswariah, C., Cox, M. (2002). Frequency characteristics of wavelets. *IEEE Transactions on Power Delivery*, vol. 17, no. 3, p. 800-804, **DOI:10.1109/TPWRD.2002.1022806**.

[41] Kankar, P.K., Sharma, S.C., Harsha, S.P. (2011). Fault diagnosis of ball bearings using continuous wavelet transform. *Applied Soft Computing*, vol. 11, no. 2, p. 2300-2312, **DOI:10.1016/j.asoc.2010.08.011**.

[42] Kankar, P.K., Sharma, S.C., Harsha, S.P. (2013). Fault diagnosis of rolling element bearing using cyclic autocorrelation and

wavelet transform. *Neurocomputing*, vol. 110, p. 9-17, **DOI:10.1016/j.neucom.2012.11.012**.

[43] Feng, K., Jiang, Z., He, W., Qin, Q. (2011). Rolling element bearing fault detection based on optimal antisymmetric real Laplace wavelet. *Measurement*, vol. 44, no. 9, p. 1582-1591, **DOI:10.1016/j.measurement.2011.06.011**.

[44] Nikolaou, N.G., Antoniadis, I.A. (2002). Rolling element bearing fault diagnosis using wavelet packets. *NDT & E International*, vol. 35, no. 3, p. 197-205, **DOI:10.1016/S0963-8695(01)00044-5**.

[45] NI 9234 datasheet: from *http://www.ni.com/datasheet/pdf/en/ds-316*, accessed on 2016-02-04.

[46] PCB IMI 603C01 transducer, from *https://www.pcb.com/contentstore/docs/PCB_Corporate/IMI/Products/Manuals/603C01.pdf*, accessed on 2016-02-04.

Strojniški vestnik - Journal of Mechanical Engineering 63(2017)1, 15-24
DOI:10.5545/sv-jme.2016.3746
Original Scientific Paper
Received for review: 2016-05-20
Received revised form: 2016-08-06
Accepted for publication: 2016-09-06

Improvement of the Lubrication Performance of RBD Palm Stearin as an Alternative Lubricant under Different Sliding Speeds

Nurul Farhanah Azman* – Syahrullail Samion
University of Technology Malaysia, Faculty of Mechanical Engineering, Malaysia

Vegetable oils have gained global att–ention to be used as an alternative lubricant to reduce the dependency on natural resources of petroleum-based lubricants due to concern over environmental problems. In this study, a refined, bleached and deodorized (RBD) palm stearin was chosen as the base lubricant, and its lubrication performance was investigated using a pin-on-disk tribotester. A zinc dialkyl-dithiophosphate (ZDDP) additive in concentrations of 1 wt%, 3 wt% and 5 wt% was blended with RBD palm stearin to improve the lubrication performance of the base lubricant. Commercial semi-synthetic oil (SAE15W50) was used for comparison purposes. The experiments were conducted under various sliding speeds (1.5 ms^{-1}, 2.5 ms^{-1} and 3.5 ms^{-1}) under normal force of 9.81 N for an hour. The lubrication performance of the tested lubricants was presented by the coefficient of friction, wear scar diameter, wear rate, surface roughness and wear worn surface of the pin specimen. The results show that an increase in ZDDP concentrations has improved the lubrication performance of the RBD palm stearin. RBD palm stearin with 5 wt% ZDDP additive shows a smaller coefficient of friction than that of SAE15W50, but creates a slightly larger wear scar diameter and wear rate.

Keywords: RBD palm stearin, ZDDP, coefficient of friction, wear rate

Highlights

- *The lubrication performance of RBD palm stearin and its formulation were evaluated using a pin-on-disk tribotester.*
- *The influences of ZDDP additive concentrations on the lubrication performance of RBD palm stearin were determined.*
- *The results indicate that an increase in ZDDP concentrations has improved the lubrication performance of the RBD palm stearin.*
- *RBD palm stearin blended with 5 wt% of ZDDP shows an excellent friction-reducing performance than SAE15W50 does.*

0 INTRODUCTION

The majority of the lubricants currently in use are petroleum-based lubricants [1]. In 2004, approximately 37.4 million tonnes of lubricants [2], with 12 million tons of lubricant waste being released into the environment, were used [3]. Petroleum-based lubricants have a very high level of toxicity and are non-biodegradable which is harmful to the environment. Regarding environmental problem issues, vegetable oils have gained global attention to be used as an alternative lubricant. The use of these renewable resources will reduce the dependency on natural resources of petroleum-based lubricants [4].

Vegetable oils are the most suitable candidates to replace petroleum-based lubricants because they have many advantages, such as being renewable, biodegradable, non-toxic and contributing zero pollution [5]. Despite having environmental advantages, vegetable oils have limited oxidative stability and thermal stability. The presence of unsaturated fatty acid (C=C) makes the vegetable oils easily oxidized due to the existence of bis-allylic protons between two double bonds that is highly susceptible to radical attack [6]. The higher the number of double bonds or the higher the level of unsaturation value, the higher the tendency of vegetable oils to oxidize. Whereas, a higher level of saturation value causes poor low-temperature properties, including cloudiness, precipitation, poor flowability and solidification at low temperatures [6]. The formulation of vegetable oils with commercial additives will probably help in the improvement of the lubrication performance of vegetable oils as lubricants.

Previous research had shown that zinc dialkyl-dithiophosphate (ZDDP) improves the lubrication performance of vegetable oils. Jayadas et al. investigated the lubrication performance of pure coconut oil with and without the ZDDP additive [7]. Among other vegetable oils, coconut oil has much better oxidative and thermal stability due to its high degree of saturated fatty acid composition. They monitored the evaluation of lubrication performance using a four-ball tester and test rig. The results were compared with SAE20W50 commercial mineral oil. Their analysis revealed that the wear scar diameter (WSD) of pure coconut oil is larger than that of SAE20W50, although the coefficient of friction (COF) of coconut oil is much smaller. This is attributed to the continuous removal of metallic soap film during

*Corr. Author's Address: Faculty of Mechanival Engineering, Universiti Teknologi Malaysia, 81310 UTM Johor Bahru, Johor, Malaysia, nurulfarhanahazman@gmail.com

surface sliding, and it reacts chemically with metal surfaces resulting in poor protection against wear. This metallic soap film has low shear strength, resulting in low COF. However, when 2 wt% of ZDDP additive is added into the coconut oil, it improves both wear and friction performance. Sulphur and phosphorus content in ZDDP will form an iron sulphide and iron phosphide layer that is low in shear strength, hence preventing rapid oxidation and wear. ZDDP also acts as an antioxidant agent to prevent oxide formation on the metal surface.

Cheenkachorn discovered that the addition of 1 % ZDDP in soybean oil, epoxidized soybean oil, and high oleic soybean oil significantly reduces the coefficient of friction especially at lower temperatures [8]. It is thought that the desorption rate of the additive on the surface is higher than the adsorption rate at higher temperatures. The addition of additive effectively protects the rubbing surfaces since it can form a thin protective film with the attachment of a polar head to the metal and the non-polar ends can form a molecular layer. Mahipal et al. investigated the effectiveness of ZDDP as an additive in Karanja oil in terms of friction and wear performance [9]. Karanja oil added with 2 wt% ZDDP is the optimum concentration in reducing both COF and WSD. ZDDP effectively reduces friction and wear with the formation of the protective film, the elimination of corrosive peroxides and the disintegration of hard and abrasive iron oxides. However, it was found that further increases in ZDDP concentrations above 2 wt% cause an increase in friction and wear. This is due to excess zinc adsorption on the contact surface that will increase the friction, while the heavier structure of ZDDP will be attached to the metal surface resulting in larger WSD.

In this research, refined, bleached, and deodorized (RBD) palm stearin (PS) was used as a base lubricant, and its lubrication performance was evaluated using a pin-on-disk tribotester. ZDDP was selected because it is the most commonly used and cost effective multifunctional additive in engine oil formulation. According to Girotti et al., the typical composition of ZDDP in engine oil formulation is 3 %, which is present in antioxidant and antiwear additives [10]. The effectiveness of ZDDP additive in PS was also investigated in terms of their lubrication performance. The results were compared with commercial semi-synthetic oil (SAE15W50). In addition, the effect of sliding speeds condition on the lubrication performance is also present.

1 METHODS AND EXPERIMENTAL

Refined, bleached and deodorized (RBD) palm stearin was used in this research with a viscosity 38.01 mm^2s^{-1} at 40 °C and 8.55 mm^2s^{-1} at 100 °C, a viscosity index of 212.56, free fatty acid (as palmitic) 0.04 % and an iodine value of 35.2. Zinc dialkyl-dithiophosphate (ZDDP) additive was commercially purchased and blended at a concentration of 1 wt%, 3 wt% and 5 wt% with RBD palm stearin to improve its lubrication performance. Commercial semi-synthetic oil (SAE15W50) was used for comparison purposes with a viscosity of 112.9 mm^2s^{-1} at 40 °C and 20.9 mm^2s^{-1} at 100 °C, and a viscosity index of 211.89. RBD palm stearin has lower kinematic viscosity than SAE15W50 because it contains unsaturated fatty acid, and a high level of unsaturation results in lower kinematic viscosity [11]. The density of RBD palm stearin and SAE15W50 is 0.87 gcm^{-3} and 0.88 gcm^{-3}, respectively.

Lubrication performance of the tested lubricants was carried out using a pin-on-disk tribotester (pure aluminium A1100 vs. SKD11 tool steel disk) in accordance to ASTM G99. A hemispherical end pin-on-disk tribotester uses a nonconformal contact, which is suitable for such applications as wheels, bearings, traction drives, gears and cams [12]. Furthermore, nonconformal contact can avoid alignment problem during the test. This is because even small misalignments between the surfaces can result in uneven distribution of contact pressure and uneven trapping of wear debris or lubricants [13]. The selection of material for the pin and disk used in the present research to match prior experiments conducted by other researchers [14]. In addition, aluminium is a lightweight metal that has been widely used in automotive applications due to the need for improved fuel economy [15]. The material pair also was chosen to obtain most of the significant wear for the softer A1100 pin material, as compared to the harder SKD11 disk which is highly wear resistant. The scheme of the tribotester was presented in Fig. 1 which shows a stationary pin was in contact with the disk at a constant vertical force. The experiment ran at an applied load of 9.81 N for an hour of test duration with sliding speeds of 1.5 ms^{-1}, 2.5 ms^{-1} and 3.5 ms^{-1} at room temperature. A small amount of lubricant (2.5 ml) was placed on the disk surface, and the disk was designed to have a groove to prevent the lubricant from flowing out during the rotation of the disk. The disk was rotated at a specified speed creating a sliding contact, and frictional force sensor will measure the friction force. The data was presented in a data

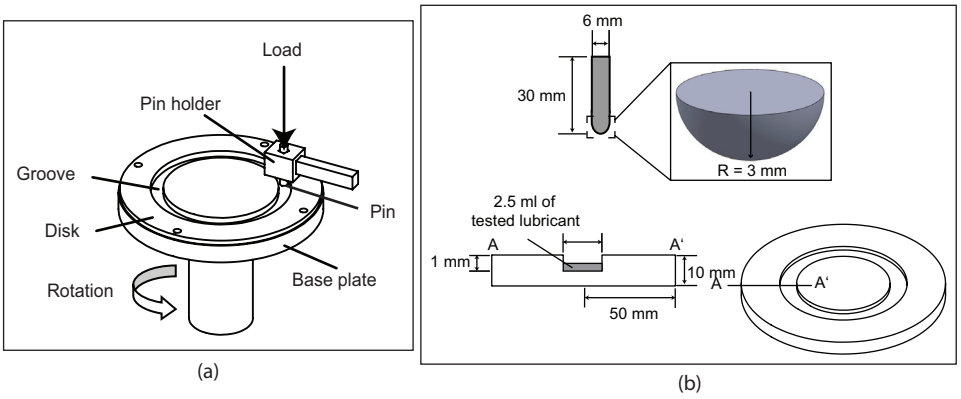

Fig. 1. *a) Schematic diagram of pin-on-disk and b) Geometry of the pin and disk*

acquisition system, and then the friction force value was used to calculate the coefficient of friction (COF). The COF was taken as a measure of the friction-reducing performance of the tested lubricants.

The mean contact Hertz pressure was calculated as in Eq. (1) **[16]**.

$$\bar{p} = \frac{1}{\pi}\left(\frac{4E'}{3R}\right)^{2/3} P^{1/3}, \tag{1}$$

where P is the normal load, R is the radius of curvature of the hemispherical end of the pin, E' is the effective elastic modulus which is equal to $\left(\left(1-\nu_1^2\right)/E_1+\left(1-\nu_2^2\right)/E_2\right)^{-1}$, where E_1 and ν_1 denote elastic modulus and Poisson's ratio for aluminium A1100 pin, E_2 and ν_2 denote elastic modulus and Poisson's ratio for the tool steel SKD11 disk. Given that E_1 = 75 GPa, ν_1 = 0.34, E_2 = 212.8 GPa and ν_2 = 0.28, the effective elastic modulus E' = 61.69 GPa; thus, mean contact Hertz pressure, $\bar{p}$ is 0.62 GPa.

The minimum film thickness was calculated using EHL equations as in Eq. (2) to determine the lubrication regime of a tribosystem.

$$H_{\min} = 3.63U^{0.68}G^{0.49}W^{-0.073}(1-e^{-0.68k}), \tag{2}$$

where U is the dimensionless speed parameter ($U=\left(\eta_0 V\right)/\left(E'R_x\right)$), where η_0 is the dynamic viscosity at 27 °C, V is the surface velocity of the disk, E' is the effective modulus of elasticity, R_x is the curvature of the pin. G is the dimensionless materials parameter ($G=\alpha E'$), where α is the viscosity-pressure coefficient. W is the dimensionless load parameter ($W=F/\left(E'R_x^2\right)$) where F is the normal load exerted on the pin, and k is the elliptical parameter ($k=R_y/R_x$) where R_y is the elliptical contact in the y-direction and R_x is the elliptical contact in x-direction **[17]** and **[18]**.

After calculating the minimum film thickness, $h_{\min}$, Eq. (3) the lubrication regime can be calculated by determining the dimensionless film parameter, also called lambda ratio, seen in Eq. (4).

$$h_{\min} = H_{\min}\cdot R_x, \tag{3}$$

$$\lambda = \frac{h_{\min}}{\sqrt{R_{q1}^2+R_{q2}^2}}, \tag{4}$$

where R_{q1} and R_{q2} are the root mean square roughness of the two solid surfaces. In the present study, the value of rms roughness of pin and disk are 0.43 μm and 0.35 μm respectively. The range of λ for the lubrication regimes are boundary lubrication $\lambda \leq 1$; mixed lubrication $3>\lambda>1$ and full film lubrication $\lambda \geq 3$ **[18]**.

Information for geometry and calculated lubricant constants are given in Table 1. The dynamic viscosity, η_0 at 27 °C for each tested lubricant is given by $\eta_{(\text{SAE15W50})}$ = 0.172 Pa·s, and $\eta_{(\text{RBD palm stearin})}$ = 0.152 Pa·s. The calculated minimum film thickness and lubricant regime for the tested lubricants at speed varying from 1.5 ms^{-1} to 3.5 ms^{-1} are shown in Table 2.

Table 1. *Geometry and calculated lubricant constants*

R_x	0.003 m
E'	6.169×10^{10} Pa
k	1.0339
α	2.1×10^{-8} Pa
G	1279

The anti-wear performance of the tested lubricants was measured by taking the wear scar diameter (WSD) and calculating the wear rate. The WSD of the pin was measured by using an optical microscope to calculate the wear volume (V) as in Eq.

(5) [19], then the value was used to calculate the wear rate as in Eq. (6) [20].

Table 2. *Calculated minimum film thickness and lubricant regime at speed varying from 1.5 ms^{-1} to 3.5 ms^{-1}*

Lubricants	Speed [ms^{-1}]	h_{min} [μm]	λ	Lubrication regime
SAE15W50	1.5	0.3869	0.6979	Boundary lubrication
	2.5	0.5477	0.9878	Boundary lubrication
	3.5	0.6884	1.2417	Mixed lubrication
RBD palm stearin	1.5	0.3557	0.6416	Boundary lubrication
	2.5	0.5035	0.9081	Boundary lubrication
	3.5	0.6329	1.1416	Mixed lubrication

$$V = \frac{\pi r^4}{4R}, \tag{5}$$

where; r is the radius of pin wear scar [mm], and R is original pin radius [mm].

$$k = \frac{V}{SF}, \tag{6}$$

where k is the wear rate [mm^{3}N^{-1}m^{-1}], V is the volume of material removed by wear [mm^3], S is the sliding distance [m], and F is the applied force [N].

Surface roughness and wear worn surfaces of the pin specimen were obtained using a surface profiler and high-resolution optical microscope. The present study only considered the arithmetic mean surface roughness (Ra) value for analysis purposes since this is a good parameter in which the conditions are always the same. To ensure there was no excess oil on the pin surface, the pins were cleaned with acetone after each test.

2 RESULTS AND DISCUSSION

2.1 Friction-Reducing Performance

The experiments were conducted at different sliding speeds, at 1.5 ms^{-1}, 2.5 ms^{-1} and 3.5 ms^{-1}, respectively, in order to study the friction-reducing performance of RBD palm stearin with and without a ZDDP additive. The pin-on-disk tribotester was run at 9.81 N for an hour. A ZDDP additive of 1 wt%, 3 wt%, and 5 wt% was added into RBD palm stearin to improve its lubrication performance. The friction-reducing performance of the RBD palm stearin with and without the ZDDP additive was compared to a commercial semi-synthetic oil (SAE15W50). The coefficient of friction (COF) was calculated by dividing the frictional force by the normal load and plotted against the sliding speed in Fig. 2.

It can be seen from the graphs that the COF increased with an increase in the sliding speed, except for PS+5 wt% ZDDP. It was found that RBD palm stearin (PS) had a significantly larger COF in comparison to SAE15W50. It is thought that the high content of unsaturated fatty acid in PS may have contributed to the higher COF. It is widely known that vegetable oils with a high content of unsaturated fatty acid have a low resistance to oxidative degradation. According to Joseph and Sharma, vegetable oils follow the same free radical oxidation as hydrocarbon mineral oil does, but it oxidizes at a faster rate [21]. As has been noted, PS, being highly susceptible to oxidation, is unable to provide a stable lubricant film to prevent metal surfaces from coming into contact with each other, hence increasing the friction. Additionally, PS did not seem to be effective in reducing friction because it remained in a semi-solid state at room temperature when the experiment was being conducted. It is widely accepted that a higher viscosity will generate a thicker tribofilm, hence providing better lubrication performance. However, in this case, the viscosity of PS was too thick, thus resulting in greater heat generation. The heat generated eventually raised the rate of oxidation, thus generating more wear debris on the metal surface and the oxidation of the debris will eventually raise the COF [22].

The figure also showed that an increase in the additive concentration improved the friction-reducing performance of PS. It is clear from Fig. 2 that the friction-reducing performance of PS+5 wt% ZDDP (0.039) was comparable to that of SAE15W50 (0.035) at a low sliding speed, while at 3.5 ms^{-1}, PS+5 wt% ZDDP (0.036) gave a better friction-reducing performance than SAE15W50 (0.067) did. It was evident that the ZDDP was responsible for protecting the PS from oxidation, thus resulting in a better friction-reducing performance by the lubricating oil. ZDDP has long been recognized for its ability as an antioxidant to resist oxidation degradation. ZDDP functions both as a radical scavenger and as a peroxide decomposer [23]. It inhibits the formation of free radicals by breaking the chains that react with the radicals in order to form stable compounds that prevent further propagation of the free radical chain. ZDDP also reacts with hydroperoxide molecules during the oxidation process to prevent the formation of peroxy radicals. The presence of organic molecules such as zinc, phosphorus, and sulphur in ZDDP make it a powerful antioxidant since these organic molecules bond to the surface of the metal to form a protective coating. Sulphur and phosphorus compounds will also

react with metal surfaces to form a low shear strength film, thus reducing the COF [24].

Furthermore, it can be seen in Fig. 2 that the friction behaviour of PS+5 wt% ZDDP was not significantly affected by the sliding speed, where the average coefficient of friction of the various sliding speeds was 0.037, which indicated the best friction-reducing performance. This suggests that at a concentration of 5 wt%, the ZDDP provided a lubricant film on the surface of the metal and this film was maintained at various sliding speeds, thereby maintaining the COF. The ZDDP was dominant at this concentration and acted as a "friction modifier" in PS. The ZDDP additive in vegetable oil exhibited a good friction-reducing ability in comparsion to vegetable oil alone because the chemical adsorption of the ZDDP additive to the metal surface was stronger than the physical adsorption of vegetable oil on the surface [8].

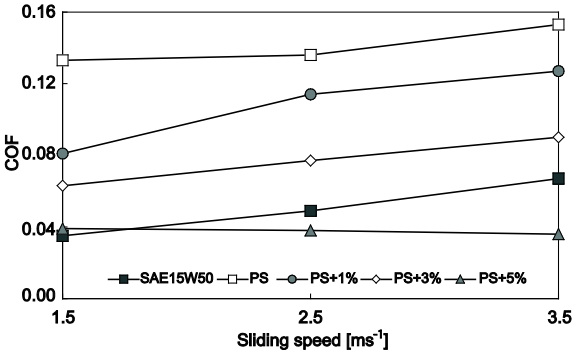

Fig. 2. *Effects of sliding speed on coefficient of friction*

2.2 Anti-Wear Performance

The wear scar diameter (WSD) of the pin surfaces was measured using an optical microscope, and the values were plotted against the sliding speed, as shown in Fig. 3. The wear rate was also calculated using Eq. (2) and the data were tabulated in Table 3. Fig. 3 shows no clear trend with regard to the WSD at different sliding speeds, but when calculating the wear rate of the pin, as shown in Table 3, it was indicated that the wear rate decreased with an increase in the sliding speed. Fig. 2 shows that the COF increased with an increase in the sliding speed, but the wear rate is decreasing (see Table 3). An increase in the sliding speed usually leads to heat generation in the contact region, where an increase in temperature will result in more oxidation. Wear debris will form during abrasion, where oxidation of the debris will eventually raise the COF [22]. However, a rise in temperature will cause the formation of an oxide layer. It was observed in some previous research that this oxide film offers a certain amount of protection from wear [25] and [26]. This is possibly the reason that an increase in sliding speed will reduce the wear rate.

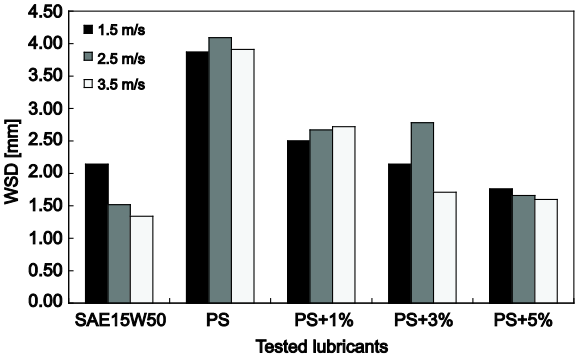

Fig. 3. *Effects of sliding speed on wear scar diameter (WSD)*

Table 3. *Wear rate of the tested lubricants under different sliding speeds*

Tested lubricants	Wear rate $\times 10^{-5}$ [mm^{3}N^{-1}m^{-1}]		
	1.5 ms^{-1}	2.5 ms^{-1}	3.5 ms^{-1}
SAE15W50	0.65	0.10	0.04
PS	6.93	5.19	3.09
PS+1 wt% ZDDP	1.21	0.94	0.73
PS+3 wt% ZDDP	0.65	1.11	0.11
PS+5 wt% ZDDP	0.30	0.14	0.09

It can be seen that the addition of 1 wt% ZDDP into the PS significantly reduced the wear rate of the specimen pin. This result indicated that ZDDP effectively reduced the wear. A further increase in the ZDDP concentration slightly reduced the wear rate of the specimen pin. The anti-wear performance of PS+5 wt% ZDDP (1.76 mm) was comparable to that of SAE15W50 (2.14 mm) at a low sliding speed. However, PS+5 wt% ZDDP (1.60 mm) created a slightly larger WSD than SAE15W50 (1.34 mm) at a sliding speed of 3.5 ms^{-1}.

PS showed a larger WSD and wear rate in comparison to SAE15W50 due to its high content of unsaturated fatty acid, which resulted in poor oxidative stability due to the C=C bonds that functioned as active sites for the oxidation reactions. The oxidation of vegetable oil will increase the viscosity of the oil, thereby forming numerous deposits in the oil. These results correspond with the findings by de Almeida et al., where the use of refined palm oil at ambient temperature caused the formation of many deposits due to the high viscosity [27]. The addition of ZDDP to the PS reduced the WSD and wear rate of the

specimen pin. This was attributed to the protection of the lubricant against oxidation and preventing the formation of deposits in the oil. The addition of 5 wt% ZDDP to PS provided good protection against wear as it possessed anti-wear properties comparable to that of SAE15W50.

2.3 Surface Analysis

2.3.1 Surface Roughness Characteristics

Fig. 4 shows the arithmetic mean deviation of the surface roughness (*Ra*) against the sliding speed. The plots show a positive slope with increasing sliding speed. PS generated a coarser surface roughness due to the removal of the soap film by the continuous rubbing of the contact surfaces. The destruction of this soap film caused greater metal-to-metal contact and generated deeper scratches on the pin surface. This phenomenon was related to the oxidation process that occurred on the metal surfaces because the unsaturated fatty acid in PS easily absorbed oxygen and hence, affected the reactions within the lubricant [28]. When oxidation occurs, there is a high tendency for the formation of deposits, which will cause deeper scratches on the pin surface. In addition, Autay et al. explained that wear debris essentially has an abrasive action, but its chemical composition is responsible for the presence of oxides [22]. The wear debris was embedded on the pin surface, thus increasing the surface roughness value.

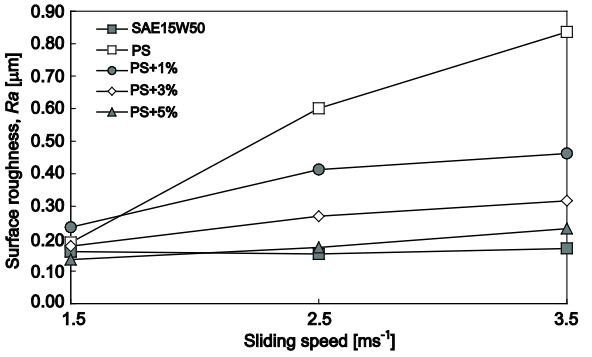

Fig. 4. *Effects of sliding speed on surface roughness*

The addition of ZDDP into PS had a positive effect on the surface protection, where PS produced a smoother surface with an increase in the ZDDP concentration. Fig. 4 shows PS with 5 wt% ZDDP additive only had a similar surface roughness with SAE15W50 at a sliding speed of 1.5 ms^{-1}. At this sliding speed condition, the addition of 1 wt% ZDDP increased the surface roughness of PS, but the surface roughness of the pin became smoother as the concentration of ZDDP increased. Meanwhile, at sliding speeds of 2.5 ms^{-1} and 3.5 ms^{-1}, the surface roughness was reduced as the ZDDP concentration increased. The presence of ZDDP in the PS contributed to the prevention of rapid oxidation, hence minimizing the rate of the removal of the soap film, resulting in a smoother surface.

2.3.2 Worn Wear Surface Characteristics

Further confirmation of the wear behaviour of the pin surfaces lubricated with commercial semi-synthetic oil and RBD palm stearin with and without additive was obtained by analysing the wear worn surface. Both the worn wear surface and slider profile of the pins were taken by using a high-resolution microscope. Figs. 5 to 7 show the worn wear surfaces and the surface profile of the rubbing surfaces lubricated with a commercial semi-synthetic oil (SAE15W50), an RBD palm stearin (PS), PS + 1 wt% ZDDP, PS + 3 wt% ZDDP and PS + 5 wt% ZDDP at various sliding speeds (1.5 ms^{-1}, 2.5 ms^{-1} and 3.5 ms^{-1}), respectively. The surface slider profile corroborates the COF, where the steeper peak means that there is a larger amount of material removed. This also represents a deeper abrasive groove on the worn surface of the pin specimen.

It was observed that at all speed conditions, the PS generated deeper scratches on the worn surfaces and severe wear occurred at sliding speeds of 2.5 ms^{-1} and 3.5 ms^{-1}. The darker region on the pin surface represents the oxidation. These deep scratches were apparently caused by the breakdown of the lubricant film, which was probably due to the occurrence of oxidation on the metal surfaces. This oxidation will eventually weaken the metal surface and cause more material to be removed. The ZDDP additive helped to overcome this problem by acting as an antioxidant agent in PS. With increasing ZDDP concentrations, less abrasive grooves appeared on the worn surfaces. The presence of ZDDP made the PS more resistant to oxidation; therefore, it had a lesser tendency to cause the removal of more material. It is evident that ZDDP effectively formed a lubricant film, which protected the metal surface from rapid oxidation, thus resulting in less material removal and smoother worn surfaces. This phenomenon was confirmed by the results of the friction and surface roughness measurement. It was shown that increasing the ZDDP concentrations reduced both the COF and surface roughness values.

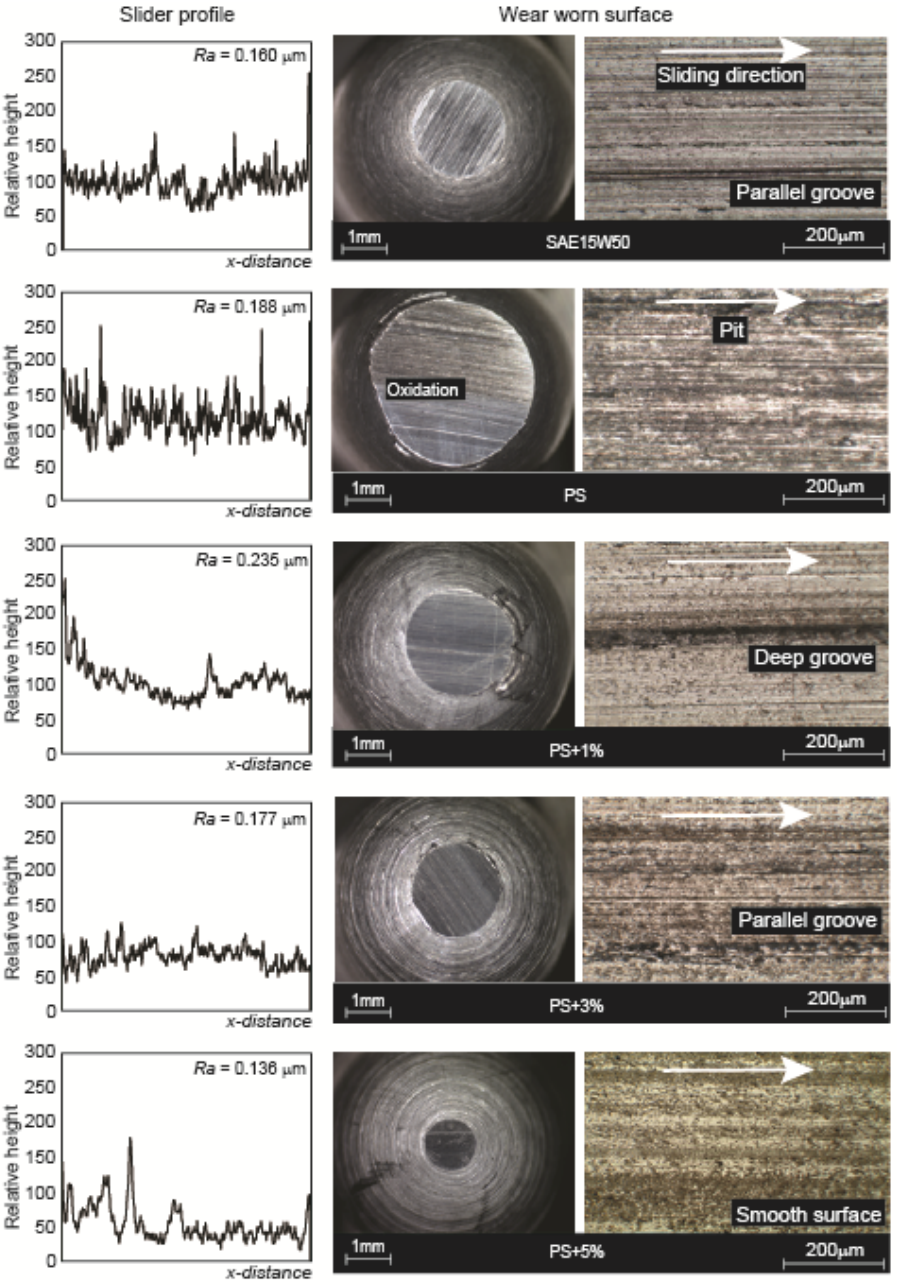

Fig. 5. *Worn wear surfaces and surface profile under 1.5 ms^{-1} sliding speed*

3 CONCLUSIONS

The lubrication performance of RBD palm stearin with and without ZDDP additive have been evaluated using a pin-on-disk tribotester. Commercial semi-synthetic oil (SAE15W50) was used for comparison purposes. The result shows that without ZDDP additive, RBD palm stearin generated a larger coefficient of friction and wear scar diameter than that of SAE15W50. The presence of a ZDDP additive in an RBD palm stearin improves both the friction-reducing and anti-wear properties of the lubricant, where an increase in ZDDP concentrations improves both properties. An RBD palm stearin with a 5 wt% ZDDP additive shows a lower coefficient of friction compared to that of an SAE15W50 at various sliding speeds, but it creates a slightly larger wear scar diameter and rougher pin surfaces. In addition, surface wear analysis with an optical microscope shows abrasive wear as the dominant wear mechanism for both with

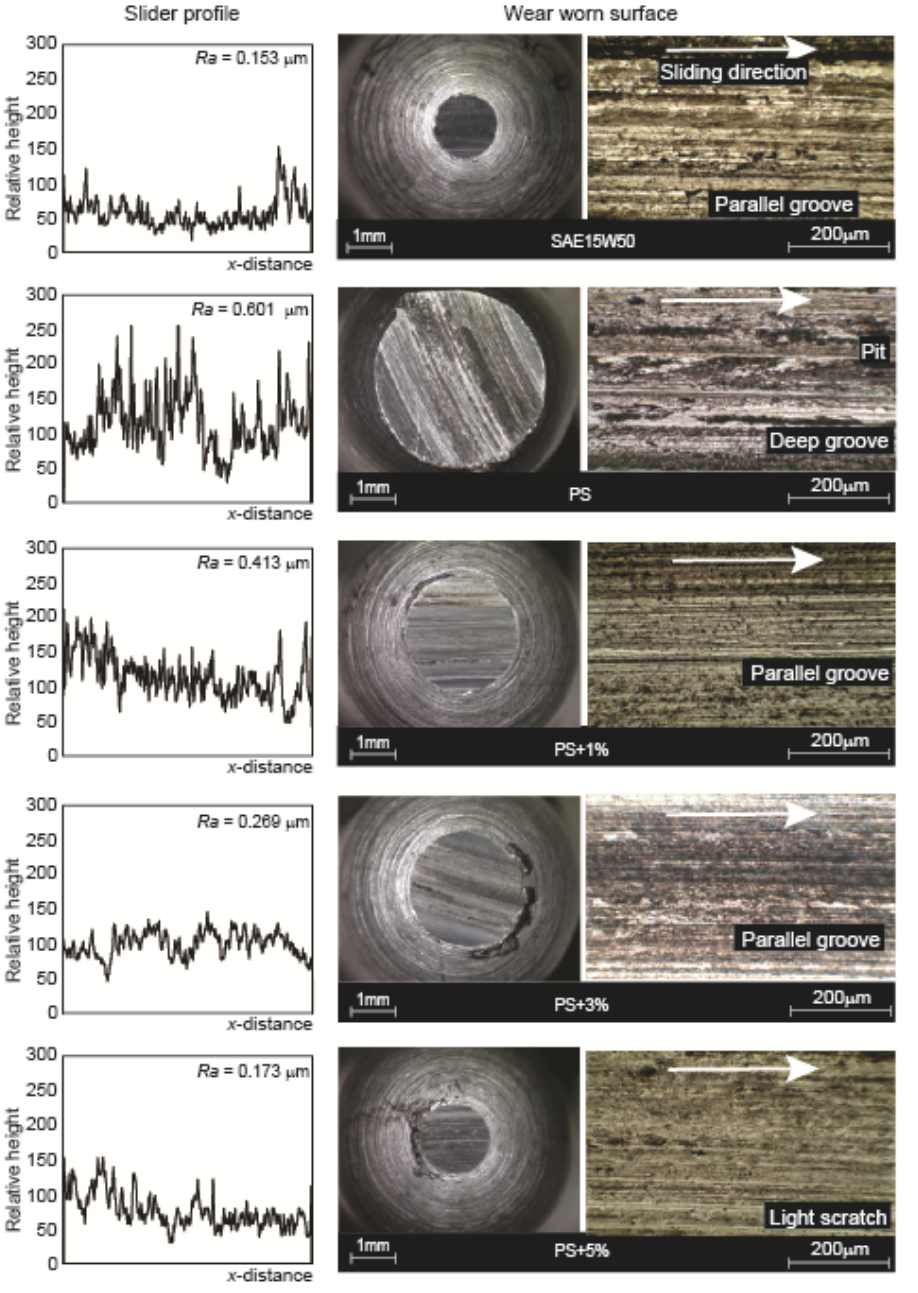

Fig. 6. *Worn wear surfaces and surface profile under 2.5 ms^{-1} sliding speed*

and without a ZDDP additive in an RBD palm stearin and SAE15W50. A pure RBD palm stearin shows that oxidation occurs, which is represented by the existence of a darker region on the worn surfaces. An increase in ZDDP concentrations showed less abrasive grooves appeared on the worn surfaces. In the present research, commercial semi-synthetic oil (SAE15W50) was used for comparison purposes to ensure that vegetable based oil formulations provide at least the same tribological performance as engine oil formulation for automotive applications. However, there is still a need to examine other properties such as oxidative and thermal stability of the formulated RBD palm stearin to be a competitive lubricant in automotive applications. Future work should be undertaken to investigate the oxidative and thermal stability of the formulated RBD palm stearin.

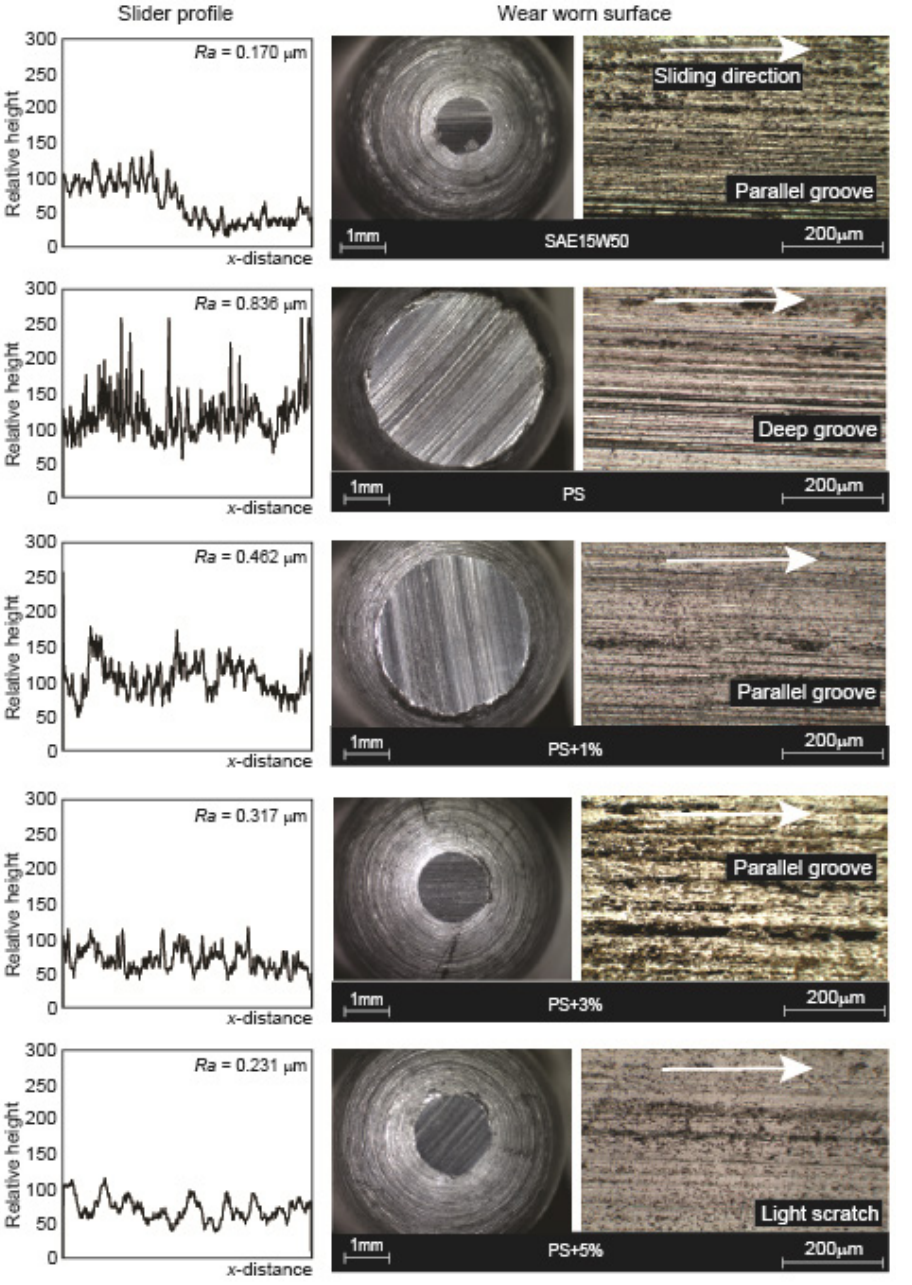

Fig. 7. *Worn wear surfaces and surface profile under 3.5 ms^{-1} sliding speed*

4 ACKNOWLEDGEMENTS

The authors wish to thank the Faculty of Mechanical Engineering at the Universiti Teknologi Malaysia for their support and cooperation during this study. The authors also wish to thank the Research Management Centre (RMC) for the Research University Grant (02G34, 02G35, 09H64) from the Universiti Teknologi Malaysia and Fundamental Research Grant Scheme (4F610) from the Ministry of Higher Education for their financial support.

5 REFERENCES

[1] Joseph, P.V., Saxena, D., Sharma, D.K. (2007). Study of some non-edible vegetable oils of Indian origin for lubricant application. *Journal of Synthetic Lubrication*, vol. 24, no. 4, p. 181-197, **DOI:10.1002/jsl.39**.

[2] Nagendramma, P., Kaul, S. (2012). Development of ecofriendly/biodegradable lubricants: An overview. *Renewable and Sustainable Energy Reviews*, vol. 16, no. 1, p. 764-774, **DOI:10.1016/j.rser.2011.09.002**.

[3] Chiong Ing, T., Rafiq, A.K.M., Azli, Y., Syahrullail, S. (2012). Tribological behaviour of refined bleached and deodorized palm olein in different loads using a four-ball tribotester. *Scientia Iranica*, vol. 19, no. 6, p.1487-1492, **DOI:10.1016/j.scient.2012.10.027**.

[4] Syahrullail, S., Azwadi, C.S.N., Ing, T.C. (2011). The metal flow evaluation of billet extruded with RBD palm stearin. *International Review of Mechanical Engineering*, vol. 5, no. 1, p. 21-27.

[5] Shahabuddin, M., Masjuki, H.H., Kalam, M.A., Bhuiya, M.M.K., Mehat, H. (2013). Comparative tribological investigation of bio-lubricant formulated from a non-edible oil source (Jatropha oil). *Industrial Crops and Products*, vol. 47, p. 323-330, **DOI:10.1016/j.indcrop.2013.03.026**.

[6] Erhan, S.Z., Sharma, B.K., Liu, Z., Adhvaryu, A. (2008). Lubricant base stock potential of chemically modified vegetable oils. *Journal of Agricultural and Food Chemistry*, vol. 56, no. 19, p. 8919-8925, **DOI:10.1021/jf801463d**.

[7] Jayadas, N.H., Prabhakaran Nair, K., Ajithkumar, G. (2007). Tribological evaluation of coconut oil as an environment-friendly lubricant. *Tribology International*, vol. 40, no. 2, p. 350-354, **DOI:10.1016/j.triboint.2005.09.021**.

[8] Cheenkachorn, K. (2013). A study of wear properties of different soybean oils. *Energy Procedia*, vol. 42, p. 633-639, **DOI:10.1016/j.egypro.2013.11.065**.

[9] Mahipal, D., Krishnanunni, P., Rafeekh, M.P., Jayadas, N.H. (2014). Analysis of lubrication properties of zinc-dialkyl-dithiophosphate (ZDDP) additive on Karanja oil (Pongamia pinnatta) as a green lubricant. *International Journal of Engineering Research*, vol. 3, no. 8, p. 494-496, **DOI:10.17950/ijer/v3s8/804**.

[10] Girotti, G., Raimondi, A., Blengini, G.A., Fino, D. (2011). The contribution of lube additives to the life cycle impacts of fully formulated petroleum-based lubricants. *American Journal of Applied Science*, vol. 8, no. 11, p. 1232-1240, **DOI:10.3844/ajassp.2011.1232.1240**.

[11] Garcés, R., Martínez-Force, E., Salas, J.J. (2011). Vegetable oil basestocks for lubricants. *Grasas y Aceites*, vol. 62, no. 1, p. 21-28, **DOI:10.3989/gya.045210**.

[12] Fajdiga, G. (2015). Computational fatigue analysis of contacting mechanical elements. *Tehnički vjesnik - Technical Gazette*, vol. 22, no. 1, p. 169-175, **DOI:10.17559/TV-20140429122305**.

[13] Blau, P.J. (2008). *Friction Science and Technology from Concept to Applications*. Taylor and Francis Group, United States, **DOI:10.1201/9781420054101**.

[14] Nuraliza, N., Syahrullail, S. (2016). Tribological effects of vegetable oil as alternative lubricant: A pin-on-disk tribometer and wear. *Tribology Transactions*, vol. 59, no. 5, p. 831-837, **DOI:10.1080/10402004.2015.1108477**.

[15] Miller, W.S., Zhuang, L., Bottema, J., Wittebrood, A.J., De Smet, P., Haszler, A., Vieregge, A. (2000). Recent development in aluminium alloys for the automotive industry. *Materials Science and Engineering: A*, vol. 280, no. 1, p. 37-49, **DOI:10.1016/S0921-5093(99)00653-X**.

[16] Chawan, A.D., Chakravartula, A.M., Zhou, J., Pruitt, L.A., Ries, M., Komvopoulos, K. (2002). Effects of counterface roughness and conformity on the tribological performance of crosslinked and non-crosslinked medical-grade ultra-high molecular weight polyethylene. *Materials Research Society Symposium Proceedings*, vol. 724, p. 95-100, **DOI:10.1557/PROC-724-N5.10**.

[17] Kabir, M.A., Higgs, C.F., Lovell, M.R. (2008). A pin-on-disk experimental study on a green particulate-fluid lubricant. *Journal of Tribology*, vol. 130, no. 4, p. 041801, **DOI:10.1115/1.2908913**.

[18] Zulkifli, N.W.M., Masjuki, H.H., Kalam, M.A., Yunus, R., Azman, S.S.N. (2014). Lubricity of bio-based lubricant derived from chemically modified jatropha methyl ester. *Jurnal Tribologi*, vol. 1, p. 18-39.

[19] Oğuz, H., Düzcükoğlu, H., Ekinci, Ş. (2011). The investigation of lubrication properties performance of euro-diesel and biodiesel. *Tribology Transactions*, vol. 54, no. 3, p. 449-456, **DOI:10.1080/10402004.2011.556315**.

[20] Chen, C., Bosse, H., Deters, L. (2009). Effects of various base oils and additives on the tribological behaviour of lubricated aluminium- on-aluminium and steel-on-aluminium contacts. *Proceedings of the Institution of Mechanical Engineers, Part J: Journal of Engineering Tribology*, vol. 223, no. 3, p. 571-580, **DOI:10.1243/13506501JET511**.

[21] Joseph, P.V., Sharma, D.K. (2010). Improvement of thermooxidative stability of non-edible vegetable oils of indian origin for biodegradable lubricant application. *Lubrication Science*, vol. 22, no. 4, p. 149-161, **DOI:10.1002/ls.116**.

[22] Autay, R., Kchaou, M., Dammak, F. (2012). Friction and wear behavior of steels under different reciprocating sliding conditions. *Tribology Transactions*, vol. 55, no. 5, p. 590-598, **DOI:10.1080/10402004.2012.684427**.

[23] Barnes, A.M., Bartle, K.D., Thibon, V.R.A. (2001). A Review of zinc dialkyldithiophosphates (ZDDPS): characterisation and role in the lubricating oil. *Tribology International*, vol. 34, no. 6, p. 389-395, **DOI:10.1016/S0301-679X(01)00028-7**.

[24] Rohatgi, P.K., Tabandeh-Khorshid, M., Omrani, E., Lovell, M.R., Menezes, P.L. (2013). *Tribology for Scientists and Engineers*. p. 294-340, Springer, New York.

[25] Gunes, I., Uygunoglu, T., Erdogan, M. (2015). Effect of sintering duration on some properties of pure magnesium. *Powder Metallurgy and Metal Ceramics*, vol. 54, no. 3, p. 156-165, **DOI:10.1007/s11106-015-9693-8**.

[26] Syahrullail, S., Ismail, M.S.J. (2013). Lubrication performance of double fraction palm olein using pin-on-disk tribotester. IOP Conference Series: Materials Science and Engineering, vol. 50, no. 1, p. 012002, **DOI:10.1088/1757-899X/50/1/012002**.

[27] de Almeida, S.C.A., Belchior, C.R., Nascimento, M.V.G., Veira, L. dos S.R., Fleury, G. (2002). Performance of a diesel generator fuelled with palm oil. *Fuel*, vol. 81, no. 16, p. 2097-2102, **DOI:10.1016/S0016-2361(02)00155-2**.

[28] Masjuki, H.H., Maleque, M.A. (1996). The effect of palm oil diesel fuel contaminated lubricant on sliding wear of cast irons against mild steel. *Wear*, vol. 198, no. 1-2, p. 293-299, **DOI:10.1016/0043-1648(96)07208-0**.

Strojniški vestnik - Journal of Mechanical Engineering 63(2017)1, 25-34
DOI:10.5545/sv-jme.2016.3526
Original Scientific Paper
Received for review: 2016-02-23
Received revised form: 2016-06-01
Accepted for publication: 2016-07-14

Linear and Quadratic Solid-Shell Elements for Quasi-Static and Dynamic Simulations of Thin 3D Structures: Application to a Deep Drawing Process

Peng Wang – Hocine Chalal – Farid Abed-Meraim*
Arts et Métiers ParisTech, LEM3, France

A family of prismatic and hexahedral solid–shell (SHB) elements, with their linear and quadratic versions, is proposed in this work to model thin structures. The formulation of these SHB elements is extended to explicit dynamic analysis and large-strain anisotropic plasticity on the basis of a fully three-dimensional approach using an arbitrary number of integration points along the thickness direction. Several special treatments are applied to the SHB elements in order to avoid all locking phenomena and to guarantee the accuracy and efficiency of the simulations. These solid-shell elements have been implemented into ABAQUS standard/quasi-static and explicit/dynamic software packages. A number of static and dynamic benchmark problems, as well as a simulation of the deep drawing of a cylindrical cup, have been conducted to assess the performance of these SHB elements.

Keywords: assumed-strain method, finite elements, linear and quadratic solid–shell, quasi-static and dynamic, thin 3D structures, deep drawing

Highlights

- *A family of linear and quadratic (prismatic and hexahedral) solid–shell elements is proposed.*
- *The element formulation is extended to advanced large-strain anisotropic elastoplasticity.*
- *The validation of the proposed elements is extended to both quasi-static and dynamic analyses.*
- *The performance of these elements is evaluated through a complex deep drawing process simulation.*

0 INTRODUCTION

In modern industry, the finite element analysis has become an essential approach in the analysis of complex engineering processes. The accurate and efficient simulation of thin structures has motivated a number of researchers to develop advanced finite element technologies. Among these, the solid–shell concept **[1]** and **[2]** has emerged in recent decades for the efficient modelling of thin 3D structures **[3]** and **[4]**, while accurately describing the various non-linear phenomena **[5]** and **[6]**. The formulation of solid–shell elements is based on the reduced-integration technique, which makes them very attractive due to their low computational cost. However, they require special numerical treatments to avoid several locking phenomena. Among these techniques, the assumed strain method (ASM) has been used in **[7]** to eliminate locking modes. The enhanced assumed strain (EAS) technique is also widely used in the formulation of solid–shell elements, which is based on the inclusion of additional deformation modes for removing locking problems **[2]**, **[8]** and **[9]**. The EAS technique is often combined with the assumed natural strain (ANS) method in order to prevent most locking phenomena **[4]**, **[10]** and **[11]**. The concept of solid–shell elements has been widely adopted in the analysis of non-linear elastic and elastic-plastic thin structures, and it has been recently extended to the modelling of laminates **[12]** and **[13]**, and multilayer sandwich structures **[14]**.

In the current contribution, four assumed-strain based solid-shell (SHB) elements are proposed. They consist of linear prismatic (SHB6) **[15]** and hexahedral (SHB8PS) **[1]** and **[7]** elements, and their quadratic counterparts (SHB15) and (SHB20) **[16]** and **[17]**, respectively. These SHB elements are formulated within a three-dimensional framework with large displacements and rotations. An in-plane reduced-integration scheme with an arbitrary number of integration points along the thickness is adopted, which allows modelling thin structures with only a single element layer. The spurious zero-energy modes that are inherent in the reduced-integration technique are stabilized with a special procedure, while most locking phenomena are eliminated using an appropriate projection of the discrete gradient operator. The resulting SHB elements are coupled with three-dimensional anisotropic elastic–plastic constitutive models for metallic materials and then implemented into the ABAQUS standard/quasi-static and explicit/dynamic software packages. Several quasi-static and dynamic benchmark tests, which induce geometric and material nonlinearities, are first conducted to evaluate the performance of the SHB

*Corr. Author's Address: LEM3, UMR CNRS 7239 - Arts et Métiers ParisTech, 4, rue Augustin Fresnel, 57078 Metz Cedex 03, France, farid.abed-meraim@ensam.eu

elements. Next, attention is focused on the simulation of a complex deep drawing process involving large strains, anisotropic plasticity, and contact.

1 BASIC CONCEPTS OF THE SHB ELEMENTS

A unified formulation for the linear hexahedral SHB8PS and prismatic SHB6 solid–shell elements, as well as their quadratic counterparts SHB20 and SHB15, is briefly presented in this section. The current developments extend and enlarge the earlier quasi-static formulations of the SHB elements [7], [15] and [16]. Note that the earlier formulations of the linear prismatic element SHB6 [15] and the quadratic elements SHB15 and SHB20 [16] have been restricted to small-strain analysis and linear elastic behaviour. In this paper, all of the SHB elements are extended to explicit dynamic analysis, as well as being coupled with advanced large-strain anisotropic plasticity models, for the analysis of quasi-static and dynamic structural problems as well as sheet metal forming processes.

1.1 Definition of the Element Reference Geometry

Fig. 1 shows the reference geometry of all SHB elements with the location of their integration points. In the element reference frame, direction ζ denotes the thickness, along which multiple integration points can be used. In general, only two integration points along the thickness direction are sufficient to model elastic problems, while five integration points are recommended for non-linear (elastic–plastic) problems.

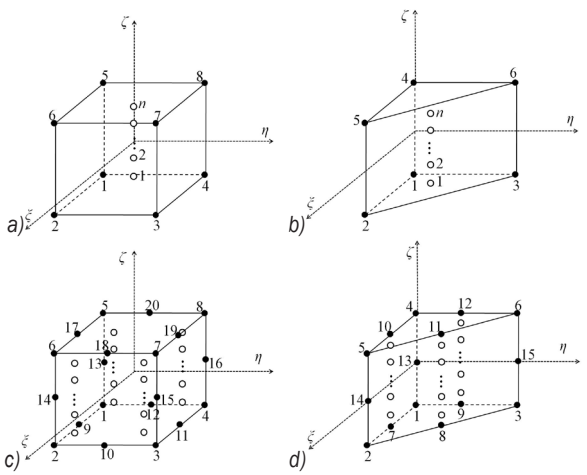

Fig. 1. *Reference geometry of the SHB elements and location of their integration points: a) linear hexahedral SHB8PS element; b) linear prismatic SHB6 element; c) quadratic hexahedral SHB20 element, and d) quadratic prismatic SHB15 element*

1.2 Quasi-Static Framework

The classical isoparametric linear and quadratic interpolation functions for standard hexahedral and prismatic elements are adopted in the formulation of the SHB elements. Accordingly, the three-dimensional position and displacement of any point inside the element, x_i and $u_i (i=1,2,3)$ respectively, can be defined using the interpolation functions $N_I (I=1,2,...,n)$ as:

$$x_i = x_{iI} N_I(\xi,\eta,\zeta) = \sum_{I=1}^{n} x_{iI} N_I(\xi,\eta,\zeta), \tag{1}$$

$$u_i = d_{iI} N_I(\xi,\eta,\zeta) = \sum_{I=1}^{n} d_{iI} N_I(\xi,\eta,\zeta), \tag{2}$$

where x_{iI} and d_{iI} denote the I^{th} nodal coordinate and displacement, respectively. The lowercase subscript i represents the spatial coordinate directions, while n indicates the number of nodes per element.

Next, the discrete gradient operator $\mathbf{B}$ defining the relationship between the strain field $\nabla_s(\boldsymbol{u})$ and the nodal displacement field $\mathbf{d}$ is given by:

$$\nabla_s(\boldsymbol{u}) = \mathbf{B} \cdot \mathbf{d}. \tag{3}$$

The SHB element formulation is based on the assumed-strain method, which corresponds to the simplified form of the Hu-Washizu variational principle proposed by Simo and Hughes [18]:

$$\pi(\dot{\bar{\boldsymbol{\varepsilon}}}) = \int_{\Omega_e} \delta \dot{\bar{\boldsymbol{\varepsilon}}}^T \cdot \boldsymbol{\sigma} \, d\Omega - \delta \dot{\mathbf{d}}^T \cdot \mathbf{f}^{ext} = 0, \tag{4}$$

where δ represents a variation, $\dot{\bar{\boldsymbol{\varepsilon}}}$ the assumed-strain rate, $\boldsymbol{\sigma}$ the Cauchy stress tensor, $\dot{\mathbf{d}}$ the nodal velocities, and $\mathbf{f}^{ext}$ the external nodal forces. The assumed-strain rate $\dot{\bar{\boldsymbol{\varepsilon}}}$ is defined using a $\bar{\mathbf{B}}$ matrix, which is obtained by projecting the classical discrete gradient operator $\mathbf{B}$ involved in Eq. (3):

$$\dot{\bar{\boldsymbol{\varepsilon}}} = \bar{\mathbf{B}} \cdot \dot{\mathbf{d}}. \tag{5}$$

Inserting Eq. (5) into the variational principle (Eq. (4)), the element stiffness matrix $\mathbf{K}_e$ and internal force vector $\mathbf{f}^{int}$ can be derived as:

$$\begin{aligned} \mathbf{K}_e &= \int_{\Omega_e} \bar{\mathbf{B}}^T \cdot \mathbf{C}^{ep} \cdot \bar{\mathbf{B}} \, d\Omega + \mathbf{K}_{GEOM}, \\ \mathbf{f}^{int} &= \int_{\Omega_e} \bar{\mathbf{B}}^T \cdot \boldsymbol{\sigma} \, d\Omega, \end{aligned} \tag{6}$$

where the additional term $\mathbf{K}_{GEOM}$ in the expression of the stiffness matrix originates from the non-linear part of the strain field and is commonly called geometric stiffness matrix [7], while $\mathbf{C}^{ep}$ is the elastic–plastic

tangent modulus associated with the material behaviour law [19].

In addition to the basic formulation of the SHB elements described above, some special treatments are required for the linear SHB8PS and SHB6 elements in order to improve their performance. In particular, a physical stabilization matrix, computed in a co-rotational coordinate frame [7], is used in the formulation of the SHB8PS element in order to control the zero-energy modes, which are inherent in the reduced-integration technique. Furthermore, an appropriate projection of the strains is required to eliminate some locking phenomena, in particular for the linear SHB6 and SHB8PS elements [7] and [15].

1.3 Explicit/Dynamic Framework

The dynamic version of the SHB elements is essentially based on the quasi-static formulation described above; therefore, it will not be repeated here. However, the mass matrix is required in dynamic problems in order to calculate the inertial term in the variational principle. Note that the stiffness matrix $\mathbf{K}_e$ (see Eq. (6)) is not required in such dynamic analysis, except for problems dealing with natural frequency extraction, for which both the stiffness and mass matrix are computed. Several computational methods exist in the literature for the calculation of the element mass matrix [20]. Among them, the lumped mass matrix approach is usually adopted in most dynamic problems, which results in a diagonal mass matrix. In the formulation of the current solid-shell elements, the lumped mass matrix method is followed, due to its computational advantages. Accordingly, the element mass matrix $\mathbf{M}^e$ (with a size of $3n\times3n$) can be expressed in terms of the following block of components:

$$\mathrm{M}_{IJ} = \begin{cases} m\int_{\Omega_e} \rho N_I N_J d\Omega & I = J \\ 0 & I \neq J \end{cases}, \tag{7}$$

where $m = \int_{\Omega_e} \rho d\Omega \Big/ \sum_{I=J=1}^{n} \int_{\Omega_e} \rho N_I N_J d\Omega$. N_I and N_J are the element interpolation functions and ρ is the mass density.

2 FINITE ELEMENT SIMULATIONS AND DISCUSSIONS

In this section, several benchmark tests, including both linear and non-linear problems, are selected to evaluate the performance of the SHB solid-shell elements. The first two linear tests are investigated to examine the convergence rate of the SHB elements. Then, the SHB elements are tested in vibration analysis in order to predict the first four eigenfrequencies of a rectangular cantilever plate and a fully clamped square plate. Finally, three non-linear benchmark problems involving quasi-static and dynamic analyses are carried out to assess the performance of the SHB elements in the framework of large displacements and rotations as well as large strains.

In the following simulations, the geometries are meshed using the nomenclature $N_1\times N_2\times N_3$ for the linear and quadratic hexahedral elements (SHB8PS and SHB20), and $N_1\times N_2\times 2\times N_3$ for the linear and quadratic prismatic elements (SHB6 and SHB15), where N_1 denotes the number of elements in the length direction, N_2 the number of elements in the width direction, and N_3 the number of elements in the thickness direction. The latter is equal to 1 in all simulations, which represents a single element layer through the thickness.

2.1 Linear Static Beam Problems

2.1.1 Elastic Cantilever Beam Subjected to Bending Forces

The first linear static test is an elastic cantilever beam with four concentrated loads at its free end. The geometric parameters and material properties are given in Fig. 2. This simple test aims to analyse the behaviour of the SHB elements in the case of bending-dominated conditions. The analytical solution for the deflection at the load point is $U_{ref} = 7.326\times10^{-3}$ m. The convergence results are given in Tables 1 and 2 in terms of normalized deflection with respect to the analytical solution. These simulation results prove that all of the SHB elements provide an excellent convergence rate, but with a slower convergence rate for the linear prismatic element SHB6. For the latter, the triangular geometry and the associated interpolation functions lead to constant strain fields inside the element, which requires finer meshes to obtain accurate solutions [15].

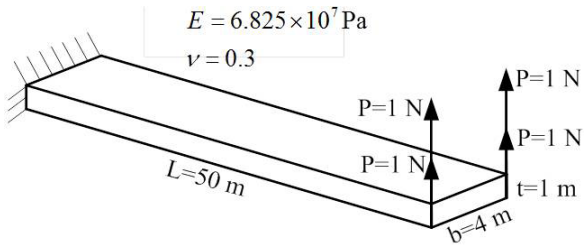

Fig. 2. *Elastic cantilever beam subjected to bending forces*

Table 1. *Normalized deflection results obtained with the linear SHB elements*

Mesh	SHB8PS	Mesh	SHB6
	U/U_{ref}		U/U_{ref}
5×1×1	0.9750	12×2×2×1	0.7062
10×1×1	0.9898	24×2×2×1	0.9019
12×4×1	0.9898	48×2×2×1	0.9669
24×4×1	0.9933	100×4×2×1	0.9807

Table 2. *Normalized deflection results obtained with the quadratic SHB elements*

Mesh	SHB20	Mesh	SHB15
	U/U_{ref}		U/U_{ref}
2×1×1	0.9672	12×2×2×1	0.9896
5×1×1	0.9865	24×2×2×1	0.9925
10×1×1	0.9929		

2.1.2 Elastic Cantilever Beam Subjected to Torsion-Type Forces

The second linear static test is illustrated in Fig. 3 and consists of a cantilever beam subjected to a torsion-type loading. The end of the beam is loaded by two opposite concentrated forces causing a twisting-type loading along the beam. The geometric and material parameters are given in Fig. 3. In the same way, the deflection results at one load point, normalized with respect to the reference solution $U_{ref} = 3.537\times10^{-4}$ m, are reported in Tables 3 and 4.

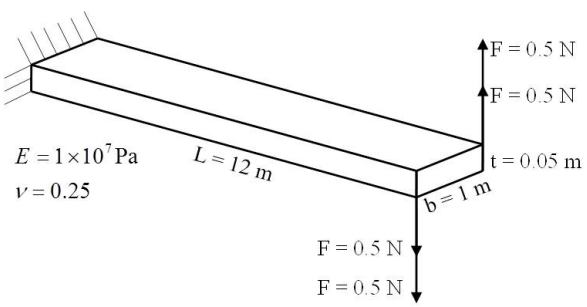

Fig. 3. *Elastic cantilever beam subjected to torsion-type loading*

Table 3. *Normalized deflection results obtained with the hexahedral SHB elements*

Mesh	SHB8PS	SHB20
	U/U_{ref}	U/U_{ref}
10×5×1	1.0470	1.0278
20×5×1	1.0479	1.0280
50×5×1	1.0500	
50×10×1	1.0289	

Table 4. *Normalized deflection results obtained with the prismatic SHB elements*

Mesh	SHB6	SHB15
	U/U_{ref}	U/U_{ref}
10×5×2×1	0.0107	0.9783
20×5×2×1	0.0247	1.0111
50×5×2×1	0.0916	
50×10×2×1	0.3438	
100×20×2×1	1.0873	

Similar to the previous test problem, the simulation results again show that all of the SHB elements provide a good convergence rate, without noticeable locking phenomena, except for the linear prismatic element SHB6 that requires finer meshes for convergence.

2.2 Plate Vibration Problems

2.2.1 Simple Rectangular Cantilever Plate

The first plate vibration problem is a rectangular cantilever plate with constant thickness. As illustrated in Fig. 4, the rectangular plate, with length L, width b=L/2, and thickness t, is fully clamped on one side, while the other sides are entirely free. The predicted results, in terms of non-dimensional frequency coefficient $\omega\sqrt{D/\rho tL^4}$, associated with the first four natural frequencies ω are summarized in Table 5, where $D = Et^3/\left(12\left(1-\nu^2\right)\right)$ is the flexural rigidity of the plate; E and ν are the Young modulus and Poisson ratio, respectively. All predicted results using the SHB8PS, SHB20, and SHB15 elements are in good agreement with the theoretical results as well as with the reference solutions given in **[21]** and **[22]**. For the linear prismatic SHB6 element, due to its relatively poor performance, finer meshes are required to obtain relatively accurate solutions.

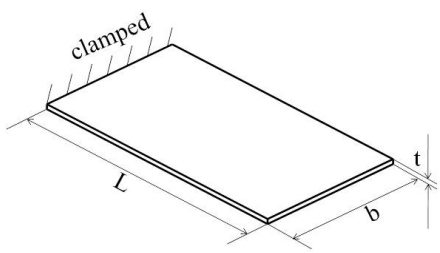

Fig. 4. *Simple rectangular cantilever plate*

2.2.2 Fully Clamped Square Plate

The second plate vibration problem relates to a fully clamped square plate, as illustrated in Fig. 5. The

Table 5. *Natural frequency coefficients for the rectangular cantilever plate*

Mode	Theoretical results*	Experimental results*	Simulated results**	SHB8PS	SHB20	SHB6	SHB15
				20×10×1	10×5×1	400×200×2×1	10×5×2×1
1	3.47	3.42	3.44	3.44	3.44	4.022	3.44
2	14.93	14.52	14.77	14.66	14.46	20.51	14.56
3	21.26	20.86	21.50	21.42	21.22	28.03	21.43
4	48.71	46.9	48.19	47.69	46.95	59.97	47.63

Note: results marked by * are taken from [21], while results marked by ** are available in [22].

Table 6. *Natural frequency coefficients for the clamped square plate*

Mode	Reference solution*	Simulated results**	SHB8PS	SHB20	SHB6	SHB15
			16×16×1	16×16×1	400×400×2×1	16×16×2×1
1	5.999	6.024	6.004	6.012	6.659	6.027
2,3	8.567	8.671	8.599	8.605	9.079	8.632
4	10.4	10.52	10.387	10.545	11.337	10.533
5,6	11.5	11.78	11.590	11.523	12.257	11.614

Note: results marked by * are taken from [23], while results marked by ** are taken from [24].

length to thickness ratio of this square plate is fixed equal to 1000 and the Poisson ratio of the material is 0.3. For comparison with reference solutions from the literature, the non-dimensional frequency coefficient λ is calculated for the first six natural frequencies of the plate, which is defined as $\lambda^2 = \omega L^2 \sqrt{\rho t / D}$, where D is the flexural rigidity defined in the previous test problem. All predicted frequency coefficients obtained using SHB elements are summarized in Table 6 and compared with reference solutions taken from **[23]** and **[24]**. Similar to the previous vibration problem, the obtained results show the performance and efficiency of the SHB elements in determining the natural frequencies of plates, except for the linear prismatic SHB6 element, for which finer meshes are inherently required to obtain accurate results.

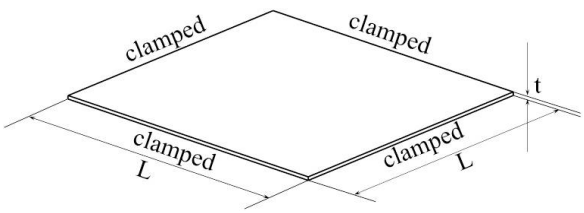

Fig. 5. *Clamped square plate*

2.3 Non-Linear Static Problems

2.3.1 Fully Clamped Circular Plate

A fully clamped elastic circular plate subjected to a uniform pressure is considered here, which involves geometric nonlinearities. The geometric dimensions and material elastic properties are taken from **[25]** and summarized in Fig. 6. Due to the symmetry of the problem, only one quarter of the plate is modelled, which is meshed using 105 SHB8PS elements, 3200 SHB6 elements, 39 SHB20 elements, and 78 SHB15 elements, successively. Fig. 7 shows the numerical results, in terms of the non-dimensional ratio of the central deflection W_0 to the thickness t, obtained with the SHB elements together with the reference solution from **[25]** and the analytical solution given by Chia **[26]**. As revealed by Fig. 7, all SHB solid–shell elements provide an accurate solution for this type of bending problem as compared to the reference and analytical solutions.

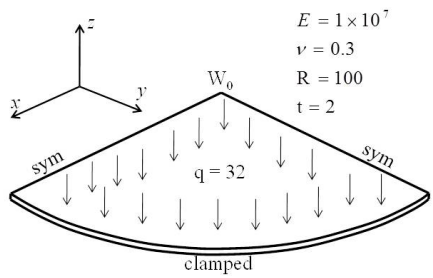

Fig. 6. *Clamped circular plate*

2.3.2 Pinched Semi-Cylindrical Shell

The pinched semi-cylindrical shell, as shown in Fig. 8, is a popular benchmark test that has been considered in several references **[27]**; both isotropic and laminated shells have been studied. This semi-cylindrical shell is subjected to a vertical radial force at the middle

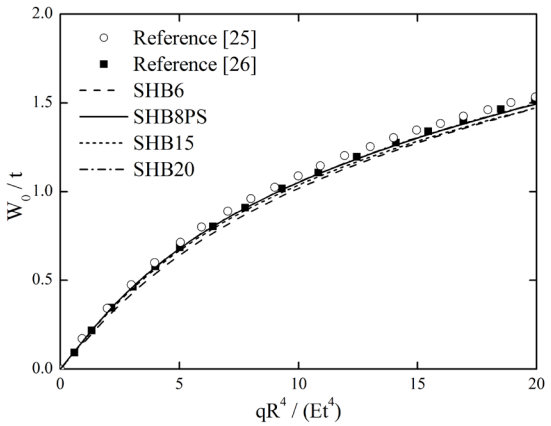

Fig. 7. *Normalized central deflection results for the clamped circular plate*

of the free circumferential edge, while the other circumferential edge is fully clamped (see Fig. 8 for the geometric and material parameters as well as the remaining boundary conditions). Due to the symmetry of the problem, only one half of the structure is modelled. Fig. 9 displays the load-deflection curves at the load point A, which are obtained using the SHB elements along with the reference solution available in **[27]**. The simulation results show good agreement with the reference solution given in **[27]**, which was obtained using (40×40) shell elements. Note, however, that these good convergence results are obtained here with less computational effort, since the SHB elements most often require coarser meshes, except for the linear prismatic SHB6 element, where a finer mesh is required to obtain an accurate solution.

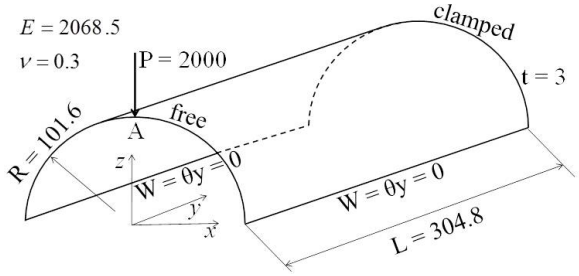

Fig. 8. *Pinched semi-cylindrical shell*

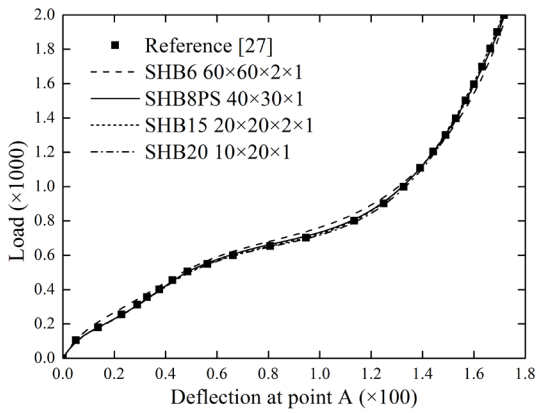

Fig. 9. *Load–deflection curves for the pinched semi-cylindrical shell*

2.4 Explicit Dynamic Problems

2.4.1 Elastic Cantilever Beam Bending

In order to evaluate the dynamic non-linear response of the SHB elements, we consider here an elastic cantilever beam that is loaded impulsively with a concentrated force applied at its free end. The geometric parameters and material properties are summarized in Fig. 10. The deflection history at Point A (indicated at the free edge in Fig. 10), which is obtained with the SHB elements, is plotted in Fig. 11, where it is compared with the reference results given in **[8]**. From this figure, one can observe that for all of the SHB elements, both the maximum deflection and time period are in good agreement with those provided by the reference solution.

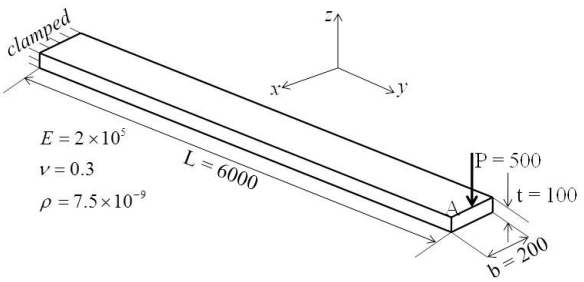

Fig. 10. *Elastic cantilever beam under impulsively-applied loading*

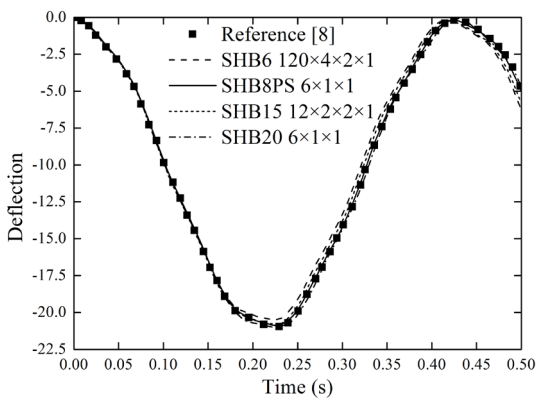

Fig. 11. *Deflection history for the elastic cantilever beam under dynamic loading*

2.4.2 Simply Supported Elastic Beam

The second non-linear dynamic problem is an elastic beam, which is simply supported at both ends. The beam is subjected to a uniform load, resulting in a maximum deflection of the order of its depth. The geometric dimensions, material properties, and boundary conditions are all summarized in Fig. 12. Owing to the symmetry of the problem, only half of the beam is discretized. The deflection of the central point, obtained with the SHB solid-shell elements, is depicted in Fig. 13 and compared with the reference solution taken from [28]. It can be seen that the numerical results obtained with the proposed SHB elements are in good agreement with the reference solution.

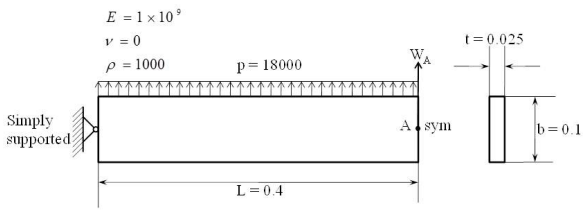

Fig. 12. *Simply supported elastic beam*

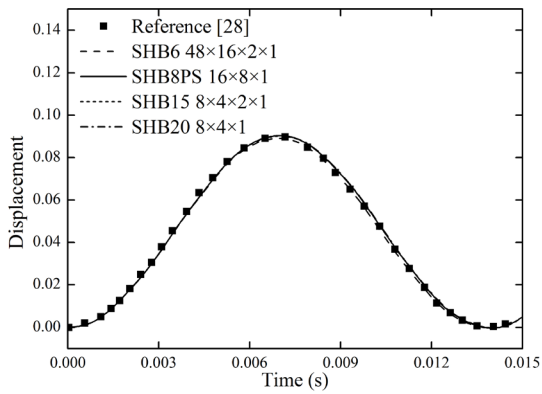

Fig. 13. *Deflection results for the simply supported elastic beam*

2.5 Application to the Simulation of Deep Drawing Process

In this section, a popular sheet metal forming process, involving geometric and material nonlinearities as well as double-sided contact, is simulated to further evaluate the performance of the proposed SHB elements. This selective benchmark consists in the simulation of the deep drawing process of a cylindrical cup, which is commonly used to study the earing profile of the cup when the anisotropic behaviour of sheet metals is considered. The initially circular metal sheet, with a diameter of 158.76 mm and a thickness of 1.6 mm, is made of an AA2090-T3 aluminium alloy [29]. For the modeling of the elastoplastic material behaviour, isotropic hardening described by the Swift law is considered. Its expression is given by

$$\sigma_y = k(\varepsilon_0 + \varepsilon_{eq}^p)^n, \tag{8}$$

where σ_y is the yield stress, ε_{eq}^p is the equivalent plastic strain, and (k, ε_0, n) are the hardening parameters. The Hill'48 quadratic yield criterion is adopted in this work to characterize the anisotropic plasticity of the sheet metal. All of the material parameters are summarized in Tables 7 and 8 [29]. The schematic view and dimensions of the drawing setup are given in Fig. 14.

Table 7. *Elastic–plastic parameters for the AA2090-T3 aluminium sheet*

E [MPa]	ν	k [MPa]	ε_0	n
70500	0.34	646	0.025	0.227

Table 8. *r-values for the AA2090-T3 aluminium sheet*

r_0	r_{45}	r_{90}
0.2115	1.7695	0.6923

Owing to the symmetry of the problem, only one quarter of the circular blank is discretized. The holding force is kept constant during the deep drawing and equal to 22.2 kN (for the complete model). The standard Coulomb law is used to model the contact between the circular sheet and the rigid tools, with a friction coefficient of 0.1 [29]. This process is simulated using the ABAQUS explicit/dynamic and implicit/quasi-static solvers for comparison purposes. The simulation results are compared with the experimental ones taken from [29]. It is worth noting that, for all of the SHB elements, the simulations are performed using only a single element layer in the thickness with five integration points. Fig. 15 shows the deformed meshes of the blank, as obtained with the four SHB elements, which correspond to a completely drawn cup. It can be seen that all SHB elements predict four ears for the cylindrical cup, which is consistent with the use of the quadratic Hill'48 yield surface for the description of the material planar anisotropy. Fig. 16 shows the final height profiles for the cup as obtained with the SHB elements for the quarter model. On the whole, one can observe that the shape of the predicted earing profiles is in good agreement with the experimental results for both quasi-static and dynamic versions of the SHB elements. More specifically, the SHB element predictions are closer to the experiment cup heights in the range around the experimental

peak value at 50° from the rolling direction, while the predicted cup heights are underestimated at 0° and 90° from the rolling direction. These predictions could be improved in the future by using more appropriate anisotropic yield criteria [29], which can predict more than four earing profiles for the complete circular blank, as observed experimentally for aluminium alloys [30] and [31].

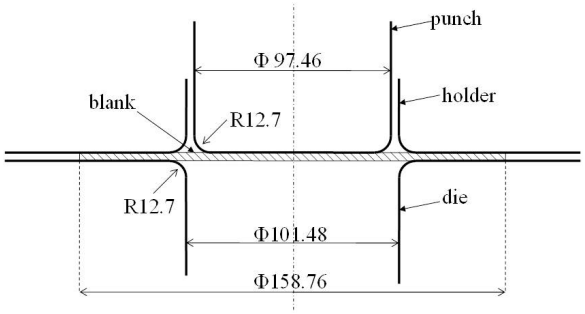

Fig. 14. *Schematic view of the drawing setup* [29]

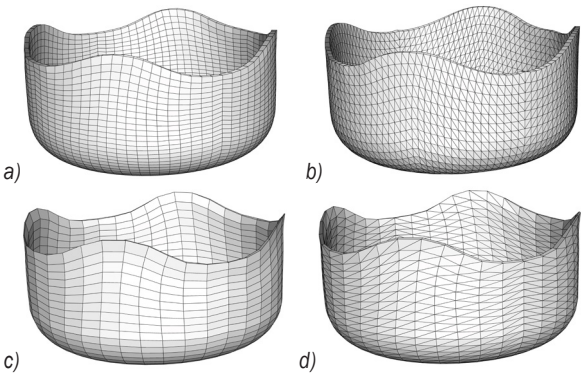

Fig. 15. *Final deformed shape for a completely drawn cylindrical cup using a) the SHB8PS elements; b) the SHB6 elements; c) the SHB20 elements; and d) the SHB15 elements*

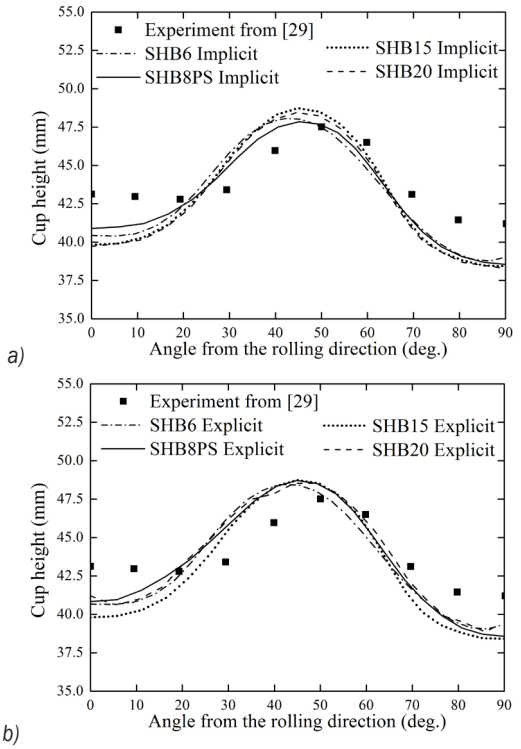

Fig. 16. *Predicted cup height profiles obtained by a) implicit/static and b) explicit/dynamic analysis, along with experimental measurements*

3 CONCLUSIONS

The assumed-strain solid–shell finite element technology SHB has been extended to explicit dynamic analysis and coupled with advanced anisotropic plasticity models for the modeling of thin three-dimensional structures under quasi-static or dynamic loading conditions and sheet metal forming processes. This family of SHB solid–shell elements consists of a linear 6-node prismatic element and a linear 8-node hexahedral element as well as their quadratic counterparts (15-node prismatic element and 20-node hexahedral element, respectively). All of these linear and quadratic solid–shell elements have been implemented into ABAQUS implicit/static and explicit/dynamic software packages to model various quasi-static and dynamic problems. The respective capabilities of the proposed SHB elements were first evaluated through a series of linear and non-linear benchmark tests, both in static and dynamic analyses. The obtained results, using only a single element layer with two integration points, showed excellent performance in terms of convergence rate and accuracy when compared to reference solutions yielded by existing state-of-the-art solid and shell finite elements from the literature. Then, the performance of the SHB elements has been assessed via the simulation of the deep drawing process of a cylindrical cup made of an aluminium alloy with anisotropic plastic behaviour. For comparison purposes, both implicit/quasi-static and explicit/dynamic versions of the SHB elements have been used for these deep drawing simulations. The earing profiles predicted by the implicit/quasi-static and explicit/dynamic versions were found to be reasonably close to each other, and in satisfactory agreement with the experiments on the whole. Nevertheless, the prediction of the earing profiles could be improved by adopting advanced non-quadratic anisotropic yield functions that are more suitable to aluminium alloys.

4 REFERENCES

[1] Abed-Meraim, F., Combescure, A. (2002). SHB8PS–a new adaptive, assumed-strain continuum mechanics shell element for impact analysis. *Computers & Structures*, vol. 80, no. 9-10, p. 791-803, **DOI:10.1016/S0045-7949(02)00047-0**.

[2] Parente, M.P.L., Fontes Valente, R.A., Natal Jorge, R.M., Cardoso, R.P.R., Alves de Sousa, R.J. (2006). Sheet metal forming simulation using EAS solid-shell finite elements. *Finite Elements in Analysis and Design*, vol. 42, no. 13, p. 1137-1149, **DOI:10.1016/j.finel.2006.04.005**.

[3] Reese, S. (2007). A large deformation solid-shell concept based on reduced integration with hourglass stabilization. *International Journal for Numerical Methods in Engineering*, vol. 69, no. 8, p. 1671-1716, **DOI: 10.1002/nme.1827**.

[4] Schwarze, M., Reese, S. (2009). A reduced integration solid-shell finite element based on the EAS and the ANS concept—Geometrically linear problems. *International Journal for Numerical Methods in Engineering*, vol. 80, no. 10, p. 1322-1355, **DOI:10.1002/nme.2653**.

[5] Caseiro, J.F., Valente, R.A.F., Reali, A., Kiendl, J., Auricchio, F., Alves de Sousa, R.J. (2015). Assumed natural strain NURBS-based solid-shell element for the analysis of large deformation elasto-plastic thin-shell structures. *Computer Methods in Applied Mechanics and Engineering*, vol. 284, p. 861-880, **DOI:10.1016/j.cma.2014.10.037**.

[6] Flores, F.G. (2016). A simple reduced integration hexahedral solid-shell element for large strains. *Computer Methods in Applied Mechanics and Engineering*, vol. 303, p. 260-287, **DOI:10.1016/j.cma.2016.01.013**.

[7] Abed-Meraim, F., Combescure, A. (2009). An improved assumed strain solid–shell element formulation with physical stabilization for geometric non-linear applications and elastic–plastic stability analysis. *International Journal for Numerical Methods in Engineering*, vol. 80, no. 13, p. 1640-1686, **DOI:10.1002/nme.2676.**

[8] Pagani, M., Reese, S., Perego, U. (2014). Computationally efficient explicit nonlinear analyses using reduced integration-based solid-shell finite elements. *Computer Methods in Applied Mechanics and Engineering*, vol. 268, p. 141-159, **DOI:10.1016/j.cma.2013.09.005**.

[9] Sena, J.I.V., Alves de Sousa, R.J., Valente, R.A.F. (2011). On the use of EAS solid-shell formulations in the numerical simulation of incremental forming processes. *Engineering Computations*, vol. 28, no. 3, p. 287-313, **DOI:10.1108/02644401111118150**.

[10] Cardoso, R.P.R., Yoon, J.W., Mahardika, M., Choudhry, S., Alves de Sousa, R.J., Fontes Valente, R.A. (2008). Enhanced assumed strain (EAS) and assumed natural strain (ANS) methods for one-point quadrature solid-shell elements. *International Journal for Numerical Methods in Engineering*, vol. 75, p. 156-187, **DOI:10.1002/nme.2250**.

[11] Ben Bettaieb, A., Velosa de Sena, J.I., Alves de Sousa, R.J., Valente, R.A.F., Habraken, A.M., Duchene, L. (2015). On the comparison of two solid-shell formulations based on in-plane reduced and full integration schemes in linear and non-linear applications. *Finite Element in Analysis and Design*, vol. 107, p. 44-59, **DOI:10.1016/j.finel.2015.08.005**.

[12] Moreira, R.A.S., Alves de Sousa, R.J., Valente, R.A.F. (2010). A solid-shell layerwise finite element for non-linear geometric and material analysis. *Composite Structures*, vol. 92, p. 1517-1523, **DOI:10.1016/j.compstruct.2009.10.032**.

[13] Naceur, H., Shiri, S., Coutellier, D., Batoz, J.L. (2013). On the modeling and design of composite multilayered structures using solid-shell finite element model. *Finite Elements in Analysis and Design*, vols. 70-71, p. 1-14, **DOI:10.1016/j.finel.2013.02.004**.

[14] Kpeky, F., Boudaoud, H., Abed-Meraim, F., Daya, E.M. (2015). Modeling of viscoelastic sandwich beams using solid–shell finite elements. *Composite Structures*, vol. 133, p. 105-116, **DOI:10.1016/j.compstruct.2015.07.055**.

[15] Trinh, V.D., Abed-Meraim, F., Combescure, A. (2011). A new assumed strain solid–shell formulation "SHB6" for the six-node prismatic finite element. *Journal of Mechanical Science and Technology*, vol. 25, no. 9, p. 2345-2364, **DOI:10.1007/s12206-011-0710-7**.

[16] Abed-Meraim, F., Trinh V.D., Combescure, A. (2013). New quadratic solid–shell elements and their evaluation on linear benchmark problems. *Computing*, vol. 95, no. 5, p. 373-394, **DOI:10.1007/s00607-012-0265-1**.

[17] Wang, P., Chalal, H., Abed-Meraim, F. (2015). Efficient solid-shell finite elements for quasi-static and dynamic analyses and their application to sheet metal forming simulation. *Key Engineering Materials*, vols. 651-653, p. 344-349, DOI: **10.4028/www.scientific.net/KEM.651-653.344**.

[18] Simo, J.C., Hughes, T.J.R. (1986). On the variation foundations of assumed strain methods. *Journal of Applied Mechanics*, vol. 53, no. 1, p. 51-54, **DOI:10.1115/1.3171737**.

[19] Salahouelhadj, A., Abed-Meraim, F., Chalal, H., Balan, T. (2012). Application of the continuum shell finite element SHB8PS to sheet forming simulation using an extended large strain anisotropic elastic–plastic formulation. *Archive of Applied Mechanics*, vol. 82, no. 9, p. 1269-1290, **DOI:10.1007/s00419-012-0620-x**.

[20] Zienkiewicz, O.C., Taylor, R.L., Zhu, J.Z. (2006). *The Finite Element Method: Its Basis and Fundamentals, Sixth ed.*, Elsevier Ltd., Oxford, UK.

[21] Barton, M.V. (1951). Vibration of rectangular and skew cantilever plates. *Journal of Applied Mechanics*, vol. 18, p. 129-134.

[22] Anderson, R.G., Irons, B.M., Zienkiewicz, O.C. (1968). Vibration and stability of plates using finite elements. *International Journal of Solids and Structures*, vol. 4, no. 10, p. 1031-1055, **DOI:10.1016/0020-7683(68)90021-8**.

[23] Leissa, A.W. (1969). *Vibration of Plates.* Scientific and Technical Information Division, NASA, Washington, DC, USA.

[24] Sze, K.Y., Yao, L.Q. (2000). A hybrid stress ANS solid-shell element and its generalization for smart structure modelling. Part I: solid-shell element formulation. *International Journal for Numerical Methods in Engineering*, vol. 48, no. 4, p. 545-564, **DOI:10.1002/(SICI)1097-0207(20000610)48:4<545::AID-ME889>3.0.CO;2-6.**

[25] Cai, Y.C., Atluri, S.N. (2012). Large rotation analyses of plate/shell structures based on the primal variational principle and a fully nonlinear theory in the updated lagrangian co-rotational reference frame. *Computer Modeling in Engineering*

& Sciences, vol. 83, no. 3, p. 249-273, **DOI:10.3970/cmes.2012.083.249**.

[26] Chia, C.Y. (1980). Nonlinear analysis of plate, McGraw-Hill, New York, USA.

[27] Sze, K.Y., Liu, X.H., Lo, S.H. (2004). Popular benchmark problems for geometric nonlinear analysis of shells. *Finite Elements in Analysis and Design*, vol. 40, no. 11, p. 1551-1569, **DOI:10.1016/j.finel.2003.11.001**.

[28] Flanagan, D.P., Belytschko, T. (1981). A uniform strain hexahedron and quadrilateral with orthogonal hourglass control. *International Journal for Numerical Methods in Engineering*, vol. 17, no. 5, p. 679-706, **DOI:10.1002/nme.1620170504**.

[29] Yoon, J.W., Barlat, F., Dick, R.E., Karabin, M.E. (2006). Prediction of six or eight ears in a drawn cup based on a new anisotropic yield function. *International Journal of Plasticity,* vol. 22, no. 1, p. 174-193, **DOI:10.1016/j.ijplas.2005.03.013.**

[30] Banabic, D., Barlat, F., Cazacu, O., Kuwabara, T. (2010). Advances in anisotropy and formability. *International Journal of Material Forming*, vol. 3, p. 165-189, **DOI:10.1007/s12289-010-0992-9**.

[31] Wang, J., Sun, J. (2012). Plane strain transversely anisotropic analysis in sheet metal forming simulation using 6-component Barlat yield function. *International Journal of Mechanics and Materials in Design*, vol. 8, p. 327-333, **DOI:10.1007/s10999-012-9198-2**.

Strojniški vestnik - Journal of Mechanical Engineering 63(2017)1, 35-44
DOI:10.5545/sv-jme.2016.3639
Original Scientific Paper
Received for review: 2016-04-04
Received revised form: 2016-09-12
Accepted for publication: 2016-11-29

Robust Fault-Tolerant Control of In-Wheel Driven Bus with Cornering Energy Minimization

András Mihály[1] – Péter Gáspár[1,2] – Balázs Németh[1,2]

[1]Budapest University of Technology and Economics, Department of Control for Transportation and Vehicle Systems, Hungary
[2]Hungarian Academy of Sciences, Institute for Computer Science and Control, Hungary

The aim of this paper is to design fault-tolerant and energy optimal trajectory tracking control for a four-wheel independently actuated (FWIA) electric bus with a steer-by-wire steering system. During normal driving conditions, the architecture of the proposed controller enables the bus to select an energy optimal split between steering intervention and torque vectoring, realized by the independently actuated in-wheel motors by minimizing the cornering resistance of the bus. In the case of skidding or a fault event of an in-wheel motor or the steering system, a high-level control reconfiguration using linear parameter varying (LPV) techniques is applied to reallocate control signals in order to stabilize the bus. The main novelty of the paper is the control reconfiguration method based on the specific characteristics of the in-wheel bus which enables introducing such scheduling variables, with which the safety and efficiency of the FWIA bus can be enhanced.

Keywords: In-wheel motor, FWIA bus, reconfigurable control, cornering resistance

Highlights

- *Reconfigurable velocity and trajectory tracking in-wheel electric vehicle control.*
- *High-level LPV design and low-level control allocation using constrained optimization.*
- *Development of a reconfiguration technique with scheduling variables.*
- *Consideration of actuator failure and energy optimal cornering.*

0 INTRODUCTION

As economical and environment-friendly hybrid/electric vehicles become increasingly popular, researchers and automotive companies also focus on the development of in-wheel electric vehicles, which have several benefits in comparison to conventional vehicles. From a vehicle dynamic point of view, the fast and precise torque generation of the hub motors lends torque vectoring capability to the vehicle with which manoeuvrability can be enhanced significantly [1] and [2]. The electric in-wheel motors must also be integrated with friction brakes, as proposed in [3]. By knowing the characteristics of the in-wheel engines and the hydraulic brake system, energy optimal torque distribution can be achieved as proposed by [4] and [5]. Moreover, high-efficiency regenerative braking can be implemented [6].

The capabilities of a four-wheel independently actuated (FWIA) vehicle enable novel techniques to improve safety and economy. Recently, a sliding mode control has been developed by [7] to deal with a faulty in-wheel motor by rearranging steering geometry depending on the location of the fault. Furthermore, the steer-by-wire steering system failures can be handled more effectively in an FWIA vehicle by using differential drive-assisted steering, as presented in [8]. The performance degradation of both the steering system and the in-wheel motors were addressed in a more general manner in [9]. The aim of the paper [10] was to design a trajectory and velocity tracking reconfiguration control method for FWIA vehicle, in which both types of actuator failures and cornering resistance minimization are handled simultaneously in order to enhance the economic performance of the vehicle.

The novelty of the proposed method in this paper lies in the high-level linear parameter varying (LPV) control reconfiguration strategy based on the specific design of weighting functions' handling actuator selection. The method enables the vehicle to dynamically modify the prescribed control values best suited for the actual vehicle state and the corresponding priority regarding safety and economy.

The paper is organized as follows: Section 1 introduces the vehicle model used for the control of the FWIA bus. Section 2 presents the control design found on an LPV framework and the structure of the fault tolerant and energy efficient control reconfiguration. Section 3 defines the allocation of the high-level control signals based on vehicle dynamics. Section 4 demonstrates the effect of the introduced method in a software-in-the-loop (SIL) simulation environment. Finally, some concluding statements are listed in Section 5.

*Corr. Author's Address: Budapest University of Technology and Economics Department of Control for Transportation and Vehicle Systems, H-1111 2. Stoczek street, Budapest, Hungary, mihaly.andras@mail.bme.hu

1 CONTROL-ORIENTED MODEL OF THE BUS

The goal of the design is to ensure trajectory and velocity tracking for the FWIA bus, taking longitudinal and lateral dynamics into account while neglecting the vertical behaviour of the bus. Thus, for the modelling of the FWIA bus dynamics, the well-known two-wheeled bicycle model is used, see Fig. 1.

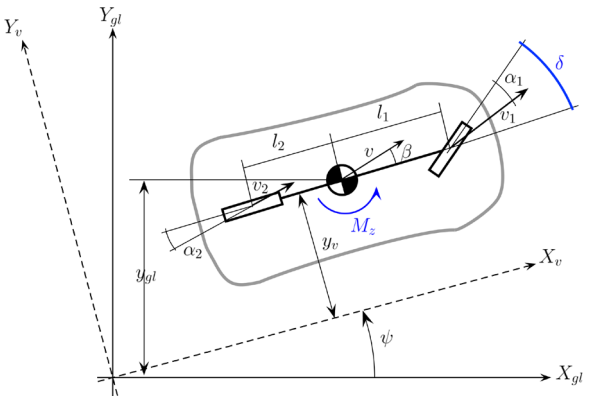

Fig. 1. *Single track bicycle model*

The motion equations in the planar plane can be written as follows:

$$\begin{aligned} J\ddot{\psi} &= l_1 F_{yf} - l_2 F_{yr} + M_z, \\ m\ddot{\xi}(\dot{\psi} + \dot{\beta}) &= F_{yf} + F_{yr}, \\ m\ddot{\xi} &= F_l - F_d, \end{aligned} \tag{1}$$

where m is the bus mass, J is the yaw inertia, $F_{yf} = c_1\alpha_1$ and $F_{yr} = c_2\alpha_2$ are the lateral tyre forces on the front and rear axle, c_1 and c_2 are the tyres' cornering stiffness. The distances measured from the centre of gravity to the front and rear axles are denoted by l_1 and l_2. The side slip angles of the front and rear wheels are $\alpha_1 = \delta - \beta - \dot{\psi} l_1 / \dot{\xi}$ and $\alpha_2 = -\beta + \dot{\psi} l_2 / \dot{\xi}$. The yaw rate of the bus is denoted with $\dot{\psi}$, the bus side-slip angle is β and ξ is the longitudinal displacement of the FWIA bus.

The high-level control inputs of the bus are the longitudinal force noted with F_l, the yaw moment M_z generated by torque vectoring, and the steering angle δ of the front wheels. The disturbance force F_d contains the drag, rolling and road slope disturbances: $F_d = F_{d1} + F_{d2} + F_{d3}$. Here, the aerodynamic drag is a function of the drag coefficient c_w, the air density ρ_{aero}, the frontal area size A_F and the velocity of the bus: $F_{d1} = 0.5 c_w \rho_{aero} A_F \dot{\xi}^2$. The rolling resistance force depends on vehicle mass m, rolling resistance coefficient f and road slope angle θ: $F_{d2} = mgf\cos\theta$, where g is the gravitational constant. Finally, the road slope disturbance is calculated as: $F_{d3} = mg\sin\theta$.

Since the nonlinearity of the system described by the differential equations of Eq. (1) is caused by the velocity $\dot{\xi}$ of the bus, choosing it as a scheduling variable $\rho_1 = \dot{\xi}$ the nonlinear model is rewritten as an LPV model. Note that another scheduling variable ρ_2 is also introduced responsible for the high-level control allocation between steering and yaw moment generation. The main goal of the proposed method presented in the paper is to determine the value of ρ_2 in such way that the energy efficiency and safety of the FWIA bus can be guaranteed. Thus, a real-time calculation is carried out to define $\rho_2^{M_z}$ and ρ_2^{δ} related to safety and ρ_2^{e} related to energy efficiency, while simple decision logic sets the value of ρ_2 considering priorities.

The state-space representation of the LPV model can be written as follows:

$$\dot{\bar{x}} = A(\rho_1)\bar{x} + B_1\bar{w} + B_2\bar{u}, \tag{2}$$

where the state vector $\bar{x} = \begin{bmatrix} \dot{\xi} & \xi & \dot{\psi} & \beta \end{bmatrix}^T$ contains the bus velocity, the displacement, the yaw rate and the side-slip angle. Note that the input vector $\bar{u} = \begin{bmatrix} F_l & \delta & M_z \end{bmatrix}^T$ contains the high-level control inputs, the output vector $\bar{y} = \begin{bmatrix} \dot{\xi} & \dot{\psi} \end{bmatrix}^T$ contains the measured velocity and the yaw rate, while the disturbance vector is $\bar{w} = \begin{bmatrix} F_d \end{bmatrix}^T$.

2 DESIGN OF ENERGY OPTIMAL AND FAULT TOLERANT CONTROLLER

For the nonlinear model of the FWIA bus, a gain scheduling LPV controller is necessary to guarantee a global solution. The reference signals for the bus to follow are the reference velocity and the yaw rate. The former is set by the driver, while the latter is also given by the driver steering intervention δ_d as follows [11]: $\dot{\psi}_{ref} = \dot{\xi} / d \cdot e^{-t/\tau} \cdot \delta_d$, where τ is the time constant, d is a parameter depending on the bus geometry and velocity. With $\dot{\xi}_{ref}$ denoting the reference velocity set by the driver, the two signals are put in a reference vector $\bar{R} = [\dot{\xi}_{ref} \; \dot{\psi}_{ref}]^T$. Thus, the control task is to follow the signals given in vector $\bar{R}$, for which two optimization criteria must be satisfied at the same time. Both the velocity error $z_{\dot{\xi}} = |\dot{\xi}_{ref} - \dot{\xi}|$ and yaw rate error $z_{\dot{\psi}} = |\dot{\psi}_{ref} - \dot{\psi}|$ must be minimized with the consideration of the optimization criterion $z_{\dot{\xi}} \to 0$ and $z_{\dot{\psi}} \to 0$. These are represented with the performance vector $\bar{z}_1 = \begin{bmatrix} z_{\dot{\xi}} & z_{\dot{\psi}} \end{bmatrix}^T$, while the limitation of the control inputs connected to the physical set-up of the in-wheel

motors and steering system are defined by a second performance vector $\bar{z}_2 = \begin{bmatrix} F_l & \delta & M_z \end{bmatrix}^T$.

2.1 High-Level Controller Design

The proposed high-level controller is based on the closed-loop *P*-*K*-Δ architecture, as depicted in Fig. 2. Here, *P* is the augmented plant in which uncertainties given by Δ are taken into consideration and *K* is the controller.

The design is based on selecting relevant weighting functions representing control objectives, disturbances, and sensor noises. Weighting functions W_p ensure the accommodation of performances defined in $\bar{z}_1$, serving as penalty functions. Disturbances and sensor noises are considered with W_w and W_n, while the neglected dynamics of the bus are represented by W_u.

The focus of the paper is connected to the weighting function W_a, responsible for the control reconfiguration between actuators. The goal of the design is to ensure an optimal split between steering and torque vectoring for the bus, considering both the efficiency and safety of the FWIA bus. These criteria are realized by the scheduling parameter $\rho_2 \in [0.01, 1]$, which holds for the scaling of the actuators. Thus, the weighting function of the steering $W_{a\delta} = (\delta_{max}\chi_1)/(\rho_2)$ and the differential torque generation $W_{aMz} = (\rho_2)/(M_{zmax}\chi_2)$ are dependent on ρ_2, with δ_{max} and M_{zmax} representing the maximal steering angle and yaw moment, χ_1 and χ_2 are design parameters tuned to achieve an appropriate control reallocation.

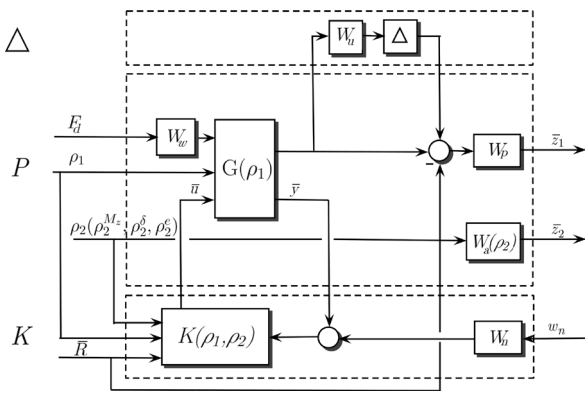

Fig. 2. *Closed-loop structure*

The consideration of safety and efficiency described later in Section 2.2 and Section 2.3 are implemented by the defining the value of ρ_2 based on the calculated parameters $\rho_2^{M_z}$, ρ_2^{δ} and ρ_2^{e}. The minimization task for the LPV performance problem already described in [12] is written as follows:

$$\inf_{K} \sup_{\rho \in F_P, \|w\|_2 \neq 0, w \in L_2} \sup \frac{\|z\|_2}{\|w\|_2} \leq \gamma. \tag{3}$$

The goal of the design is to select a parameter-varying controller in order to guarantee quadratic stability, while the induced L_2 norm from the disturbance $\bar{w}$ to the performances $\bar{z}$ remains smaller than γ. The *LPV* control synthesis is detailed in [13].

2.2 Consideration of Fault Events and Wheel Slip

The reconfiguration method in the case of a faulty in-wheel electric motor or the skidding of one of the wheel is based on the specific property of the in-wheel motor construction. The fast and accurate torque generation of the electric motors and the direct link to the wheels enables a precise estimation of the transmitted longitudinal wheel forces for each wheel of the FWIA bus. For this purpose, the wheel dynamics must be considered, given as follows:

$$J_{ij}\dot{\omega}_{ij} = T_{ij}^{motor} - R_{eff}F_{ij}^{trans}, \tag{4}$$

where J_{ij}, $i \in [f = front, r = rear]$, $j \in [L = left, R = right]$ is the wheel inertia, $\dot{\omega}_{ij}$ is the measured angular acceleration, R_{eff} is the effective rolling radius of the wheels, T_{ij}^{motor} is the torque produced by the in-wheel engines, which can be measured. Thus, assuming no wheel slip the transmitted longitudinal drive or brake force F_{ij}^{trans} can be calculated. When longitudinal wheel slip λ occurs, the friction force F_{ij}^{trans} can still be estimated as described in [14] by considering the relation of the friction coefficient and wheel slip $\mu - \lambda$ given by the Pacejka Magic Formula, see [15].

Thus, by using the estimated transmitted torque of each wheel $T_{ij}^{trans} = R_{eff}F_{ij}^{trans}$ and assuming a small steering angle δ of the front wheels the transmitted yaw moment of the in-wheel bus can be given as follows:

$$M_z^{trans} = \frac{T_f^{trans}}{R_{eff}}\frac{b_f}{2} + \frac{T_r^{trans}}{R_{eff}}\frac{b_r}{2}, \tag{5}$$

where $T_f^{trans} = -T_{fL}^{trans} + T_{fR}^{trans}$ and $T_r^{trans} = -T_{rL}^{trans} + T_{rR}^{trans}$ are the transmitted torque at the front and rear concerning M_z^{trans}, moreover, b_f and b_r are the front and rear track.

Hence, the relation of the desired yaw moment given by the high-level controller M_z and the achieved

yaw moment M_z^{trans} of the FWIA bus serves as the indicator for the bus dynamic state related to the trajectory-tracking task. For example, when the transmitted yaw moment M_z^{trans} becomes significantly smaller than the prescribed value M_z, the bus is skidding, or an internal failure has occurred in one of the electric motors. Thus, the cornering manoeuvre can only be evaluated by using more steering and less yaw moment; therefore, the negative effect of a wheel slip or motor failure can be eliminated. Hence, one of the aims of the reconfiguration presented in the paper is to reallocate the high-level control signals in such cases, by introducing the variable $\rho_2^{M_z}$ as follows:

$$\rho_2^{M_z} = \left| \frac{\left| M_z - M_z^{trans} \right|}{M_z} \right|. \tag{6}$$

Accordingly, if the bus can transmit the prescribed yaw moment during a cornering manoeuvre, the value of $\rho_2^{M_z}$ remains small and the value of ρ_2 responsible for the high-level control allocation is that set by the result of the energy optimization method detailed later in Section 2.3 or the value of ρ_2^{δ} due to a steering system failure. In the case of a faulty electric motor or wheel slip due to critical bus dynamics, the value of $\rho_2^{M_z}$ increases and the energy optimal split between steering and yaw moment generation is overwritten by the safety critical distribution with altering the value of ρ_2 to be equal with $\rho_2^{M_z}$. Thus, with modification of the weighting function W_a of the LPV controller, steering intervention becomes more pronounced to overcome the effect of lateral dynamic performance degradation due to faulty electric motor or wheel spin.

Fault-tolerant control methods for steer-by-wire steering systems have already been presented by researchers. Although faulty steering occurs rarely in comparison to the performance degradation or wheel slip related to the in-wheel motors, this present paper also deals with such event to guarantee bus stability. Here, the aim of the fault tolerant design is to substitute the effect of the steering in case of a fault event by reconfiguring the high-level controller, with which additional differential torque is generated by the in-wheel motors. The fault of the steering is assumed to be detected by FDI, as proposed by **[16]**.

When the fault is detected, the scheduling variable $\rho_2^{\delta} = 0$ is applied overwriting the value of the actual ρ_2. Thus, weighting function W_a of the LPV controller is modified in such a way, that the high-level controller prescribes solely yaw moment signal for the FWIA bus. Thus, in the case of a steering system failure, the cornering manoeuvres are evaluated using only the precise torque vectoring ability of the in-wheel bus.

2.3 Consideration of Cornering Resistance

The efficiency of the FWIA bus can be enhanced by optimizing the high-level control inputs of the bus, i.e. the steering angle δ and yaw moment M_z. The aim of this procedure is to minimize cornering forces, i.e. the longitudinal disturbances affecting the bus related to the cornering manoeuvre. Using the two-wheeled bicycle model, the cornering force F_c is calculated, omitting forces related to the drag, road slope and rolling resistance of the wheels as follows:

$$F_c = 2F_{yf}\sin(\alpha_1 + \delta) + 2F_{yr}\sin(\alpha_2). \tag{7}$$

Thus, during a cornering manoeuvre the power loss of the bus related to the cornering is $P = F_c\dot{\xi} + M_z\dot{\psi}$. Assuming no energy recuperation, the cornering energy of the FWIA bus can simply be calculated. Using small angle approximation $\sin(\alpha_1) \approx \alpha_1$ and $\sin(\alpha_2) \approx \alpha_2$, the following formula can be derived: $P = (2c_1\alpha_1(\alpha_1 + \delta) + 2c_2(\alpha_2)^2)\dot{\xi} + M_z\dot{\psi}$. Ignoring α_1^2 and α_2^2 given their small values, the power loss related to cornering can finally be expressed as follows, see **[17]**:

$$P = (2c_1\alpha_1\delta)\dot{\xi} + M_z\dot{\psi}. \tag{8}$$

Note that in the calculation of the power loss $\alpha_1 = \delta - \beta - \dot{\psi}l_1/\dot{\xi}$ need to be known. This requires the knowledge of the bus side slip angle β, which can be estimated with different methods, as proposed by **[18]**.

The role of the control allocation in the power loss due to cornering is well represented, as the power loss is a function of several bus dynamic states and the values of the control inputs δ and M_z. Thus, the objective of the cornering resistance minimization task is to create an optimal steering angle δ^e and yaw-moment M_z^e, with which the power loss expressed in Eq. (8) can be minimized. Note, that the total yaw moment induced by the steering intervention and differential torque generation must be unchanged. Thus, using the torque Eq. (1) and assuming the steady state of the bus dynamic parameters (β, $\dot{\psi}$ and $\dot{\xi}$), the following constraint can be defined:

$$(c_1l_1\delta^e + M_z^e) - (c_1l_1\delta + M_z) = 0. \tag{9}$$

Since the steer-by-wire steering system has constructional limitations $\delta_{min} \le \delta^e \le \delta_{max}$, it is also considered in the optimization process. The lower and

upper bounds of the optimal yaw moment is also considered with the following equation:

$$-mg\mu(b_f + b_r)/2 \le M_z^e \le mg\mu(b_f + b_r)/2 . \quad (10)$$

Another important constraint to achieving a reasonable solution for the minimization procedure is to guarantee that the signs of the steering angle and yaw moment are equal, i.e. $sign(\delta^e) = sign(M_z^e)$. Next, the minimization of the total power loss represented by Eq. (8) is evaluated with the constraint given by Eq. (9) and with the constraints on the lower and upper bounds and sign relations regarding the optimal steering angle δ^e and yaw moment M_z^e. The solution of the convex optimization is the optimal steering angle δ^e and yaw moment M_z^e, with which the bus can minimize the power loss due to the cornering resistance. Hence, another variable representing energy efficiency ρ_2^e is introduced founded on the actual value of the scheduling variable ρ_2 as follows:

$$\rho_2^e = \begin{cases} \rho_2 - \varepsilon, & if \quad |M_z|/|M_z^e| < 1 \\ \rho_2 + \varepsilon, & if \quad |M_z|/|M_z^e| \ge 1 \end{cases}, \quad (11)$$

where ε is a scaled value based on the ratio of M_z^e and M_e.

The value of ρ_2^e thus represents the energy optimal control allocation, by which the weighting function W_a is set in such way that the LPV controller prescribes a steering angle and yaw moment that minimizes the power loss $P = (2c_1\alpha_1\delta)\dot{\xi} + M_z\dot{\psi}$ related to the cornering manoeuvre. However, in safety critical situations due to the failure of an in-wheel electric motor, wheel slip, or steering system failure, the reconfiguration is based on the variables $\rho_2^{M_z}$ and ρ_2^{δ}. The strategy of the hierarchical control along with the scheduling variable selection will be presented in the following section.

3 IMPLEMENTATION OF THE CONTROL SYSTEM

The energy optimal and fault tolerant reconfigurable controller design of the in-wheel bus is implemented in a hierarchical structure. The multi-layer layout of the proposed control scheme is shown in Fig. 3.

In the first layer, the high-level LPV controller calculates the inputs of the FWIA bus based on the driver reference signals, the measured bus signals regarding the velocity and yaw rate and the value of scheduling variable ρ_2. Note that ρ_2 is derived from the energy optimal and fault-tolerant methods. For this purpose, a decision logic has been created with giving priority to the safety of the in-wheel bus. Hence, ρ_2 is defined as follows:

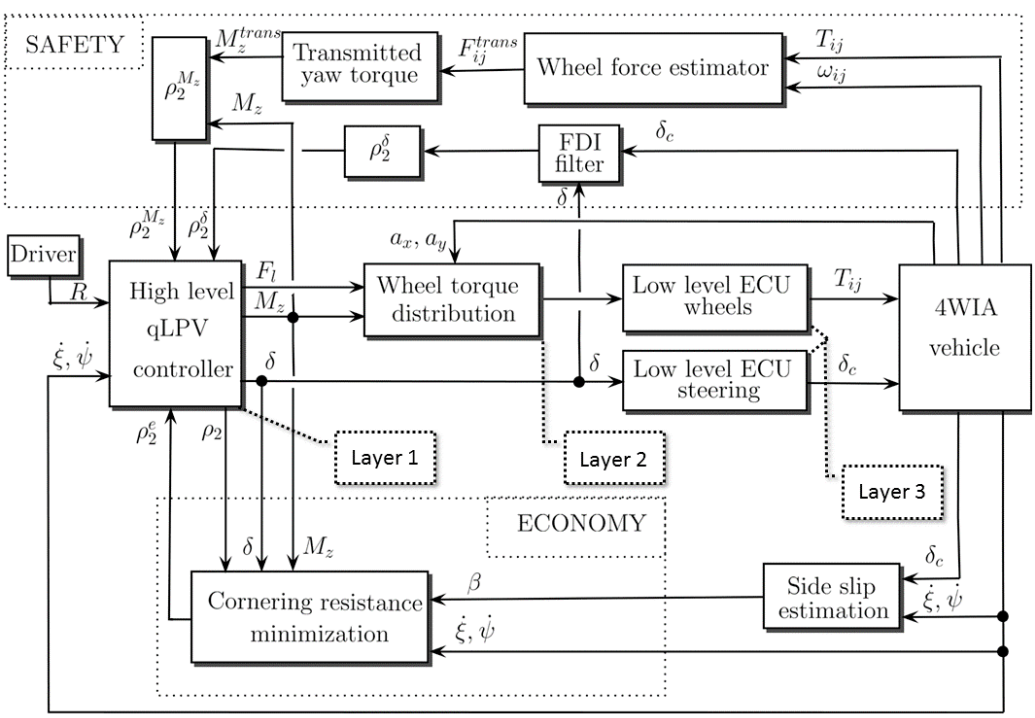

Fig. 3. *Hierarchical structure of the reconfigurable control system*

$$\rho_2 = \begin{cases} \rho_2^e, & if \quad \rho_2^e > \rho_2^{M_z} \quad and \quad \rho_2^\delta = 1 \\ \rho_2^{M_z}, & if \quad \rho_2^e \le \rho_2^{M_z} \quad and \quad \rho_2^\delta = 1. \\ \rho_2^\delta, & if \quad \rho_2^\delta = 0 \end{cases} \quad (12)$$

Note, that a first-order proportional filter and a hysteresis component are also utilized in order to smooth the value of ρ_2 and avoid chattering between controllers. The output of the first layer is the high-level control signals, i.e. the longitudinal force F_l, the yaw moment M_z and the steering angle δ.

The task of the second layer is to distribute the control signals of the LPV controller between the actuators of the in-wheel bus, i.e. the steering system and the in-wheel motors. Since the steering angle is straightforwardly applied, the main objective of the dynamic allocation process is to define the appropriate drive and brake torques for the in-wheel motors based on the high-level control signal M_z and F_l. The dynamic allocation method is implemented in order to define the necessary wheel forces F_{ij} generated by the in-wheel motors. The realized yaw moment of the bus can be written as:

$$\Delta M_z = (-F_{fL} + F_{fR}) \cdot \frac{b_f}{2} + (-F_{rL} + F_{rR}) \cdot \frac{b_r}{2}. \quad (13)$$

Here the optimization criterion is to minimize the difference between the desired yaw moment M_z and the generated yaw moment ΔM_z, i.e. function f_{opt} defined as follows:

$$f_{opt} = M_z - \Delta M_z. \quad (14)$$

In the allocation process, the bus roll and pitch dynamics are also considered in order to avoid the skidding of the wheels during critical bus manoeuvres. Given the longitudinal and lateral accelerations of the bus a_x and a_y can be measured by low-cost sensors like accelerometers, it is possible to calculate each wheel load given by **[19]** as follows:

$$F_{z,ij} = m\left(\frac{l_{[1;2]}g}{L} \pm \frac{ha_x}{L}\right) \cdot \left(0.5 \pm \frac{ha_y}{b_{[f;r]}g}\right), \quad (15)$$

where $L = l_1 + l_2$ is the wheelbase, h is the height of the mass centre. For the calculation of the front wheel loads ($i = f$) l_2 and b_f is used with a negative sign in the first bracket, while for the rear wheel loads ($i = r$) l_1 and b_r is used with a positive sign in the first bracket. Note that the left wheel loads ($j = L$) are given with a negative sign in the second bracket, while the right wheel loads ($j = R$) with a positive sign.

Thus, the minimal and maximal longitudinal forces for the wheels of the FWIA bus can be expressed as:

$$F_{ij}^{max} = \mu F_{z,ij}, \qquad F_{ij}^{min} = -\mu F_{z,ij}, \quad (16)$$

where μ is the road friction, which is possible to estimate as proposed by **[20]** and **[21]**. In order to perform velocity tracking of the FWIA bus, the sum of the wheel forces must be equal to the longitudinal force F_l given by the high-level controller. Therefore, the following constraint must also be fulfilled:

$$\sum F_{ij} - F_l = 0. \quad (17)$$

Hence, the control allocation leads to a constrained optimization problem, in which the objective function $f_{opt} = M_z - \Delta M_z$ introduced in Eq. (14) must be minimized with the constraint of lower and upper bounds given by Eq. (16) and the nonlinear constraint given by Eq. (17). The solution of the optimization is the wheel forces F_{ij}, which are transformed into the corresponding in-wheel motor torques $T_{ij} = F_{ij} \cdot R_{eff}$.

Finally, the third layer contains the specific low-level controllers of the steer-by-wire steering system and the four electric in-wheel motors of the bus, transforming the control signals into real physical parameters. Here, the steering is modelled as a first order system as discussed in **[22]**. Considering the much faster torque response of the in-wheel motors compared to the dynamic response of the wheels, it can be modelled as a second-order system (see **[23]**) given by the following transfer function: $T_{ij}^m(s) = \frac{T_{ij}(s)(1+\eta)}{1 + 2\zeta s + 2\zeta^2 s^2}$, where T_{ij} are the required torques, T_{ij}^m are the real output torques of the motors, while ζ and η are design parameters considering the response time and steady state error of the electric motors. These parameters depend on the complex structure of the in-wheel electric motor including the inner controller and can be identified by measurements.

4 SIMULATION RESULTS

Simulations with the in-wheel electric bus have been performed in a software-in-the-loop (SIL) environment shown in Fig. 4. The upper part represents the electric in-wheel driven bus using a TruckSim/Simulink simulation environment, while the lower part represents the control system with dSPACE MicroAutoBox II on which the proposed control algorithm is running and serving as a fast

function prototyping electronic control unit (ECU). Note, that the reference signals for the controller and the input signals for the bus are transferred via controller area network (CAN) communication. The aim of the SIL environment is to perform simulation tests for tuning the proposed controller on a platform that can be converted into a hardware-in-the-loop (HIL) system by attaching dSPACE MicroAutoBox II to the CAN system of a real vehicle. By this means, prototype testing can be evaluated with the controller tuned in TruckSim/Simulink environment.

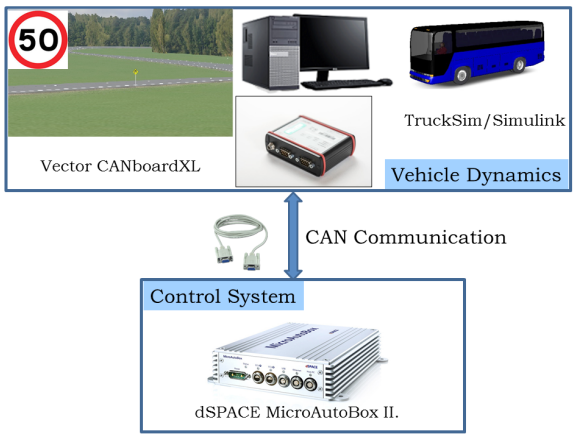

Fig. 4. *SIL environment*

The simulation vehicle selected in TruckSim is a two-axle bus equipped with four in-wheel motors and a steer-by-wire steering system. In the simulation, the in-wheel bus is assumed to be driven by a driver who must follow the trajectory of an S-turn shown in Fig. 5, while the bus velocity is set to a constant 50 km/h. The reference yaw rate for the bus to follow shown in Fig. 6 is generated by the driver operating the steering wheel. It is assumed, that the yaw rate, longitudinal and lateral accelerations of the FWIA bus can be measured with low-cost inertial sensors and accelerometers, as well as wheel speeds.

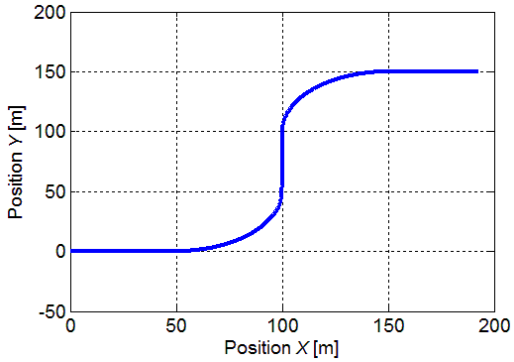

Fig. 5. Geometry of the S-turn

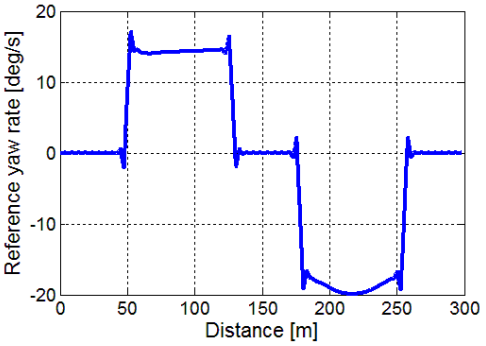

Fig. 6. *Reference yaw rate*

In the presented simulation case, the effect of an in-wheel motor fault is analysed by comparing the results of the simulation with one evaluated without any fault event.

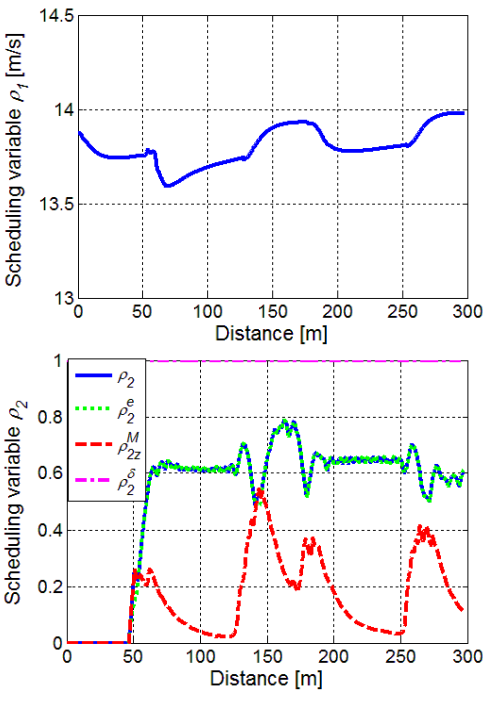

Fig. 7. *Scheduling variables without fault; a) ρ_1 and b) ρ_2*

The scheduling variables of the high-level controller without a fault event are shown in Fig. 7. It is well demonstrated, that the first scheduling variable ρ_1 shown in Fig. 7a corresponding to the bus velocity remains even in both corners while scheduling variable ρ_2 responsible for the high-level control allocation is equal to that given by the cornering resistance minimization method, as demonstrated in Fig. 7b.

In the case of a faulty in-wheel motor, scheduling variable ρ_1 becomes more uneven as shown in Fig. 8a.

The value of the scheduling variable ρ_2 changes significantly in the second corner, as shown in Fig. 8b. Since the designed yaw moment cannot be put on the road as a result of the faulty in-wheel motor, the value of $\rho_2^{M_z}$ increases and exceeds the value of ρ_2^{δ} given by the energy optimization method. Hence, the decision logic detailed selects the former as the scheduling variable ρ_2.

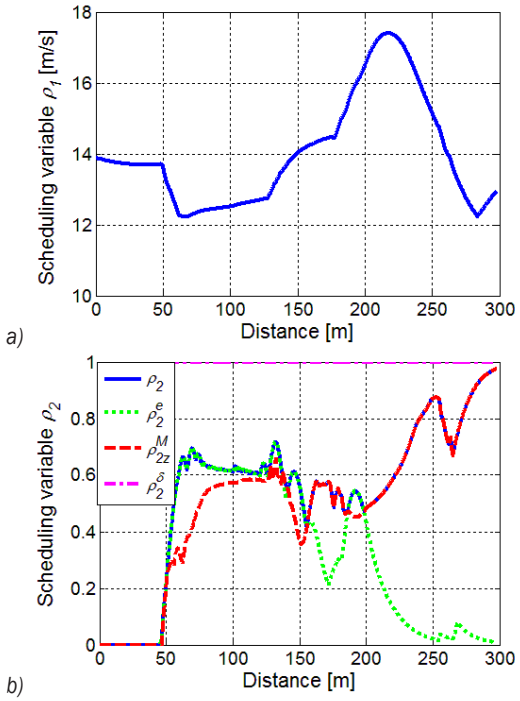

Fig. 8. *Scheduling variables with fault; a) ρ_1 and b) ρ_2*

The prescribed high-level control signals of the LPV controller for both cases are shown in Fig. 9. The operation of the high-level reconfiguration strategy is well demonstrated by observing Figs. 9b and c. Without a fault event, the value of ρ_2 corresponding to the energy optimal cornering yields an effective combination of steering and yaw moment generation. In the case of an in-wheel motor failure and the increased value of ρ_2, the LPV controller of the FWIA bus prescribes a bigger steering angle for the bus in comparison to the normal case without a fault event.

As a result of the dynamic wheel-torque allocation method, the in-wheel motors generate differential torque considering the bus pitch and roll motion, as shown in Fig. 10. It is well demonstrated by observing Fig. 10a that the left and right side motors, without a fault event generate approximately the same amount of differential torque in both corners.

Meanwhile, when the rear right in-wheel motor fails to produce any torque, as shown in Fig. 10b, the

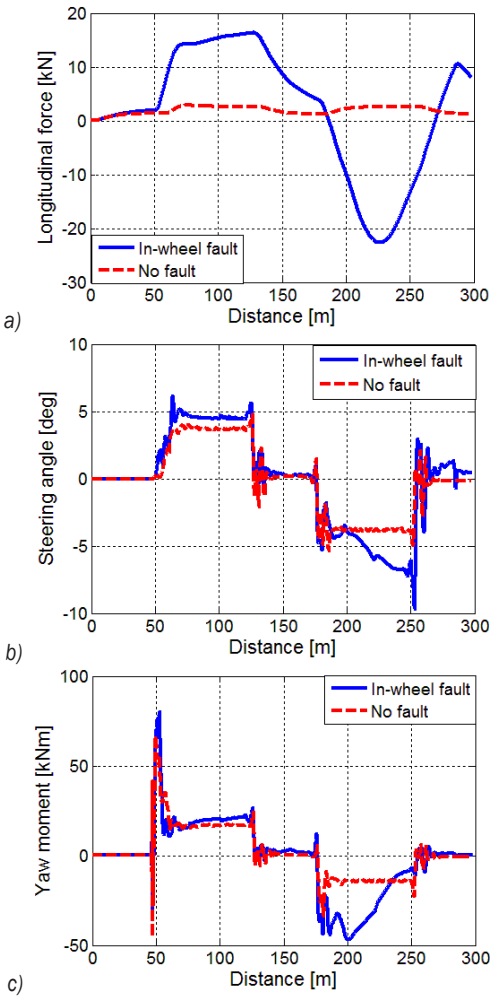

Fig. 9. *High-level control signals; a) longitudinal force, b) steering angle; c) yaw moment*

differential torque generation of the healthy in-wheel motors are also reduced due to the high-level control reallocation.

The performances of the proposed method are shown in Fig. 11. The velocity error of the FWIA bus does not exceed 1 km/h without a fault event as depicted in Fig. 11a. The yaw rate error shown in Fig. 11b also remains acceptably small even under a fault event due to the control reconfiguration. It is well demonstrated in Fig. 11c that the cornering energy increases significantly in the case of a fault event when the energy optimal high-level control allocation is overwritten.

5 CONCLUSIONS

This paper has proposed an energy optimal and fault tolerant LPV control method for the in-wheel electric

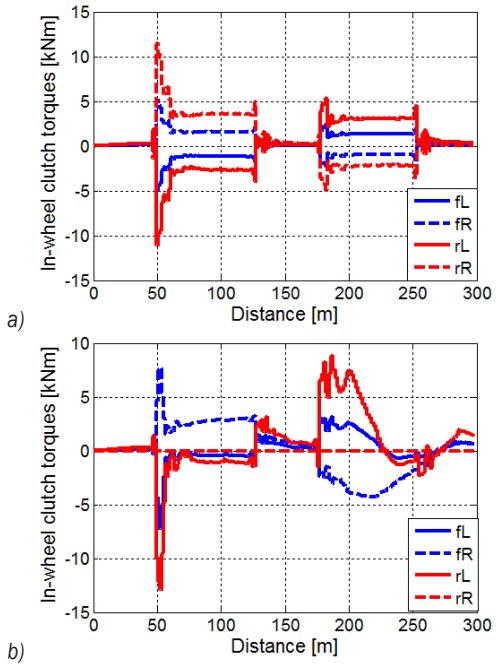

Fig. 10. *Hub motor torques; a) wheel torques without fault event, b) wheel torques with motor fault*

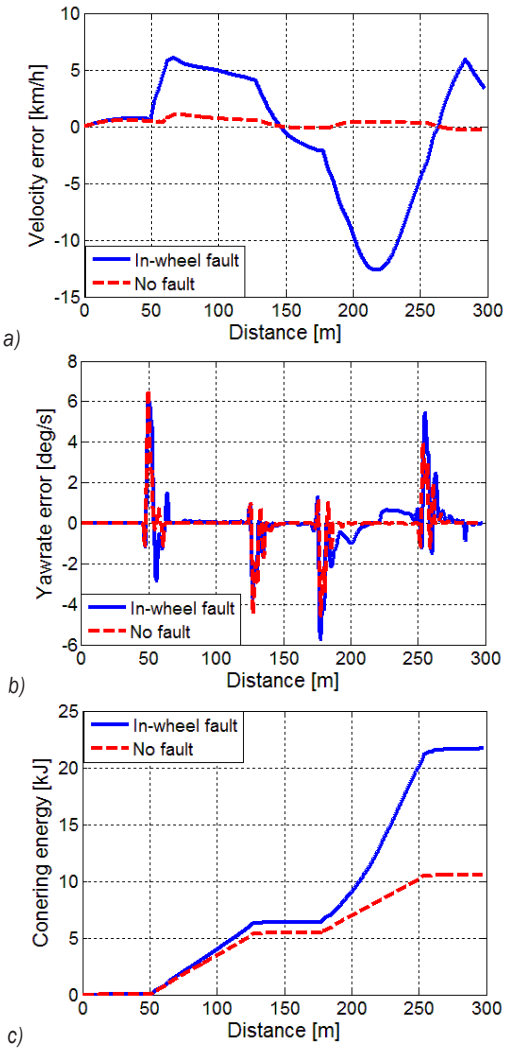

Fig. 11. *Performances of the scenarios; a) velocity error, b) yaw rate error, c) cornering energy*

bus. The proposed strategy is based on a high-level control reconfiguration method, in which the energy efficiency and safety of the FWIA bus are both considered. The operation of the proposed trajectory following control method has been tested in an SIL environment demonstrating the capability of the proposed method.

6 ACKNOWLEDGMENT

The research was supported by the National Research, Development and Innovation Fund through the project "SEPPAC: Safety and Economic Platform for Partially Automated Commercial vehicles" (VKSZ 14-1-2015-0125). This paper was partially supported by the János Bolyai Research Scholarship of the Hungarian Academy of Sciences.

7 REFERENCES

[1] Wu, F.-K., Yeh, T.-J., Huang, C.-F. (2013). Motor control and torque coordination of an electric vehicle actuated by two in-wheel motors. *Mechatronics*, vol. 23, no.1, p.46-60, **DOI:10.1016/j.mechatronics.2012.10.008**.

[2] Shuai, Z., Zhang, H., Wang, J., Li, J., Ouyang, M. (2013). Lateral motion control for four-wheel-independent-drive electric vehicles using optimal torque allocation and dynamic message priority scheduling. *Control Engineering Practice*, vol. 24, p. 55-66, **DOI:10.1016/j.conengprac.2013.11.012**.

[3] de Castro, R., Araújo, R.E., Tanelli, M., Savaresi, S.M., Freitas, D. (2012). Torque blending and wheel slip control in EVs with in-wheel motors. *Vehicle System Dynamics*, vol. 50, p. 71-94, **DOI:10.1080/00423114.2012.666357**.

[4] Lin, C., Xu, Z. (2015). Wheel torque distribution of four-wheel-drive electric vehicles based on multi-objective optimization. *Energies*, vol. 8, no. 5, p. 3815-3831, **DOI:10.3390/en8053815**.

[5] Wang, R., Chen, Y., Feng, D., Huang, X., Wang, J. (2011). Development and performance characterization of an electric ground vehicle with independently actuated in-wheel motors. *Journal of Power Sources*, vol. 196, p. 3962-3971, **DOI:10.1016/j.jpowsour.2010.11.160**.

[6] Ringdorfer, M., Horn, M. (2011). Development of a wheel slip actuator controller for electric vehicles using energy recuperation and hydraulic brake control. *IEEE International*

Conference on Control Applications, Denver, p. 313-318, **DOI:10.1109/CCA.2011.6044472**.

[7] Li, B., Du, H., Li, W. (2016). Fault-tolerant control of electric vehicles with in-wheel motors using actuator-grouping sliding mode controllers. *Mechanical Systems and Signal Processing*, vol. 72-73, p. 462-485, **DOI:10.1016/j.ymssp.2015.11.020**.

[8] Leng, B., Xiong, L., Jin, C., Liu, J. et al. (2015). Differential Drive Assisted Steering Control for an In-wheel Motor Electric Vehicle. *SAE International Journal of Passenger Cars-Electronic and Electrical Systems*, vol. 8, no. 2, p. 433-441, **DOI:10.4271/2015-01-1599**.

[9] Jing, H., Wang, R., Chadli, M., Hu C., Yan, F., Li, C. (2015). Fault-tolerant control of four-wheel independently actuated electric vehicles with active steering systems. *9th IFAC Symposium on Fault Detection, Supervision and Safety for Technical Processes*, vol. 48, no. 21, p. 1165-1172, **DOI:10.1016/j.ifacol.2015.09.684**.

[10] Gáspár, P., Bokor, J., Mihály, A., Szabó, Z. Fülep, T., Szauter F. (2015). Robust reconfigurable control for in-wheel electric vehicles. *9th IFAC Symposium on Fault Detection, Supervision and Safety for Technical Processes*, vol. 48, no. 21, p. 36-41, **DOI:10.1016/j.ifacol.2015.09.501**.

[11] Rajamani, R. (2005). *Vehicle Dynamics and Control.* Springer, New York, **DOI:10.1007/978-1-4614-1433-9**.

[12] Bokor, J., Balas, G. (2005). Linear parameter varying systems: A geometric theory and applications. *IFAC Proceedings Volumes*, vol. 38, no. 1, p. 12-22, **DOI:10.3182/20050703-6-cz-1902.00003**.

[13] Packard, A., Balas, G. (1997). Theory and application of linear parameter varying control techniques. *American Control Conference, Workshop I*, Albuquerque.

[14] Hu, J.-S., Yin, D. (2011). MTTE-based motion stabilization control for in-wheel motor electric vehicles. *Proceedings of SICE Annual Conference*, Tokyo, p. 312-317.

[15] Pacejka, H.B. (2004). *Tyre and Vehicle Dynamics.* Elsevier Butterworth-Heinemann, Oxford.

[16] Im, J.S., Ozaki, F., Yeu, T.K. , Kawaji, S. (2009). Model-based fault detection and isolation in steer-by-wire vehicle using sliding mode observer. *Journal of Mechanical Science and Technology*, vol. 23, no. 8, p. 1991-1999, **DOI:10.1007/s12206-009-0357-9**.

[17] Sumiya, H., Fujimoto, H. (2010). Range extension control system for electric vehicle with active front steering and driving/braking force distribution on curving road. *36th Annual Conference on IEEE Industrial Electronics Society*, p. 2352-2357, **DOI:10.1109/IECON.2010.5674927**.

[18] Ryu, J., Rossetter, E.J., Gerdes J.C. (2002). Vehicle sideslip and roll parameter estimation using GPS. *6th International Symposium on Advanced Vehicle Control*, Hiroshima.

[19] Kiencke, U., Nielsen, L. (2005). *Automotive Control Systems*. Springer Verlag, Berlin, Heidelberg, **DOI:10.1007/b137654**.

[20] Gustafsson, F. (1997). Slip-based tire-road friction estimation. *Automatica*, vol. 33, no. 6, p. 1087-1099, **DOI:10.1016/S0005-1098(97)00003-4**.

[21] Li, K., Misener, J. A., Hedrick, K. (2007). On board road condition monitoring system using slip-based tyre road friction estimation and wheel speed signal analysis. *Automatica*, vol. 221, p. 129-146, **DOI:10.1243/1464419jmbd60**.

[22] Takanori, F., Shogo, M., Kenji, M., Norihiko, A., Koichi, O. (2004). Active steering systems based on model reference adaptive nonlinear control. *Vehicle System Dynamics*, vol. 42, no. 5, p. 301-318, **DOI:10.1080/0042311042000266739**.

[23] Tahami, F., Kazemi, R., Farhanghi, S. (2003). A novel driver assist stability system for all-wheel-drive electric vehicles. *IEEE Transactions on Vehicular Technology*, vol. 52, no. 3, p. 683-692, **DOI:10.1109/TVT.2003.811087**.

Strojniški vestnik - Journal of Mechanical Engineering 63(2017)1, 45-55

DOI:10.5545/sv-jme.2016.3811 Original Scientific Paper
Received for review: 2016-06-16
Received revised form: 2016-10-20
Accepted for publication: 2016-11-03

Research of Planetary Gear Fault Diagnosis Based on Multi-Scale Fractal Box Dimension of CEEMD and ELM

Xihui Chen – Gang Cheng* – Hongyu Li – Yong Li
China University of Mining and Technology, School of Mechatronic Engineering, China

The planetary gear is the most critical part of a drive transmission system, and its faults will affect the reliability of the equipment, and even cause accidents. Therefore, it is of great significance to study the fault diagnosis of the planetary gear. A method of planetary gear fault diagnosis based on the multi-scale fractal box dimension of complementary ensemble empirical mode decomposition (CEEMD) and extreme learning machine (ELM) is proposed. The original vibration signal is decomposed by CEEMD, and a series of intrinsic mode functions (IMFs) are obtained. Some effective IMFs are extracted, and their reconstructed signal associated with the feature information is obtained. The reconstructed signal is analysed with multi-scale analysis, and the fault feature information contained in the signals with different scales is quantified and extracted via a fractal box dimension. The status recognition of planetary gear is achieved by combining ELM. The experiments show that the proposed method is effective at diagnosing planetary gear faults.

Keywords: Fault diagnosis, Planetary gear, CEEMD, Multi-scale, Fractal box dimension, ELM

Highlights

- *A method of planetary gear fault diagnosis based on the multi-scale fractal box dimensions of CEEMD and ELM is proposed.*
- *The effective IMFs which associate with the shock feature information are selected by the kurtosis criterion.*
- *The multi-scale fractal box dimension of the reconstructed signal is defined as the fault feature information.*
- *The status recognition of a planetary gear is achieved by combining ELM.*

0 INTRODUCTION

The planetary gear is widely used in all kinds of drive transmissions of large electromechanical equipment, and it is the most critical part of a drive transmission system. A fault in a planetary gear will affect the reliability of the equipment, and even causes accidents [1]. Therefore, to study planetary gear fault diagnosis has great significance. The complex structure of planetary gear and the changes of working parameters, such as speed and load, will cause the vibration signal of planetary gear to be non-stationary, and it also has the characteristics of frequency modulation (FM) and amplitude modulation (AM) [2]. Therefore, the traditional time-domain analysis and frequency-domain analysis that only have statistical properties and global significance are not suitable for processing the non-stationary signals; the feature extraction method for non-stationary signals and the advanced classification method should be studied.

In order to obtain the useful information generated by planetary gears, some time-frequency analysis methods are proposed. The time-frequency analysis method which has the best application effect is empirical mode decomposition (EMD) [3] proposed by Huang et al. [4]. A series of IMFs with strict definitions can be obtained from the original vibration signal [5]. However, EMD has a major drawback: modal aliasing. To solve this problem, EEMD is proposed [6]. The Gaussian white noise is added to the original signal to change the extreme points, and an IMF set can be obtained by EMD. The Gaussian white noise is added multiple times, and a series of IMF sets can be obtained. The final IMFs can be obtained by the average of a series of IMF sets, and the added Gaussian white noise is eliminated according to its uniform characteristics. However, due to the added Gaussian white noise is eliminated by ensemble average; the reconstructed signal of the IMFs still contains residual noise. CEEMD is the latest method to improve the shortcomings of EMD; it can achieve a better decomposition effect which is beneficial for extracting the features [7]. A pair of Gaussian white noises with opposite symbols are respectively added to the original vibration signal, following the EMD process is carried out. CEEMD can solve the problems of modal aliasing and energy leakage, and the problem of reconstruction error is alleviated by using complementary pairs of Gaussian white noise.

The collected vibration signal near the planetary gear also contains the vibration produced by other transmission components. With CEEMD, a large part of vibration interference produced by other transmission components and the feature information produced by planetary gears are divided into different IMFs. Only some IMFs associated with the feature information generated by planetary gear faults and some IMFs do not contain the information that we

*Corr. Author's Address: China University of Mining and Tech., School of Mechatronic Engineering, No 1, Daxue Rd. Xuzhou, Jiangsu, China, chenxh@cumt.edu.cn

need. The effective IMFs, including the most relevant, feature information for recognizing planetary gears should be selected. Next, it is necessary to extract the fault feature information. The multi-scale algorithm has the advantages of high efficiency, good convergence, and high precision, and it can show the features of the signals with different scales [8]. The fractal dimension is an important parameter in the quantitative description of nonlinear behaviour, and it mainly includes the Hausdorff dimension, similarity dimension and box dimension, etc. Among them, the fractal box dimension is widely used [9]. The fractal box dimension establishes the relationship with the nonlinear problem based on the box-filling idea. For the status change of a mechanical transmission system, it can be used to describe the statistical self-similarity feature of the fractal boundary of the vibration signal. Thus, the multi-scale fractal box dimension combining multi-scale analysis and fractal box dimension can be used to extract the fault feature information.

Fault classification is necessary after extracting the fault feature information; some classification methods such as support vector machine (SVM), ELM, and other neural networks are proposed [10]. SVM is a data classification method that is suitable for processing small samples, and the nonlinear mapping of the date is realized by the kernel function. Therefore, the kernel function and its parameters are crucial. With the development of optimization algorithms, some parameter optimization algorithms such as artificial colony bee algorithm and genetic algorithm are combined with SVM [11]. However, that will increase the complexity and computational burden. The neural network has developed into an effective classification method in fault diagnosis, but the traditional algorithms have several shortcomings, such as slow training speed, the fact that they easily fall into a local minimum point and sensitive learning rate. ELM is a new learning algorithm of the single-hidden layer feed-forward neural network, its weights between the input layer and hidden layer and the threshold of hidden neurons are randomly generated, and there is no need to adjust them in the training process. Only the number of hidden neurons needs to be set, and the unique optimal solution can be obtained [12]. ELM has the advantages of easy parameter selection, fast learning speed, and good generalization performance, and it can be applied in the classification of planetary gear status.

This paper is structured as follows. In Section 1, a mathematical model of planetary gear fault diagnosis based on a multi-scale fractal box dimension of CEEMD and ELM is built. In Section 2, the experiment equipment of planetary gear fault simulation is introduced. In Section 3 and Section 4, the vibration signals are processed by the proposed method, and its effectiveness and applicability are verified. In the last section, many conclusions are obtained.

1 MODEL BUILDING

1.1 CEEMD

CEEMD is an improved algorithm based on EMD; a pair of Gaussian white noises with opposite symbols are added to the original signal, and EMD and the ensemble average process are conducted. That can eliminate the residual noise contained in the reconstructed signal and improve the completeness of the decomposition process [13]. CEEMD can be expressed as follows:

Step 1: The original vibration signal is $x(t)$, and s pairs of Gaussian white noises with opposite symbols are added, and a $2s$ added white noise signal can be obtained.

$$\begin{bmatrix} x_{s+}(t) \\ x_{s-}(t) \end{bmatrix} = \begin{bmatrix} 1 & 1 \\ 1 & -1 \end{bmatrix} \begin{bmatrix} x(t) \\ n_s(t) \end{bmatrix}, \tag{1}$$

where $n_s(t)$ is the s^{th} added Gaussian white noise. $x_{s+}(t)$ is the signal added to the s^{th} Gaussian white noise with a positive symbol, and $x_{s-}(t)$ is the signal added to the s^{th} Gaussian white noise with a negative symbol.

Step 2: For the signal-added Gaussian white noise, EMD [4] is carried out, respectively. $2s$ sets of IMFs are obtained, and they are expressed as follows:

$$\begin{bmatrix} imf_{s+}^{i}(t) \\ imf_{s-}^{i}(t) \end{bmatrix} = E\left(\begin{bmatrix} 1 & 1 \\ 1 & -1 \end{bmatrix} \begin{bmatrix} x(t) \\ n_s(t) \end{bmatrix} \right), \quad s = 1,2,...,S; \quad i = 1,2,...,I, \tag{2}$$

where $E(\ )$ represent EMD process, S is the number of the added Gaussian white noise, and I is the number of the obtained IMFs.

Step 3: The process of ensemble average is processed, and the final IMFs can be obtained; they can be expressed as follows:

$$IMF_i = \frac{1}{2S} \sum_{s=1}^{S} (imf_{s+}^{i}(t) + imf_{s-}^{i}(t)). \tag{3}$$

Step 4: The vibration signal can be expressed as follows:

$$x(t) = \sum_{i=1}^{I} IMF_i(t) + r(t), \tag{4}$$

where $r(t)$ is the residual signal.

1.2 Extraction of Effective IMFs

The signal collected by the vibration sensor installed near the planetary gear also contains the vibration produced by other transmission components, which is reduced significantly in the vibration transfer process, and they have a certain difference with the vibration produced by the monitored planetary gear. With CEEMD, a large part of vibration interference produced by other transmission components and the feature information produced by planetary gear are divided into different IMFs. Only some IMFs associate with the feature information produced by planetary gear faults, and the effective IMFs associating with the fault feature information produced by the planetary gear should be selected. The shock components are generated during the meshing process of the planetary gear, and they have different changes when different faults of the planetary gear occur, so the fault feature information is usually contained in the shock components generated during the meshing process. Kurtosis is strongly related to the shock components, so the effective IMFs associated with feature information can be selected by kurtosis. Assuming $IMF_i=(x_1,x_2,...,x_N)$, The definition of kurtosis is as follows [14]:

$$K=\frac{\sum_{n=1}^{N}(|x_n|-\bar{x})^4}{\sigma^4}, \tag{5}$$

where $\bar{x}$ is the mean value and σ is the standard deviation of the signal.

1.3 Multi-Scale Fractal Box Dimension

The effective IMFs including the fault shock components are selected, and their reconstructed signal contains the main fault feature information generated by planetary gear fault. Next, the fault feature extraction and quantization of the reconstructed signal should be analysed.

1.3.1 Multi-Scale Analysis

Multi-scale analysis can show the features of the signals with different scales. For a time-domain signal with length H; $x_1,x_2,...,x_H$, it is divided into several time series with different lengths according to the scale factor τ. The average value of each divided data set is then calculated [15]. A new time series $\{y_j^{(\tau)}\}$ is constituted; it is expressed as Eq. (6) and Fig. 1.

$$\{y_j^{(\tau)}\}=\frac{1}{\tau}\sum_{h=(j-1)\tau+1}^{j\tau}x_h, \quad 1\le j\le\frac{H}{\tau}. \tag{6}$$

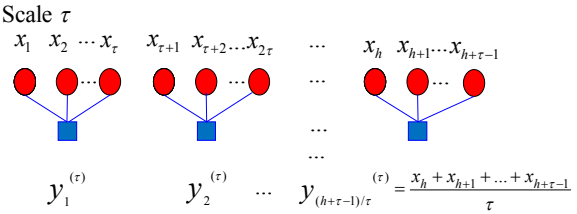

Fig. 1. *Multi-scale process*

1.3.2 Fractal Box Dimension

The fractal box dimension can be used to extract and quantify the feature information included in the signals with different scales. Assuming X is a not empty bounded subsets of R^n, and $N(X,\varepsilon)$ represents the minimum number of the subset that can cover X set with the maximum diameter ε. The definition of fractal box dimension is expressed as follows [16]:

$$\dim_B(X)=\lim_{\varepsilon\to0}\frac{\ln N(X,\varepsilon)}{\ln(1/\varepsilon)}. \tag{7}$$

Assuming the signal $Y=\{y_1,y_2,...,y_Q\}\subset O$, O is a closed set in the n-dimension Euclid space. Because the limitation of Eq. (7) cannot be calculated in accordance with the definition, the approximate method is used. ε is defined as a baseline, and it is gradually enlarged to $k\varepsilon$, $k\in Z^+$. The calculation equation is as follows:

$$P(k\varepsilon)=\sum_{i=1}^{Q/k}\left|\max(y_{k(i-1)+1},y_{k(i-1)+2},...,y_{k(i-1)+k+1})-\min(y_{k(i-1)+1},y_{k(i-1)+2},...,y_{k(i-1)+k+1})\right|, \tag{8}$$

where $i=1,2,...,Q/N$; N is the sampling data number, $k=1,2,...,M$; $M\le N$.

The grid count is as follows:

$$N_{k\varepsilon}=P(k\varepsilon)/(k\varepsilon)+1; \quad N_{k\varepsilon}>1. \tag{9}$$

A range that has a better linear relationship in the figure $\lg k\varepsilon-lgN_{k\varepsilon}$ is defined as a non-scaling range, and assuming the beginning and ending of this non-scaling range are k_1 and k_2, respectively.

$$\lg N_{k\varepsilon}=a\lg k\varepsilon+b; \quad k_1\le k\le k_2. \tag{10}$$

The slope of this line is determined by the least square method, and it is the fractal box dimension and expressed as follows:

$$d_B = \hat{a} = -\frac{(k_2 - k_1 + 1)(\sum \lg k \lg N_{k\varepsilon} - \sum \lg k \sum \lg N_{k\varepsilon})}{(k_2 - k_1 + 1)\sum \lg^2 k - (\sum \lg k)^2}. \quad (11)$$

1.3 Extreme Learning Machine

ELM has the advantages of easy parameter selection, fast learning speed and good generalization performance [17]. The structure of ELM is shown in Fig. 2. Where input layer has J neurons, hidden layer has H neurons, and output layer has K neurons [18].

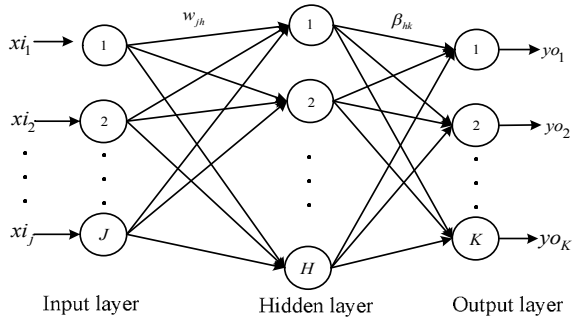

Fig. 2. *Structure of ELM*

The connection weights between the input layer and hidden layer and the connection weights between hidden layer and output layer are expressed as follows:

$$w = \begin{bmatrix} w_{11} & w_{12} & \cdots & w_{1h} \\ w_{21} & w_{22} & \cdots & w_{2h} \\ \vdots & \vdots & \ddots & \vdots \\ w_{j1} & w_{j2} & \cdots & w_{jh} \end{bmatrix},$$

$$\beta = \begin{bmatrix} \beta_{11} & \beta_{12} & \cdots & \beta_{1k} \\ \beta_{21} & \beta_{22} & \cdots & \beta_{2k} \\ \vdots & \vdots & \ddots & \vdots \\ \beta_{h1} & \beta_{h2} & \cdots & \beta_{hk} \end{bmatrix}, \quad (12)$$

where w_{jh} is the connection weight between the j^{th} neuron of the input layer and the h^{th} neuron of the hidden layer, and β_{hk} is the connection weight between the h^{th} neuron of the hidden layer and the k^{th} neuron of the output layer.

Setting the threshold ϕ of the hidden neurons is expressed as follows:

$$\phi = [\phi_1, \phi_2, \ldots, \phi_h]^T. \quad (14)$$

The input matrix xi and output matrix yo of the training set with Q samples are expressed as follows:

$$xi = \begin{bmatrix} xi_{11} & xi_{12} & \cdots & xi_{1Q} \\ xi_{21} & xi_{22} & \cdots & xi_{2Q} \\ \vdots & \vdots & \ddots & \vdots \\ xi_{j1} & xi_{j2} & \cdots & xi_{jQ} \end{bmatrix}_{J\times Q},$$

$$yo = \begin{bmatrix} yo_{11} & yo_{12} & \cdots & yo_{1Q} \\ yo_{21} & yo_{22} & \cdots & yo_{2Q} \\ \vdots & \vdots & \ddots & \vdots \\ yo_{k1} & yo_{k2} & \cdots & yo_{kQ} \end{bmatrix}_{K\times Q}. \quad (15)$$

The activation function of the hidden neuron is $g(x)$, then, the output T of ELM is expressed as follows:

$$T = [t_1, t_2, \ldots, t_Q]_{K\times Q},$$

$$t_h = [t_{1h}, t_{2h}, \ldots, t_{Kh}]^T_{1\times K} = \begin{bmatrix} \sum_{i=1}^{H} \beta_{i1} g(w_i xi_h + \phi_i) \\ \sum_{i=1}^{H} \beta_{i2} g(w_i xi_h + \phi_i) \\ \vdots \\ \sum_{i=1}^{H} \beta_{iK} g(w_i xi_h + \phi_i) \end{bmatrix}_{K\times 1},$$

$$(h = 1, 2, \ldots, Q), \quad (16)$$

where $w_i = [w_{i1}, w_{i2}, \ldots, w_{iJ}]^T$, $xi_h = [xi_{1h}, xi_{2h}, \ldots, xi_{Jh}]^T$.

The Eq. (16) can be expressed as follows:

$$H\beta = T^*, \quad (17)$$

where T^* is the transpose of T, and H is the output matrix of the hidden layer of ELM, and its concrete form is expressed as follows:

$$H(w_1, w_2, \ldots, w_H, \phi_1, \phi_2, \ldots, \phi_H, xi_1, xi_2, \ldots, xi_Q) = \begin{bmatrix} g(w_1 \bullet xi_1 + \phi_1) & g(w_2 \bullet xi_1 + \phi_2) & \cdots & g(w_h \bullet xi_1 + \phi_h) \\ g(w_1 \bullet xi_2 + \phi_1) & g(w_2 \bullet xi_2 + \phi_2) & \cdots & g(w_h \bullet xi_2 + \phi_h) \\ \vdots & \vdots & \ddots & \vdots \\ g(w_1 \bullet xi_Q + \phi_1) & g(w_2 \bullet xi_Q + \phi_2) & \cdots & g(w_h \bullet xi_Q + \phi_h) \end{bmatrix}. \quad (18)$$

When the activation function $g(x)$ is infinitely differentiable, the parameters of ELM do not need to be adjusted. w and ϕ can be randomly selected. The connection weight β between hidden layer and output layer can be obtained by calculating the least square solution of the following equations [19].

$$\min_{\beta} = \left\| H\beta - T^* \right\|. \quad (19)$$

The solution of Eq. (19) is as follows:

$$\hat{\beta} = H^+ T^*, \quad (20)$$

where H^+ is the Morre-Penrose generalized inverse matrix of the output matrix H.

2 EXPERIMENT INTRODUCTION

The planetary gear fault simulation bench is shown in Fig. 3. The planetary gearbox and fixed-axis gearbox are commonly used transmission components, and they have their respective advantages. Due to the need for some special occasions, the planetary gearbox and fixed-axis gearbox are often used in combination, such as the transmission system of shearer cutting part, the transmission system of the wind turbine and automotive gear reducer, etc. Thus, the fault simulation bench combining a planetary gearbox and fixed-axis gearbox is used. The acceleration sensors that used to measure the vibration signal generated by planetary gear are installed on the shell of the planetary gearbox. In this experiment, the sun gear faults are simulated; they are normal gear, broken gear, gear with tooth root crack and wear gear. Those gears are shown in Fig. 4. The parameter setting of the experiment process is shown in Table 1, and the vibration signals of four types of planetary gear statuses are sampled. The collected vibration signal is divided into a number of samples for analysis, and each sample includes 8400 data points. They are used to verify the effectiveness of the proposed fault diagnosis method of the planetary gear.

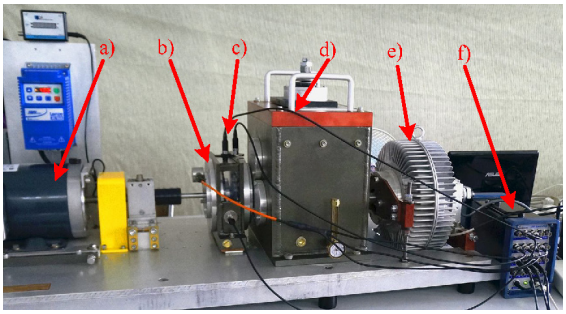

Fig. 3. *Fault experiment for planetary gear, a) three-phase asynchronous motor, b) planetary gearbox, c) acceleration sensors, d) fixed-axis gearbox, e) load system, f) acquisition system*

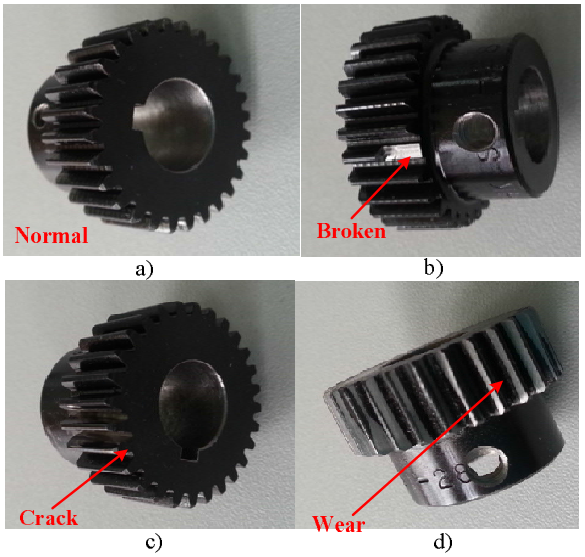

Fig. 4. *Four types of gears, a) normal gear, b) broken gear, c) gear with tooth root crack, d) wear gear*

Table 1. *Parameters setting of the experiment process*

Motor speed	Sampling frequency	Load
2400 r/min	4200 Hz	13.5 Nm

3 EXPERIMENT ANALYSIS

The analysis flowchart of the fault diagnosis method based on the multi-scale fractal box dimension of CEEMD and ELM is proposed and shown in Fig. 5.

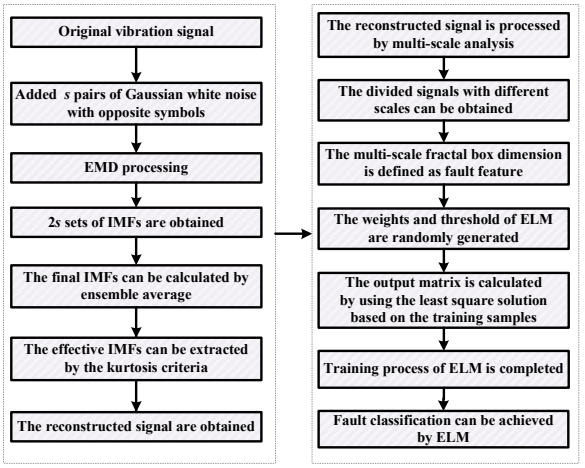

Fig. 5. *Experimental analysis flowchart*

The vibration signals of four types of planetary gears are collected and shown in Fig. 6. It can be seen that the vibration signals have FM and AM characteristics, and that is because of the influences of complex structure, assembly error, motor, and load. The vibration signal of normal gear includes more shock components, and there are no obvious rules. The gear surface structure and its stiffness are changed when the planetary gear fault occurs, and the additional shock components are generated in the meshing process. Those cause the vibration signals of the faulty gear to be more complex. It can be seen

from Fig. 6 that the gear status cannot be recognized based on the time-domain signals.

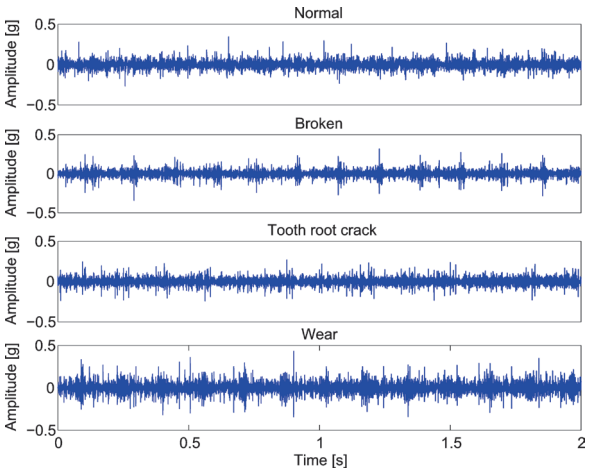

Fig. 6. *Four types of vibration signals*

The proposed fault diagnosis method is used to process the vibration signal. The vibration signal is sampled as a digital signal, which is composed of a series of data points. It is decomposed by CEEMD according to Eqs. (1) to (4). The number of the added Gaussian white noise S is set to 50, the amplitude of the added Gaussian white noise $n_s(t)$ is set to 0.25 times the standard deviation of the original signal, and EMD process $E(\ )$ is defined in [4]. The vibration signal of wear gear is selected as an example to show the decomposition result of CEEMD, and the decomposition result of EEMD is compared. The decomposition results of EEMD and CEEMD for wear gear are shown in Figs. 7 and 8, respectively.

The complex signal can be expressed as multiple signals with simple characteristics and are easy to analyse with CEEMD; 13 IMFs and a residual signal is obtained, and the residual signal is called IMF14 for convenience. They are arranged from high-frequency to low-frequency. It can be found that the decomposition result of CEEMD is superior to that of EEMD. For EEMD, it is obvious that there is the phenomenon of modal aliasing in IMF6, IMF7, and IMF8. Modal aliasing refers to an IMF that contains the features with great differences or similar features distributed in different IMFs. That causes the waveforms of adjacent IMFs exhibit an aliasing phenomenon, which affects the extraction of the fault features. The quality of the obtained IMFs by CEEMD is greatly improved, and the modal aliasing degree is further reduced. The decomposition errors of EEMD and CEEMD are calculated and shown in Fig. 9. The magnitude of the decomposition error of EEMD is

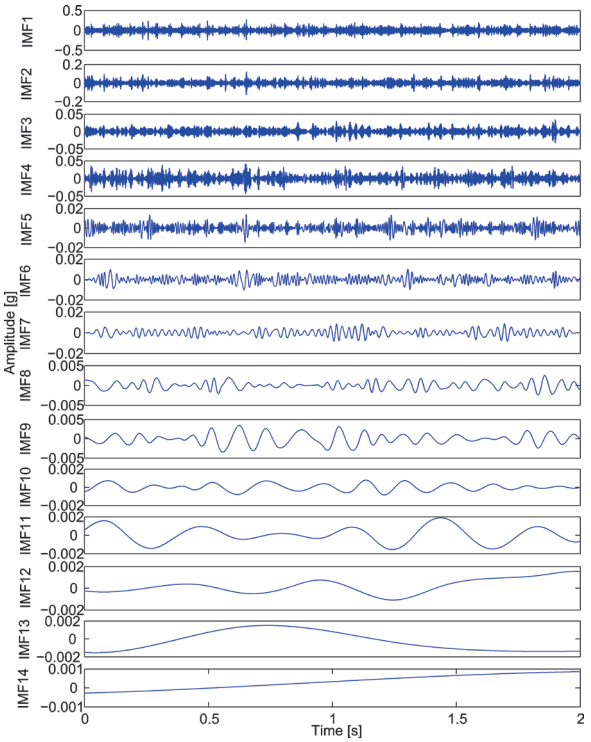

Fig. 7. *Decomposition results of EEMD for wear gear*

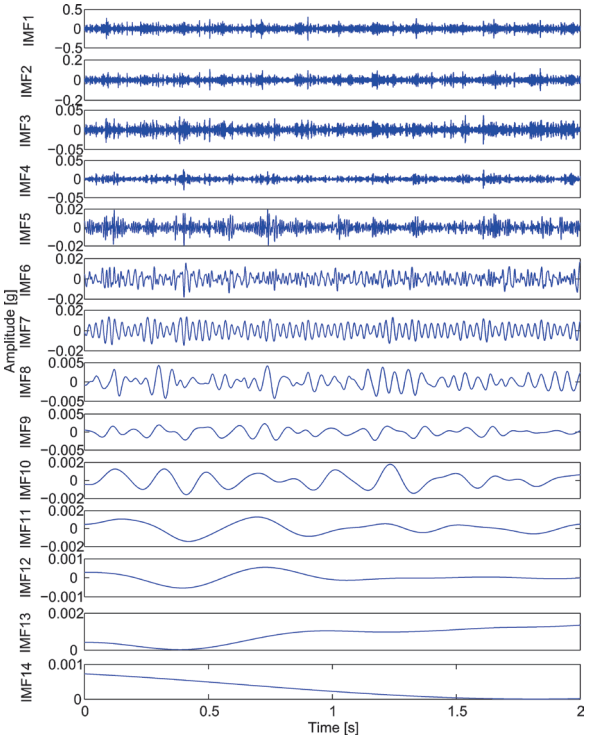

Fig 8. *Decomposition result of CEEMD for wear gear*

10^{-4}, and it is obviously more than that of CEEMD. The magnitude of the decomposition error of CEEMD

is only 10^{-7}. CEEMD can better eliminate the residual noise generated by the added Gaussian white noise, and the decomposition error can be reduced.

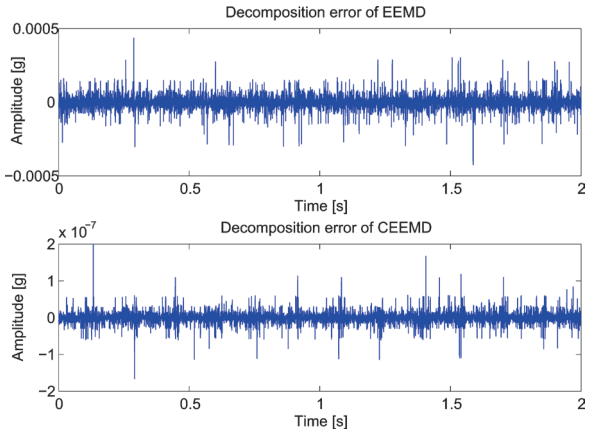

Fig. 9. *Decomposition errors of EEMD and CEEMD*

The IMFs containing different information can be obtained by CEEMD, and the fault feature information generated by the planetary gear is only contained in some IMFs. The shock components are generated during the meshing process of the planetary gear, and the fault feature information is usually contained in the shock components. Thus, kurtosis is defined as selection criteria to select the effective IMFs associated with fault feature information. Each IMF can be seen as a single digit signal, and the kurtosis of each IMF can be calculated according to Eq. (13), and it is shown in Fig. 10.

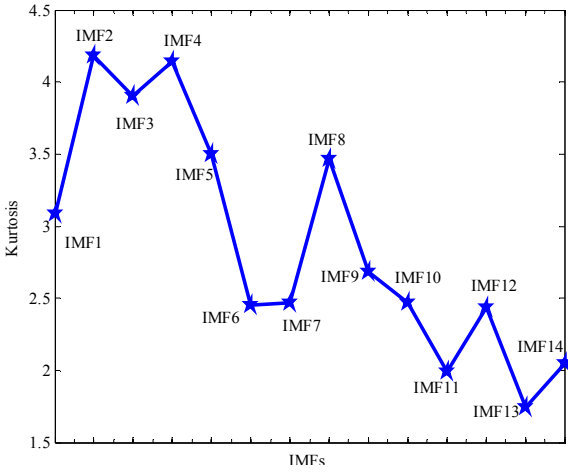

Fig. 10. *Kurtosis of each IMF*

It can be seen from Fig. 10 that IMF2 has the maximum kurtosis; it reaches 4.1825. IMF11 has the minimum kurtosis; it reaches 1.9930. In general, more shock components are included in the signal when its kurtosis is greater than 3. Thus, IMF1, IMF2, IMF3, IMF4, IMF5, and IMF8 are selected as the effective IMFs. The reconstructed signal of the effective IMFs can be obtained, and it includes more shock feature information generated by planetary gear faults.

The multi-scale fractal box dimension of the reconstructed signal of the effective IMFs should be extracted. The reconstructed signal includes 8400 data points, and the scale factor τ is set to 20. Twenty signals containing different scales are obtained from the reconstructed signal according to Eq. (6), and their fractal box dimensions are calculated according to Eqs. (7) to (11). The multi-scale fractal box dimension of four types of planetary gears is shown in Fig. 11.

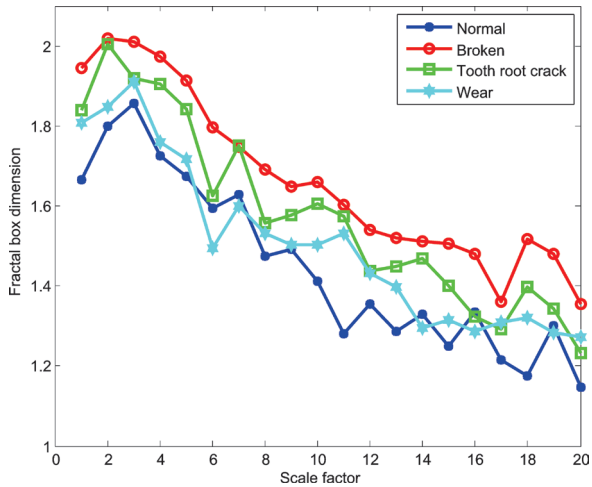

Fig. 11. *Multi-scale fractal box dimension of four types of planetary gears*

The multi-scale fractal box dimension of four types of planetary gears is decreasing with the increasing of the multi-scale factor τ. Due to the additional shock components being produced when planetary gear faults occur, the multi-scale fractal box dimension of normal gear is less than that of other gears. The fault degree of a broken gear is relatively serious, so its multi-scale fractal box dimension is relatively large. It also can be found that there are the differences of the fractal box dimension under different scales for four types of planetary gears, so the multi-scale fractal box dimension is an effective fault feature. Moreover, next, the planetary gear status can be recognized by combining ELM.

The training sample set is built to train ELM, and each gear status has 50 training samples. The multi-scale fractal box dimension of each sample constitutes the input matrix in Eq. (15). Because the multi-scale factor τ is set to 20, the input matrix has 20 dimensions. Because the samples should be divided into four types,

the output layer of ELM has four neurons. Meanwhile, four types of gear statuses should be labeled: the normal gear is labeled by [1 0 0 0], broken gear is labeled by [0 1 0 0], the gear with tooth root crack is labeled by [0 0 1 0], and the wear gear is labeled by [0 0 0 1], and they constitute the output matrix in Eq. (15). If the number of hidden neurons and the activation function with infinitely differentiable are determined, the connection weight w in Eq. (12) and the threshold ϕ of the hidden neurons in Eq. (14) can be randomly selected. The connection weight β can be calculated according to Eqs. (16) to (20), and the training process of ELM is completed. The number of hidden neurons and the type of activation function have a large influence on the application of ELM, and in general, the activation function can be selected from 'sig' function, 'sin' function or 'hardlim' function. To determine the optimal number of hidden neurons and the type of activation function, the root mean square error (RMSE) can be used to evaluate the training performance of ELM. The RMSE of the ELM with different hidden neurons and different activation functions is shown in Fig. 12. In addition, in order to verify the recognition performance of ELM, the testing sample set is built. The vibration signals of four types of planetary gear statuses are divided into the testing samples to be analysed, and each gear status has 50 testing samples. The testing samples are recognized by the trained ELM, and the overall recognition rate of the ELM with different hidden neurons and different activation functions is shown in Fig. 13.

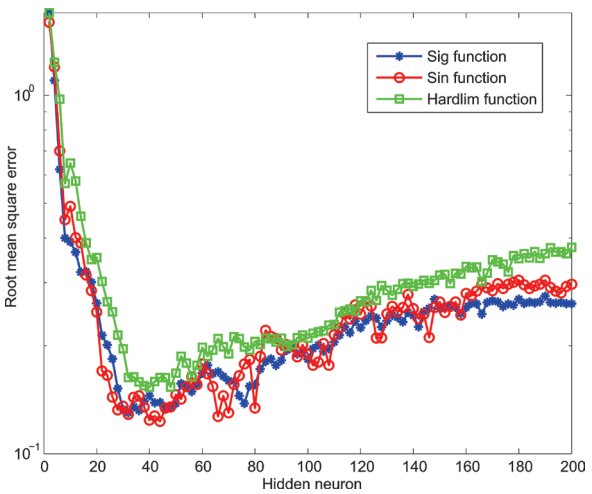

Fig. 12. *RMSE of the ELM with different hidden neurons and different activation functions*

For different activation functions, it can be found from Fig. 12 that the RMSE has a smaller value when the number of hidden neurons is between 30 and 50. Moreover, when the number of hidden neurons reaches a certain level, the RMSE increases with the increasing of hidden neurons. The ELM with 44 hidden neurons and 'sin' function has the minimum RMSE, and it reaches 0.1230. In addition, it can be seen from Fig. 13 that different hidden neurons and different activation functions have great influence on the recognition performance of ELM. When the number of hidden neurons increases to a certain extent, the overall recognition rate is gradually decreasing. The overall recognition rate has a maximum value when the ELM has 44 hidden neurons and 'sin' function, and it reaches 92.5 %. Therefore, the ELM with 44 hidden neurons and 'sin' function has the best recognition performance, and the detailed recognition rate of the ELM for different planetary gear statuses is shown in Table 2.

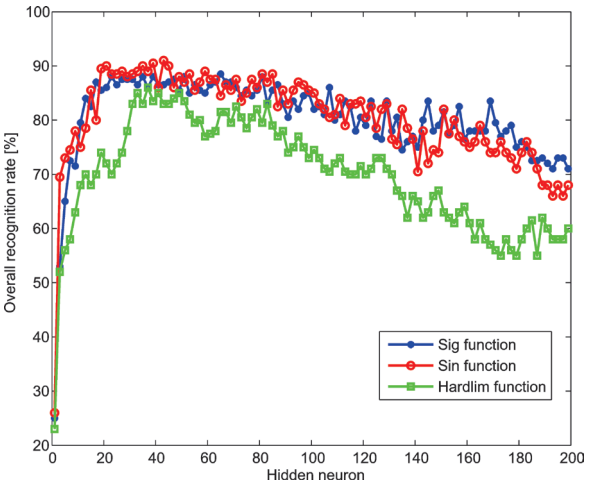

Fig. 13. *Overall recognition rate of the ELM with different hidden neurons and different activation functions*

Table 2. *Detailed recognition rate of the ELM with 44 hidden neurons and 'sin' function*

	Normal gear	Broken gear	Tooth root crack	Wear gear
Recognition rate [%]	94	100	86	90

The testing samples of four types of planetary gear statuses are used to verify the recognition performance of ELM. The recognition rate of each planetary gear status is obtained by calculating the number correctly recognized by ELM when the testing samples belong to some planetary gear status that is recognized by ELM. The multi-scale fractal box dimension of the broken gear is the largest, and it has a great difference with other gears; therefore,

the broken gear has the best recognition rate, and it reaches 100 %. The recognition rate of gear with tooth root crack is relatively low, and it reaches 86 %. The recognition rates of normal gear and wear gear are 94 % and 90 %, respectively. The ELM with 44 hidden neurons and 'sin' function has a better recognition rate for different planetary gear statuses. The recognition rate can be used to show the ability to distinguish different planetary gear statuses, and it also can be seen as the credibility of the recognition result of ELM. In the practical application process, the vibration signal is continuously collected, and it also needs to be divided into multiple continuous samples for processing. More samples should be used to improve the reliability of the results, and the final diagnosis result needs to be determined by the recognition results of multiple samples. Next, the proposed method is applied to industrial experiments.

4 INDUSTRIAL EXPERIMENT APPLICATION

The fault diagnosis system based on the proposed method is applied to an industrial experiment in the Xutuan coal mine in the Anhui province of China, and it is used to monitor the planetary gear of shearer cutting parts. Before the establishment of the fault diagnosis system, the training samples of different planetary gear statuses of shearer cutting parts are prepared, and their fault features are extracted to train the fault diagnosis system according to the proposed method. A fault diagnosis system can be established, and it is used to identify the planetary gear faults of shearer cutting part. In the practical application process for shearer cutting part, the acceleration sensor is installed on the shell of the bearing seat of the planetary gear, and the data acquisition instrument is used to sample the signal of the acceleration sensor. The collected signal is transmitted to the PC fault diagnosis software, which is compiled with Labview. The experiment is shown in Fig. 14, and the data acquisition instrument is shown in Fig. 15.

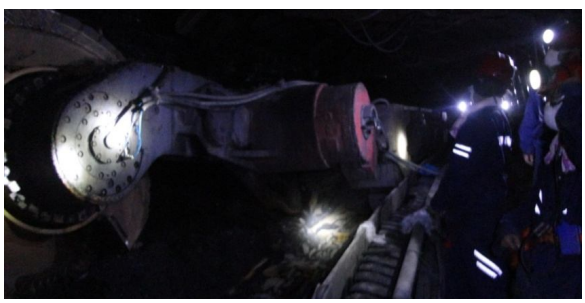

Fig. 14. *Diagnosis experiment of planetary gear of shearer cutting part*

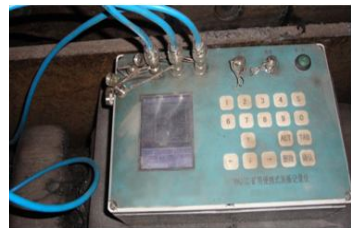

Fig. 15. *Data acquisition instrument*

The sampling frequency is set to 5000 Hz. Because the vibration signal is collected continuously, it needs to be divided into multiple samples for analysis, and each sample is set to include 10000 data points. In the process of diagnosis analysis, 50 samples are set to be analysed each time, and the diagnosis result of each sample can be obtained. The probabilities belonging to different statuses can be counted. The final diagnosis result is the status with the maximum probability, and the corresponding probability can be regarded as the reliability of the final diagnosis result. More samples can improve the accuracy and reliability of diagnosis. Next, an example of the detected fault in the experiment application is selected to illustrate. The vibration signals of normal operation and the detected fault, which are obtained by the established fault diagnosis system is shown in Fig. 16. In addition, their multi-scale fractal box dimensions are extracted according to the proposed method, and they are shown in Fig. 17.

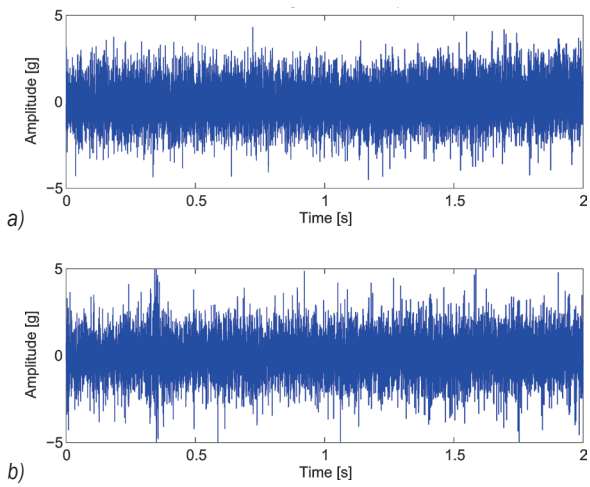

Fig. 16. *The vibration signals of a) normal operation, and b) detected fault*

It can be seen from the figures that the vibration amplitude of the detected fault is larger in comparison with the vibration signal of normal operation. The shock components are increased, and their amplitude

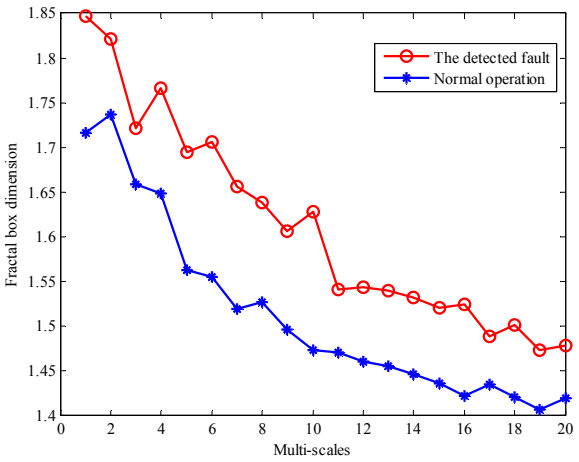

Fig. 17. *Multi-scale fractal box dimensions of normal operation and the detected fault*

is relatively strong. The multi-scale fractal box dimension of the detected fault increases comparing with that of normal operation, and it greatly deviates from the multi-scale fractal box dimension of normal operations.

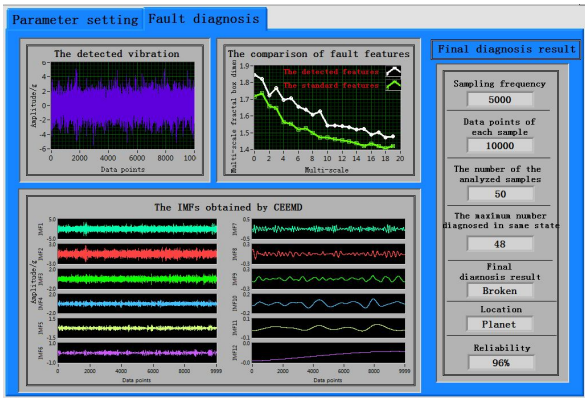

Fig. 18. *Fault diagnosis software*

Fig. 19. *The diagnosed broken gear*

In the established fault diagnosis system, the fault diagnosis software is shown in Fig. 18. The final diagnosis results, the detected vibration signal, the IMFs obtained by CEEMD, the comparison between the detected features and the standard features can be displayed on the software interface. The number of analysis samples is set to 50, and 48 of them are diagnosed as broken gear. Thus, the final diagnosis result is that the monitored planetary gear is broken, and the credibility of the final diagnosis result is 96%. The shearer cutting part is repaired after determining the diagnosis result, and it is found that the breakage happens on the first stage planetary gear of shearer cutting part. The diagnosed broken gear is shown in Fig. 19. The experiment proves that the proposed fault diagnosis method of a planetary gear based on multi-scale fractal box dimension of CEEMD and ELM can accurately recognize the planetary gear status, and it is an effective fault diagnosis method.

5 CONCLUSIONS

A fault diagnosis method of planetary gear based on multi-scale fractal box dimension of CEEMD and ELM is proposed. CEEMD is proposed to improve the decomposition effect of EEMD, and a series of high-quality IMFs which contain more accurate feature information can be obtained by CEEMD. The effective IMFs associated with the shock feature information generated by planetary gear faults are selected by the kurtosis criterion, and they are reconstructed. The reconstructed signal is processed by the multi-scale algorithm, and the feature information contained in the signals with different scales is extracted and quantified by the fractal box dimension. The multi-scale fractal box dimension is used as the fault feature information, and it is defined as the input of ELM. The influence of the number of hidden neurons and the type of activation function on the recognition performance of ELM is analysed. The testing sample set is built and used to verify the recognition effect, and the recognition rates of the ELM with different hidden neurons and different activation functions are calculated and compared. In addition, a fault diagnosis system is established based on the proposed method, and the industrial experiment application is carried out. The experiments show that the proposed method based on multi-scale fractal box dimension of CEEMD and ELM can be used to recognize planetary gear status, and it is an effective fault diagnosis method for planetary gears.

6 ACKNOWLEDGEMENTS

This work was supported by a Project Funded by the Priority Academic Program Development of Jiangsu Higher Education Institutions, the Top-notch Academic Programs Project of Jiangsu Higher Education Institutions, Natural Science Foundation of Jiangsu Province (Grant Number BK20141128) and Fundamental Research Funds for the Central Universities (grant number 2015YC02); this support is gratefully acknowledged.

7 REFERENCES

[1] Chen, X.H., Cheng, G., Shan, X.L., Hu, X., Guo, Q. (2015). Research of weak fault feature information extraction of planetary gear based on ensemble empirical mode decomposition and adaptive stochastic resonance. *Measurement*, vol. 73, p. 55-67, **DOI:10.1016/j.measurement.2015.05.007**.

[2] Fyler, D.C., Inalpolat, M. (2016). A dynamic model for double-planet planetary gearsets. *Journal of Vibration and Acoustics*, vol. 138, no. 2, Article ID 021006, **DOI:10.1115/1.4032181**.

[3] Do, V.T., Nguyen, L.C. (2016). Adaptive empirical mode decomposition for bearing fault detection. *Strojniški vestnik - Journal of Mechanical Engineering*, vol. 62, no. 5, p. 281-290, **DOI:10.5545/sv-jme.2015.3079**.

[4] Huang, N.E., Shen, Z., Long, S.R. (1998). The empirical mode decomposition and the Hilbert spectrum for nonlinear and non-stationary time series analysis. *Proceedings of the Royal Society A*, vol. 454, p. 903-995, **DOI:10.1098/rspa.1998.0193**.

[5] Cheng, G., Cheng, Y.L., Shen, L.H., Qiu J.B., Zhang, S. (2013). Gear fault identification based on Hilbert–Huang transform and SOM neural network. *Measurement*, vol. 46, no. 3, p. 1137-1146, **DOI: 10.1016/j.measurement.2012.10.026**.

[6] Wu, Z., Huang, N.E. (2009). Ensemble empirical mode decomposition: a noise-assisted data analysis method. *Advances in Adaptive Data Analysis*, vol. 1, no. 1, p. 1-41, **DOI:10.1142/S1793536909000047**.

[7] Perez-Ramirez, C.A., Amezquita-Sanchez, J.P., Adeli, H., Valtierra-Rodriguez, M., Camarena-Martinez, D., J. Romero-Troncoso, R.J. (2016). New methodology for modal parameters identification of smart civil structures using ambient vibrations and synchrosqueezed wavelet transform. *Engineering Applications of Artificial Intelligence*, vol. 48, p. 1-12, **DOI:10.1016/j.engappai.2015.10.005**.

[8] Begum, S., Barua, S., Filla, R., Ahmed, M.U. (2014). Classification of physiological signals for wheel loader operators using multi-scale entropy analysis and case-based reasoning. *Expert Systems with Applications*, vol. 41, no. 2, p. 295-305, **DOI:10.1016/j.eswa.2013.05.068**.

[9] Liu, Y., Lin, J.L., Chen, K. (2015). A stable algorithm of box fractal dimension and its application in pore structure. *Rare Metal Materials and Engineering*, vol. 44, no. 4, p. 800-804, **DOI:10.1016/S1875-5372(15)30050-3**.

[10] Khazaee, M., Ahmadi, H., Omid, M. (2013). Feature-level fusion based on wavelet transform and artificial neural network for fault diagnosis of planetary gearbox using acoustic and vibration signals. *Insight*, vol. 55, no. 6, p. 323-329, **DOI:10.1784/insi.2012.55.6.323**.

[11] Aghbashlo, M., Shamshirband, S., Tabatabaeic, M., Yee, P.L., Larimi, Y.N. (2016). The use of ELM-WT (extreme learning machine with wavelet transform algorithm) to predict exergetic performance of a DI diesel engine running on diesel/biodiesel blends containing polymer waste. *Energy*, vol. 94, p. 443-456, **DOI:10.1016/j.energy.2015.11.008**.

[12] Ahila, R., Sadasivam, V., Manimala, K. (2015). An integrated PSO for parameter determination and feature selection of ELM and its application in classification of power system disturbances. *Applied Soft Computing*, vol. 32, p. 23-37, **DOI:10.1016/j.asoc.2015.03.036**.

[13] Colominas, M.A., Schlotthauer, G., Torres, M.E. (2014). Improved complete ensemble EMD: A suitable tool for biomedical signal processing. *Biomedical Signal Processing and Control*, vol. 14, p. 19-29, **DOI:10.1016/j.bspc.2014.06.009**.

[14] Cong, F.Y., Chen, J., Dong, G.M. (2012). Spectral kurtosis based on AR model for fault diagnosis and condition monitoring of rolling bearing. *Journal of Mechanical Science and Technology*, vol. 26, no. 2, p. 301-306, **DOI:10.1007/s12206-011-1029-0**.

[15] Li, Y.B., Xu, M.L., Wang, R.X., Huang, W.H. (2016). A fault diagnosis scheme for rolling bearing based on local mean decomposition and improved multiscale fuzzy entropy. *Journal of Sound and Vibration*, vol. 360, p. 277-299, **DOI:10.1016/j.jsv.2015.09.016**.

[16] Zheng, Z., Jiang, W., Wang, Z., Zhu, Y., Yang, K. (2015). Gear fault diagnosis method based on local mean decomposition and generalized morphological fractal dimensions. *Mechanism and Machine Theory*, vol. 91, p. 151-167, **DOI:10.1016/j.mechmachtheory.2015.04.009**.

[17] Sá, J.J.M., Backes, A.R. (2016). ELM based signature for texture classification. *Pattern Recognition*, vol. 51, p. 395-401, **DOI:10.1016/j.patcog.2015.09.014**.

[18] Heras, D.B., Argüello, F., Quesada-Barriuso, P. (2014). Exploring ELM-based spatial-spectral classification of hyperspectral images. *International Journal of Remote Sensing*, vol. 35, no. 2, p. 401-423, **DOI:10.1080/01431161.2013.869633**.

[19] Huang, G.B., Zhou, H., Ding, X., Zhang, R. (2012). Extreme learning machine for regression and multiclass classification. *IEEE Transactions on Systems, Man, and Cybernetics, Part B: Cybernetics*, vol. 42, no. 2, p. 513-529, **DOI:10.1109/TSMCB.2011.2168604**.

Strojniški vestnik - Journal of Mechanical Engineering 63(2017)1, 56-64

DOI:10.5545/sv-jme.2016.4027 Original Scientific Paper
Received for review: 2016-09-03
Received revised form: 2016-10-14
Accepted for publication: 2016-11-03

Modelling Length/Pressure Hysteresis of a Pneumatic Artificial Muscle using a Modified Prandtl-Ishlinskii Model

Yixiang Liu – Xizhe Zang* – Zhenkun Lin – Xinyu Liu – Jie Zhao
Harbin Institute of Technology, State Key Laboratory of Robotics and System, China

Pneumatic artificial muscles have been widely used in various fields owing to their inherent compliance and high power-to-weight ratio. However, the natural hysteresis nonlinearity including length/pressure hysteresis and force/pressure hysteresis degrades their performance in precise tracking control, making it necessary to build a mathematical hysteresis model for hysteresis compensation. This paper deals with the modelling of length/pressure hysteresis of pneumatic artificial muscles. The length/pressure hysteresis loops measured by the isotonic test are found to be asymmetric and independent of the external load when the load is small. Considering that the classical Prandtl-Ishlinskii model is only effective for symmetric hysteresis, a modified Prandtl-Ishlinskii model is proposed to describe the length/pressure hysteresis behaviour. The developed model utilizes two asymmetric operators with simple mathematical forms to independently model the ascending branch and descending branch of hysteresis loops. The model parameters are identified using the recursive least square algorithm. Comparisons between simulation results and experimental measurements demonstrate that the proposed model can characterize the asymmetric major hysteresis loop and minor hysteresis loops with high accuracy.

Keywords: asymmetric hysteresis, length/pressure hysteresis, modified Prandtl-Ishlinskii model, pneumatic artificial muscles, recursive least square algorithm

Highlights

- *The length/pressure hysteresis of a single pneumatic artificial muscle is found to be asymmetric and independent of small external load through experimental measurements.*
- *This paper proposes a modified Prandtl-Ishlinskii model composing of two independent asymmetric play operators to characterize the length/pressure hysteresis of the pneumatic artificial muscle.*
- *The parameters of the modified Prandtl-Ishlinskii model is identified quite conveniently using the recursive least mean algorithm.*
- *The proposed model has high accuracy in describing the major hysteresis loop and minor hysteresis loops.*

0 INTRODUCTION

Pneumatic artificial muscle (PAM) is a relatively new kind of elastic pneumatic actuator. Simply put, PAM is a cylindrical rubber bladder surrounded by a braided fibre sheath, with both ends closed [1]. When supplied with compressed gas, the bladder experiences radial expansion, consequently generating axial contraction and exerting a pulling force on an external load [2]. Owing to its particular structure and materials, PAM has several unique advantages compared to hydraulic and electric actuators, for instance, high power-to-weight ratio, compact size, inherent compliance, as well as low cost [3] and [4]. Therefore, PAMs are increasingly used in industrial applications [5] to [7], bionic robots [8] to [10], surgical instruments [11], rehabilitation devices [12] to [14], and so forth.

For a PAM, the input is internal pressure, while the outputs are contraction length and pulling force. In other words, the contraction length and pulling force depend on the internal pressure. Thus, the position or force control of PAM is based on the control of internal pressure. However, the relationships between the length and internal pressure in the pressurizing and depressurizing processes are different. The same are true for the relationships between the force and internal pressure. These differences are called length/pressure hysteresis and force/pressure hysteresis, respectively, and are caused by the elasticity of the bladder, and the friction between the inner tube and the outer sheath [15]. The hysteretic behaviour increases system nonlinearity and makes it more difficult to achieve precise position or force tracking control. To deal with this problem, one possible solution is to build a mathematical hysteresis model and utilize its inversion for hysteresis compensation to obtain the approximately linear response of PAM.

To date, many investigations of the hysteresis modelling of PAM have been made. Van Damme et al. [16] studied the hysteresis behaviour of pleated PAM, and found that the dimensionless force was independent of gauge pressure and contraction rate. A Preisach-based hysteresis model was built for the force/contraction characteristics, which only performed well in the contraction range from 7 % to 20 %. Through investigation, Vo-Minh et al. [17] to [19] found the pressure/length hysteresis and the force/length hysteresis [20] were quasi-rate independent

*Corr. Author's Address: State Key Laboratory of Robotics and System, Harbin Institute of Technology, 2 Yikuang Street, Harbin 150080, China, zangxizhe@hit.edu.cn

and history dependent, and could be described by the Maxwell-slip model. Then they further extended their work to model the torque/angle hysteresis of a joint driven by PAMs in antagonistic configuration, using the model derived for individual PAMs [21]. Frank Schreiber adopted the classical Preisach model to describe the static hysteresis behaviour of a manipulator driven by antagonistic PAMs and then used its inversion for feedforward hysteresis compensation [22] and [23]. Kosaki and Sano [24] also constructed the contraction/pressure hysteresis model in the form of the Preisach model for compensation of a parallel manipulator driven by three PAMs. Ito et al. [25] modelled the length/pressure hysteresis of a PAM at a certain external load using a stop model, which was a function of the contraction ratio and applied load. Lin et al. [26] investigated pressure/length hysteresis characteristics for a dual PAM system using three different models, including a Prandtl-Ishlinskii model, a Bouc-Wen model, and a Maxwell-slip model. Comparisons indicated that the former two models were more effective than the third one.

Among the above studies, the Preisach model is the most widely used because of its applicability in various hysteretic actuators, such as electromagnetic actuators [27], piezoceramic actuators [28] and [29], and magnetostrictive actuators [30]. However, its mathematical form is highly complex, making it difficult to derive the analytic inverse model. In contrast, the Prandtl-Ishlinskii model has simple play operators, which facilitate calculation of the inverse hysteresis model [31] and [32]. Nevertheless, it is not applicable to modelling asymmetric hysteresis behaviour, owing to the symmetric property of the classical play operators [33] and [34].

This paper is mainly intended for the modelling of the asymmetric length/pressure hysteresis of PAM, which is essential for position tracking control. Based on the classical Prandtl-Ishlinskii model, a modified Prandtl-Ishlinskii (MPI) model is proposed by replacing the classical play operators with more flexible elementary operators. This model utilizes two independent operators to describe the ascending branch and descending branch of hysteresis loops respectively. In addition, the model parameters can be identified using a recursive least square algorithm within several steps.

The remaining content of this paper is organized as follows. First, the isotonic experiment setup for measuring the length/pressure hysteresis of PAM is presented. Then the MPI model is introduced in detail. After that, the MPI model is identified and verified using experiment data. Finally, some conclusions and discussion points for future work are given.

1 LENGTH/PRESSURE HYSTERESIS OF PNEUMATIC ARTIFICIAL MUSCLES

1.1 Experimental Apparatus

In this study, an isotonic experiment is carried out to measure the relationships between the contraction, internal pressure, and an external load of a PAM [35]. Currently, there are several PAM manufacturers including FESTO located in Germany, Shadow in the UK, and Bridgestone and HITACHI in Japan. Among them, the PAMs from FESTO are the cheapest and the most readily available. Thus, a commercial PAM from FESTO (DMSP-20-180) is adopted in the experiment, as illustrated in Fig. 1. The inner diameter and nominal length of the contractable membrane are 20 mm and 180 mm respectively. The maximum permitted contraction ratio of the PAM is about 25 % under the maximum operating pressure of 0.6 MPa.

Fig. 1. *A commercial PAM manufactured by FESTO*

Fig. 2 presents the schematic and experimental physical apparatus. The upper end of the PAM is fastened on the fixed frame, and the lower end is mounted with an external load. Compressed air is supplied to the PAM through a proportional pressure regulator. The internal pressure and the contraction of the PAM are measured by a pressure transducer and a linear displacement transducer, respectively. The computer sends the operating voltage to the proportional pressure regulator and receives the measurement signals through the D/A and A/D converters. The outputs of all transducers are recorded on the computer for further analysis.

1.2 Measurement of Length/Pressure Hysteresis

The length/pressure hysteresis of a single PAM was measured using the above experimental apparatus. To reduce the impact of the acceleration of the applied load, the experiment was carried out under the assumption of a quasi-static process. The process of the experiment is as follows. In the initial state,

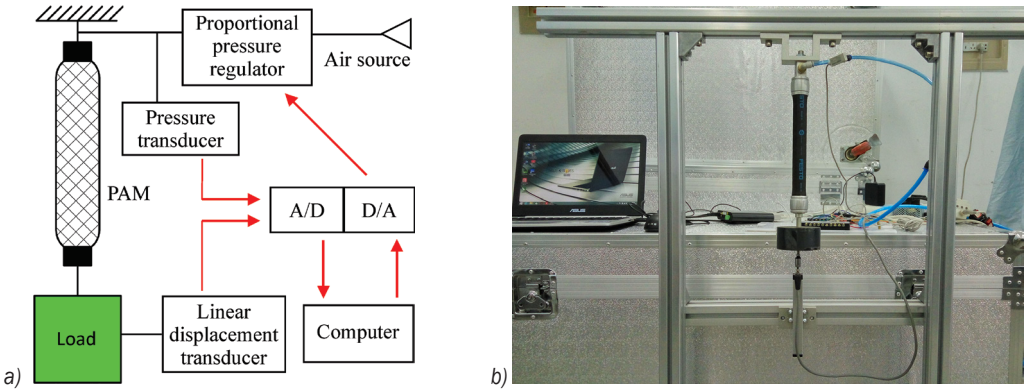

Fig. 2. *Experimental apparatus; a) schematic experimental apparatus, b) physical experimental apparatus*

the gauge pressure inside the PAM was zero, and the PAM was at its full length with a certain load hanging below. Then the PAM was pressurized and depressurized following a reference pressure signal in the form of triangle-wave with various amplitudes. The amplitudes decreased from 0.6 MPa to 0.2 MPa at a constant interval of 0.1 MPa. Fig. 3 shows the reference pressure signal. During this process, the internal pressure and contraction of PAM were measured and recorded. To obtain the relationships between the length/pressure hysteresis and applied external load, the above process was repeated in different cases where the applied load was 1 kg, 2 kg, 3 kg, and 4 kg, respectively.

When the experiment was completed, the measured data were plotted and then analysed. Figs. 4 to 7 show the relationships between the contraction ratio and internal pressure of the PAM when the

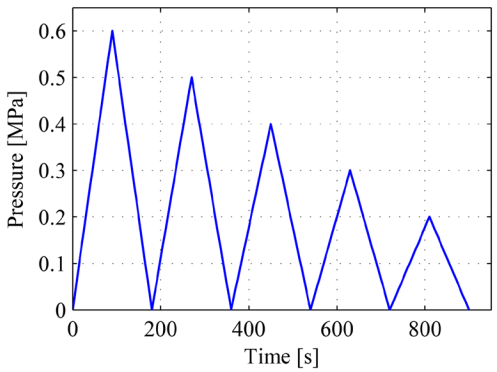

Fig. 3. *The reference pressure signal*

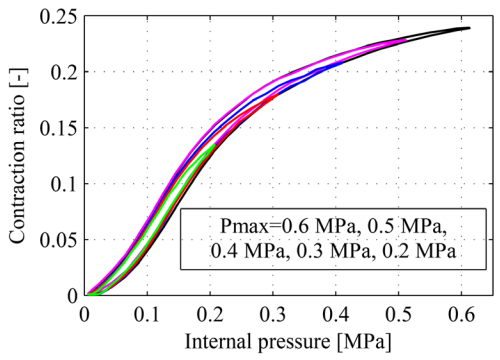

Fig. 4. *Relationship between the contraction ratio and internal pressure in the case of 1 kg load*

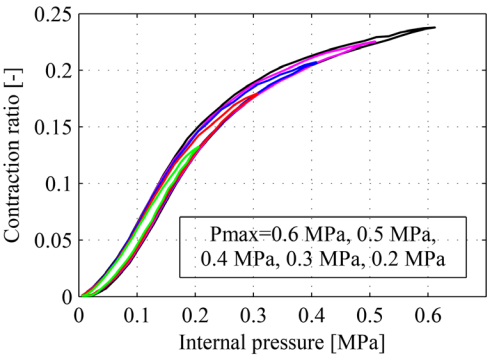

Fig. 5. *Relationship between the contraction ratio and internal pressure in the case of 2 kg load*

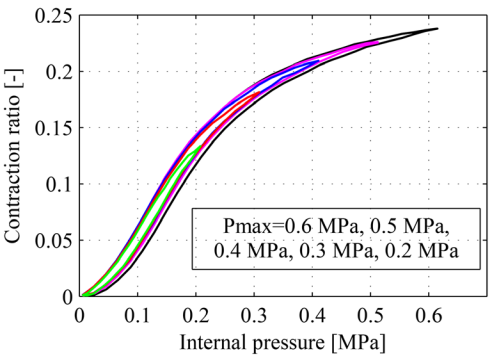

Fig. 6. *Relationship between the contraction ratio and internal pressure in the case of 3 kg load*

external load is 1 kg, 2 kg, 3 kg, and 4 kg, respectively. The contraction ratio ε is calculated using the following equation:

$$\varepsilon = \frac{\Delta L}{L}, \tag{1}$$

where ΔL is the measured contraction, and L is the nominal length of the PAM.

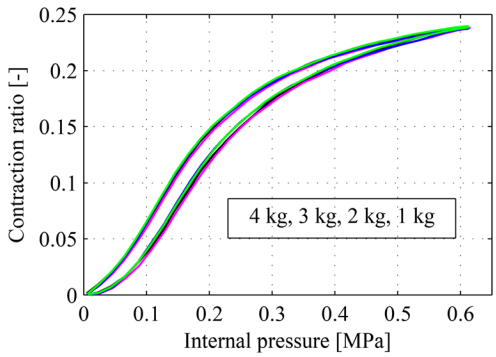

Fig. 7. *Relationship between the contraction ratio and internal pressure in the case of 4 kg load*

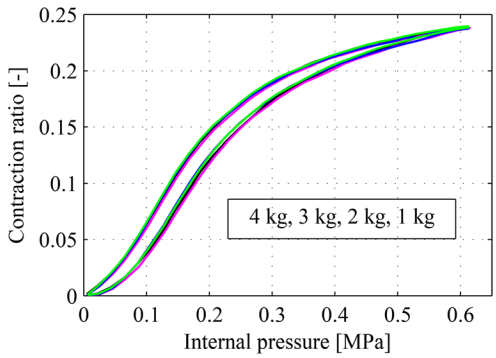

Fig. 8. *The major length/pressure hysteresis loops with different loads*

According to these four figures, several findings can be suggested as follows. First, hysteresis loops including the major loop and minor loops exist between the contraction ratio and internal pressure of PAM. The hysteresis loop formed under the maximum input pressure is termed the major loop. The loops inside the major loop are termed minor loops, which are formed when the input extrema are less than the maximum value. Second, all the hysteresis loops are asymmetric.

Fig. 8 presents the major length/pressure hysteresis loops with different loads. It is quite clear that these major loops almost coincide. Then the third finding can be obtained, i.e. when the external load is small, the length/pressure hysteresis is not dependent on the external load.

2 LENGTH/PRESSURE HYSTERESIS MODELLING

2.1 The Classical Prandtl-Ishlinskii Model

The classical Prandtl-Ishlinskii hysteresis model uses the summation of a finite number of weighted backlash operators with different thresholds to characterize hysteresis behaviour in the continuous space, as presented in Fig. 9. Analytically, suppose C_m represents the space of the piecewise monotone and continuous functions, and $0=t_0<t_1<\cdots<t_N=t_E$ are subintervals in $[0,t_E]$. For the input $u(t)\in C_m[0,t_E]$, which is monotone on each of the subintervals $[t_i,t_{i+1}]$ for $i=0,1,2,...,N-1$, the backlash operator $H_r[u,w_0](t)$ can be defined as [36] and [37]:

$$w(t) = H_r[u,w_0](t) = \\ = \max\left\{u(t)-r, \min\left\{u(t), w(t_i)\right\}\right\}, \tag{2}$$

where $w(t)$ is the output of the backlash operator, r is the threshold value, and w_0 is the initial condition.

According to the initial consistency condition, it will have:

$$w(0) = \max\left\{u(0)-r, \min\left\{u(0), w_0\right\}\right\}. \tag{3}$$

The input-output relationship of the above backlash operator is shown in Fig. 10. Then the output of the hysteresis model can be written as:

$$y(t) = pu(t) + \int_0^R q \cdot H_r[u,w_0](t)dr, \tag{4}$$

where p is a constant parameter, and q is the density function that needs to be identified from the experimental data.

To facilitate calculation and application of the hysteresis model in computer programming, it is necessary to approximate the integral using summation. Thus, the classical Prandtl-Ishlinskii hysteresis model in the discrete form can be expressed as:

$$y(t) = pu(t) + \sum_{i=1}^{n} q_i H_{ri}[u,w_0](t), \tag{5}$$

with n representing the number of backlash operators.

Research has shown that the classical Prandtl-Ishlinskii model only works well for characterizing symmetric hysteresis loops. Then its viability and effectiveness are checked using the experimental data. The model validation result is shown in Fig. 11, by comparing the measured length/pressure hysteresis loop with the simulated hysteresis loop. Obviously, the classical Prandtl-Ishlinskii model cannot describe the hysteresis behaviour of the PAM.

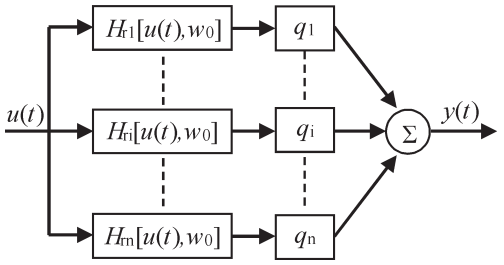

Fig. 9. *Block diagram of the classical Prandtl-Ishlinskii model*

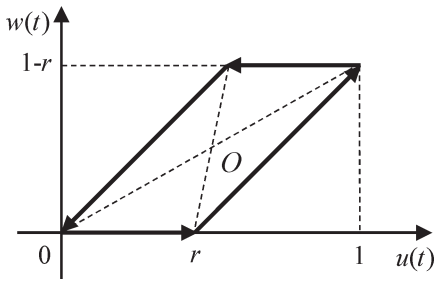

Fig. 10. *Input-output relationship of the backlash operator*

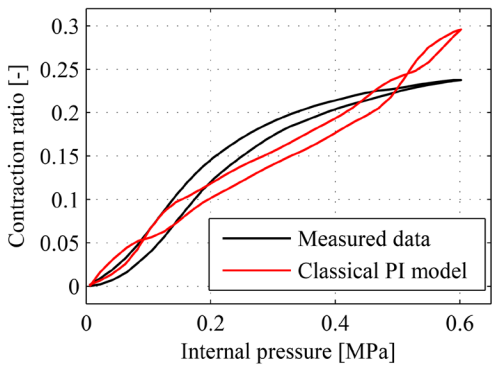

Fig. 11. *Model validation result of classic Prandtl-Ishlinskii model*

2.2 The Modified Prandtl-Ishlinskii Model

Since the classical Prandtl-Ishlinskii model is only valid for symmetric hysteresis description, a new MPI model is proposed to characterize the asymmetric length/pressure hysteresis of the pneumatic artificial muscle. According to the changes of input signals, a whole hysteresis loop can be divided into two parts: ascending branch for input increase and descending branch for input decrease. Therefore, the MPI model is also based on two independent asymmetric play operators: the play operator of the ascending branch and the play operator of the descending branch. The two play operators describe the ascending hysteretic nonlinearity and descending hysteretic nonlinearity of the system, respectively. Moreover, their combination is capable of modelling the full hysteresis loop.

For any piecewise monotone input function $u(t)\in C_m[0,\ t_E]\rightarrow[0,\ 1]$, the elementary play operator of the ascending branch is defined as:

$$H_r^a[u,w_0](t)=\begin{cases} w_{i-1} & \Delta u\geq 0, u_i\leq r \\ \dfrac{1+r}{1-r}(u_i-r) & \Delta u\geq 0, r<u_i\leq \dfrac{1+r}{2} \\ u_i & \Delta u\geq 0, u_i>\dfrac{1+r}{2} \\ u_i & \Delta u<0 \end{cases}. \quad (6)$$

Similarly, the elementary play operator of the descending branch is defined as:

$$H_r^d[u,w_0](t)=\begin{cases} f(u_m) & \Delta u\geq 0 \\ u_i & \Delta u<0, \dfrac{1-r}{2}\leq u_i<1-r \\ \dfrac{1+r}{1-r}u_i-r & \Delta u<0, u_i\geq 1-r \\ u_i & \Delta u<0 \end{cases}. \quad (7)$$

In the above equation, $f(u_m)$ is the function of the dominant extrema of the input um, which is described by a quadratic polynomial, expressed as:

$$f(u_m)=c_0+c_1\cdot u_m+c_2\cdot u_m{}^2. \quad (8)$$

For the elementary play operators, the threshold values r are distributed within the range not exceeding the maximum amplitude of the input, i.e., $0\leq r<1$. Figs. 12 and 13 present the input-output relationship of the play operator of the ascending branch and of the descending branch respectively.

Calculating the weighted sum of the two play operators, the output of the modified hysteresis model can be written as:

$$y(t)=pu(t)+\sum_{i=1}^{n}q_i^a H_{ri}^a[u,w_0](t)+ +\sum_{i=1}^{n}q_i^d H_{ri}^d[u,w_0](t), \quad (9)$$

where q_i^a is the density function of the play operator of the ascending branch, and q_i^d is the density function of the play operator of the descending branch.

The two play operators are subject to the following constraints:

$$\begin{cases} H_{ri}^a[1,w_0](t)=1 \\ H_{ri}^d[1,w_0](t)=1 \\ p+\sum_{i=1}^{n}q_i^a H_{ri}^a[1,w_0](t)+\sum_{i=1}^{n}q_i^d H_{ri}^d[1,w_0](t)=1 \end{cases}. \quad (10)$$

Substituting Eq. (10) into Eq. (9), the output of the hysteresis model can be rewritten as:

$$y(t) = u(t) + \sum_{i=1}^{n} q_i^a (H_{ri}^a [u, w_0](t) - u(t)) + \\ + \sum_{i=1}^{n} q_i^d (H_{ri}^d [u, w_0](t) - u(t)). \quad (11)$$

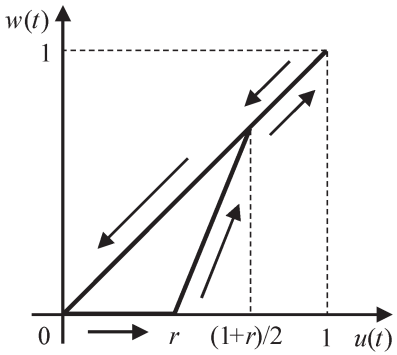

Fig. 12. *The elementary play operator of the ascending branch*

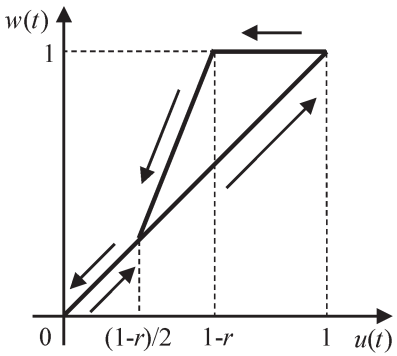

Fig. 13. *The elementary play operator of the descending branch*

3 MODEL IDENTIFICATION AND VALIDATION

In the MPI model, there are a total of $2n+3$ parameters that need to be identified. They are the weightings q_i^a $(i=1,2,\cdots,n)$ of the play operators of the ascending branch, the weightings q_i^d $(i=1,2,\cdots,n)$ of the play operators of the descending branch, and the coefficients c_i $(i=1,2,3)$ of the quadratic polynomial function $f(u_m)$. The input and output of the MPI model are constrained within the range $[0,1]$. Therefore, the measured data of the isotonic experiment, i.e., the internal pressure and the contraction ratio denoted as (x_i, y_i) need to be normalized from the physical space to the model space to satisfy the constraints first before they can be used for the identification of model parameters [38]. When the identification is completed, the outputs of the hysteresis model are transformed back to the physical space. The normalization of measured data from the physical space to the model space is defined as:

$$\begin{cases} x_{ni} = \dfrac{x_i - x_{\min}}{x_{\max} - x_{\min}} \\ y_{ni} = \dfrac{y_i - y_{\min}}{y_{\max} - y_{\min}} \end{cases}. \quad (12)$$

The thresholds r of the elementary play operators are predefined as:

$$r_i = \frac{i-1}{n} \qquad 1 \le i \le n. \quad (13)$$

The whole identification process can be divided into two steps. First, the weightings of the elementary play operators are identified with the measured data of the major hysteresis loop. After that, the coefficients of the quadratic polynomial function are calculated with the measured data of the minor hysteresis loops. The model parameters are identified using a recursive least squares (RLS) algorithm, which is one of the most well-known algorithms used in signal processing, parameters estimation and system control which recursively finds the coefficients minimizing a weighted linear least squares cost function relating to the training data. It has several unique advantages, such as fast convergence rate, easy programming, and avoiding the eigenvalue spread problem. RLS algorithm works as follows: when the observations of the system parameters are obtained, the new observations are updated by adding a correction to the old values, and then the process iterates until the observations reach acceptable accuracy. The parameter iteration law is given by:

$$\begin{cases} K(k) = \dfrac{P(k-1)\cdot\phi^T(k-1)}{1+\phi(k-1)\cdot P(k-1)\cdot\phi^T(k-1)} \\ P(k) = [I - K(k)\cdot\phi(k-1)]\cdot P(k-1) \\ q(k) = q(k-1) + K(k)\cdot[y(k) - \phi(k-1)\cdot q(k-1)] \end{cases}, \quad (14)$$

with $q(k)$ representing the observations of the k^{th} estimation. The iteration law ensures that the parameters will converge to stable values after several steps of iteration.

The number of play operators determines the accuracy of hysteresis modelling. More play operators will guarantee higher accuracy but demand heavier computation. Fig. 14 shows the major length/pressure hysteresis loops simulated by MPI models with different numbers of play operators. It can be easily found that when the number is greater than or equal

to 20, the model can predict the major hysteresis loop with sufficient accuracy. Table 1 presents the identified weightings of play operators in the case in which the number is 20. The quadratic polynomial function $f(u_m)$ is identified and written as:

$$f(x_m) = 0.5496 + 1.0109x_m - 0.5661x_m^2. \quad (15)$$

Fig. 15 shows the model validation result of the MPI model. Obviously, the MPI model can describe the hysteresis behaviour of the PAM including both major loop and minor loops with very high accuracy.

Table 1. *The identified weightings of play operators*

r_i	q_i^a	q_i^d	r_i	q_i^a	q_i^d
0	-0.0014	-0.0014	0.5	-0.0277	0.0689
0.05	0.5689	0.0915	0.55	0.0476	0.0718
0.1	0.3541	0.0523	0.6	-0.0141	0.0152
0.15	0.3932	-0.0811	0.65	-0.0679	0.0989
0.2	0.1718	0.0415	0.7	-0.0778	0.0695
0.25	-0.1755	0.0804	0.75	-0.0379	0.0974
0.3	-0.1351	0.0268	0.8	0.0116	0.0403
0.35	-0.2026	0.0013	0.85	-0.0655	0.0481
0.4	-0.0506	0.0871	0.9	-0.0217	0.0157
0.45	-0.1292	-0.0031	0.95	-0.0378	0.0110

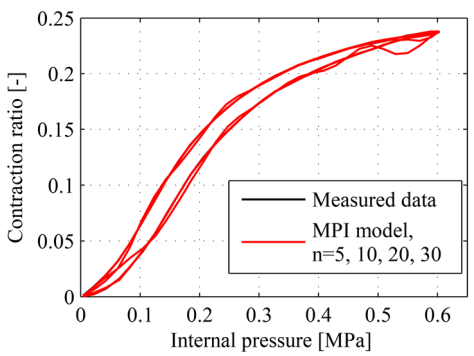

Fig. 14. *Major length/pressure hysteresis loops simulated by MPI models with different numbers of play operators*

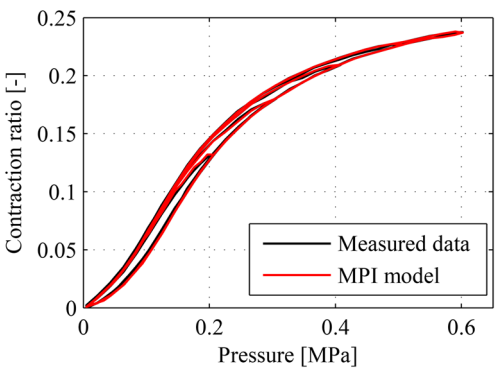

Fig. 15. *Model validation result of the MPI model*

4 CONCLUSION AND DISCUSSION

In this paper, a modified Prandtl-Ishlinskii model is proposed to model the asymmetric length/pressure hysteresis behaviour of PAMs. The proposed model is combined with two asymmetric play operators which are used to independently describe the ascending branch and descending branch of the hysteresis loops. The model parameters are identified using the recursive least square algorithm, making the identification process very simple and convenient. Compared to existing hysteresis models, the benefits of the proposed MPI model are in its relatively more concise mathematical form and its high validity and effectiveness in reproducing the asymmetric length/pressure hysteresis including both major hysteresis loop and minor hysteresis loops. Furthermore, the MPI model can simplify the derivation of the inverse hysteresis model. In fact, the inversion of the length/pressure hysteresis can be obtained in a more straightforward way instead of mathematical computation. More precisely, taking the contraction ratio as the input and the pressure as the output, the inverse length/pressure hysteresis model can be directly identified from measurements using the proposed MPI model.

The above benefits suggest that the new MPI model can play some role in the hysteresis compensation of PAMs. Therefore, it will be interesting to study its implementation in the position control of a single PAM and/or robotic joints actuated by PAMs. In this work, only the quasi-static hysteretic behaviour of PAMs is studied because the dynamic hysteresis is too complicated to be modelled precisely. When the MPI model is applied to dynamic systems, various model uncertainties and external disturbances that will affect its effectiveness remain. However, some intelligent control methods, such as nonlinear adaptive control and robust nonlinear control can deal with the above issue. Therefore, in the future, we will focus on researching a position controller that combines the robust feedback control scheme with MPI model-based hysteresis compensation to achieve better position tracking performance of PAMs.

5 ACKNOWLEDGEMENTS

This research is funded and supported by the National Natural Science Foundation of China (Grant No. 51675116).

6 REFERENCES

[1] Tondu, B. (2012). Modelling of the McKibben artificial muscle: A review. *Journal of Intelligent Material Systems and Structures*, vol. 23, no. 3, p. 225-253, **DOI:10.1177/1045389X11435435**.

[2] Daerden, F., Lefeber, D. (2000). Pneumatic artificial muscles: actuators for robotics and automation. *European Journal of Mechanical and Environmental Engineering*, vol. 47, no. 1, p. 10-21.

[3] Caldwell, D.G., Tsagarakis, N., Medrano-Cerda, G.A. (2000). Bio-mimetic actuators: polymeric pseudo muscular actuators and pneumatic muscle actuators for biological emulation. *Mechatronics*, vol. 10, no. 4-5, p. 499-530, **DOI:10.1016/S0957-4158(99)00071-9**.

[4] Davis, S., Tsagarakis, N., Canderle, J., Caldwell, D.G. (2003). Enhanced modeling and performance in braided pneumatic muscle actuators. *International Journal of Robotics Research*, vol. 22, no. 3-4, p. 213-227, **DOI:10.1177/0278364903022003006**.

[5] Palko, A., Smrček, J. (2011). The use of pneumatic artificial muscles in robot construction. *Industrial Robot: An International Journal*, vol. 38, no. 1, p. 11-19, **DOI:10.1108/01439911111097805**.

[6] Hošovský, A., Havran, M. (2012). Dynamic modeling of one degree of freedom pneumatic muscle-based actuator for industrial applications. *Technical Gazete - Tehnički Vjesnik*, vol. 19, no. 3, p. 673-681.

[7] Robinson, R.M., Kothera, C.S., Wereley, N.M. (2014). Control of a heavy-lift robotic manipulator with pneumatic artificial muscles. *Actuators*, vol. 3, no. 2, p. 41-65, **DOI:10.3390/act3020041**.

[8] Ogawa, K., Narioka, K., Hosoda, K. (2011). Development of whole-body humanoid "Pneumat-BS" with pneumatic musculoskeletal system. *Proceedings of the 2011 IEEE/RSJ International Conference on Intelligent Robots and Systems*, p. 4838-4843, **DOI:10.1109/IROS.2011.6095091**.

[9] Liu, Y.X., Zang, X.Z., Liu, X.Y., Wang, L. (2015). Design of a biped robot actuated by pneumatic artificial muscles. *Bio-Medical Materials and Engineering*, vol. 26, no. s1, p. S757-S766, **DOI:10.3233/bme-151367**.

[10] Lei, J., Yu, H. (2014). Dynamics analysis of bionic flexible body driven by pneumatic artificial muscle for quadruped robot. *Journal of Shanghai Jiaotong University*, vol. 48, no. 12, p. 1688-1693. (in Chinese)

[11] Li, H.B., Kawashima, K., Tadano, K., Ganguly, S., Nakano, S. (2013). Achieving haptic perception in forceps' manipulator using pneumatic artificial muscle. *IEEE/ASME Transactions on Mechatronics*, vol. 18, no. 1, p. 74-85, **DOI:10.1109/TMECH.2011.2163415**.

[12] Jiang, X.Z, Wang, Z.H., Zhang, C., Yang, L. (2015). Fuzzy neural network control of the rehabilitation robotic arm driven by pneumatic muscles. *Industrial Robot: An International Journal*, vol. 42, no. 1, p. 36-43, **DOI:10.1108/IR-07-2014-0374**.

[13] Huang, J., Tu, X.K., He, J.P. (2016). Design and evaluation of the RUPERT wearable upper extremity exoskeleton robot for clinical and in-home therapies. *IEEE Transactions on Systems, Man, and Cybernetics: Systems*, vol. 46, no. 7, p. 926-935, **DOI:10.1109/TSMC.2015.2497205**.

[14] Jamwal, P.K., Hussain, S., Ghayesh, M.H., Rogozina, S.V. (2016). Impedance control of an intrinsically compliant parallel ankle rehabilitation robot. *IEEE Transactions on Industrial Electronics*, vol. 63, no. 6, p. 3638-3647, **DOI:10.1109/TIE.2016.2521600**.

[15] Tondu, B., Lopez, P. (2000). Modeling and control of McKibben artificial muscle robot actuators. *IEEE Control Systems*, vol. 20, no. 2, p. 15-38, **DOI:10.1109/37.833638**.

[16] Van Damme, M., Beyl, P., Vanderborght, B., Van Ham, R., Vanderniepen, I., Versluys, R., Daerden, F., Lefeber, D. (2008). Modeling hysteresis in pleated pneumatic artificial muscles. *Proceedings of the 2008 IEEE Conference on Robotics, Automation and Mechatronics*, p. 471-476, **DOI:10.1109/RAMECH.2008.4681431**.

[17] Vo-Minh, T., Tjahjowidodo, T., Ramon, H., Van Brussel, H. (2009). Non-local memory hysteresis in a pneumatic artificial muscle (PAM). *Proceedings of the 17th Mediterranean Conference on Control and Automation*, p. 640-645.

[18] Vo-Minh, T., Tjahjowidodo, T., Ramon, H., Van Brussel, H. (2009). Control of a pneumatic artificial muscle (PAM) with model-based hysteresis compensation. *Proceedings of the IEEE/ASME International Conference on Advanced Intelligent Mechatronics*, p. 1082-1087, **DOI:10.1109/AIM.2009.5229730**.

[19] Vo-Minh, T., Tjahjowidodo, T., Ramon, H., Van Brussel, H. (2010). Cascade position control of a single pneumatic artificial muscle-mass system with hysteresis compensation. *Mechatronics*, vol. 20, no. 3, p. 402-414, **DOI:/10.1016/j.mechatronics.2010.03.001**.

[20] Vo-Minh, T., Tjahjowidodo, T., Ramon, H., Van Brussel, H. (2011). A new approach to modeling hysteresis in a pneumatic artificial muscle using the Maxwell-slip model. *IEEE/ASME Transactions on Mechatronics*, vol. 16, no. 1, p. 177-186, **DOI:10.1109/TMECH.2009.2038373**.

[21] Vo-Minh, T., Kamers, B., Tjahjowidodo, T., Ramon, H., Van Brussel, H. (2010). Modeling torque-angle hysteresis in a pneumatic muscle manipulator. *Proceedings of the IEEE/ASME International Conference on Advanced Intelligent Mechatronics*, p. 1122-1127, **DOI:10.1109/AIM.2010.5695805**.

[22] Schreiber, F., Sklyarenko, Y., Schlüter, K., Schmitt, J., Rost, S., Raatz, A., Schumacher, W. (2011). Tracking control with hysteresis compensation for manipulator segments driven by pneumatic artificial muscles. *Proceedings of the IEEE International Conference on Robotics and Biomimetics*, p. 2750-2755, **DOI:10.1109/ROBIO.2011.6181721**.

[23] Schreiber, F., Sklyarenko, Y., Runge, G., Schumacher, W. (2012). Model-based controller design for antagonistic pairs of fluidic muscles in manipulator motion control. *Proceedings of the 17th International Conference on Methods and Models in Automation and Robotics*, p. 499-504, **DOI:10.1109/MMAR.2012.6347868**.

[24] Kosaki, T., Sano, M. (2011). Control of a parallel manipulator driven by pneumatic muscle actuators based on a hysteresis model. *Journal of Environment and Engineering*, vol. 6, no. 2, p. 316-327, **DOI:10.1299/jee.6.316**.

[25] Ito, A., Washizawa, N., Kiyoto, K., Furuya, N. (2011). Control of pneumatic actuator in consideration of hysteresis

characteristics. *Proceedings of the IEEE International Conference on Robotics and Biomimetics*, p. 2541-2546, **DOI:10.1109/ROBIO.2011.6181687**.

[26] Lin, C.J., Lin, C.R., Yu, S.K., Chen, C.T. (2015). Hysteresis modeling and tracking control for a dual pneumatic artificial muscle system using Prandtl-Ishlinskii model. *Mechatronics*, vol. 28, p. 35-45, **DOI:10.1016/j.mechatronics.2015.03.006**.

[27] Mittal, S., Menq, C.H. (2000). Hysteresis compensation in electromagnetic actuators through Preisach model inversion. *IEEE/ASME Transactions on Mechatronics*, vol. 5, no. 4, p. 394-409, **DOI:10.1109/3516.891051**.

[28] Song, G., Zhao, J.Q., Zhou, X.Q., De Abreu-Garcia, J.A. (2005). Tracking control of a piezoceramic actuator with hysteresis compensation using inverse Preisach model. *IEEE/ASME Transactions on Mechatronics*, vol. 10, no. 2, p. 198-209, **DOI:10.1109/TMECH.2005.844708**.

[29] Xiao, S.L., Li, Y.M. (2013). Modeling and high dynamic compensating the rate-dependent hysteresis of piezoelectric actuators via a novel modified inverse Preisach model. *IEEE Transactions on Control Systems Technology*, vol. 21, no. 5, p. 1549-1557, **DOI:10.1109/TCST.2012.2206029**.

[30] Li, Z., Su, C.Y., Chai, T.Y. (2014). Compensation of hysteresis nonlinearity in magnetostrictive actuators with inverse multiplicative structure for Preisach model. *IEEE Transactions on Automation Science and Engineering*, vol. 11, no. 2, p. 613-619, **DOI:10.1109/TASE.2013.2284437**.

[31] Aschemann, H., Schindele, D. (2014). Comparison of model-based approaches to the compensation of hysteresis in the force characteristic of pneumatic muscles. *IEEE Transactions on Industrial Electronics*, vol. 61, no. 7, p. 3620-3629, **DOI:10.1109/TIE.2013.2287217**.

[32] Janaideh, M.A.I., Rakheja, S., Su, C.Y. (2011). An analytical generalized Prandtl–Ishlinskii model inversion for hysteresis compensation in micropositioning control. *IEEE/ASME Transactions on Mechatronics*, vol. 16, no. 4, p. 734-744, **DOI:10.1109/TMECH.2010.2052366**.

[33] Li, Z., Feng, Y., Chai, T.Y., Fu, J., Su, C.Y. (2012). Modeling and compensation of asymmetric hysteresis nonlinearity for magnetostrictive actuators with an asymmetric shifted Prandtl-Ishlinskii model. *Proceedings of the American Control Conference*, p. 1658-1663.

[34] Gu, G.Y., Zhu, L.M., Su, C.Y. (2014). Modeling and compensation of asymmetric hysteresis nonlinearity for piezoceramic actuators with a modified Prandtl–Ishlinskii model. *IEEE Transactions on Industrial Electronics*, vol. 61, no. 3, p. 1583-1595, **DOI:10.1109/TIE.2013.2257153**.

[35] Jiang, F.L., Tao, G.L., Liu, H. (2015). Research on PMA properties and humanoid lower limb application. *Proceedings of the IEEE International Conference on Advanced Intelligent Mechatronics*, p. 1292-1297, **DOI:10.1109/AIM.2015.7222717**.

[36] Chen, Y.S., Qiu, J.H., Sun, H. (2013). A hybrid model of Prandtl-Ishlinskii operator and neural network for hysteresis compensation in piezoelectric actuators. *International Journal of Applied Electromagnetics and Mechanics*, vol. 41, p. 335-347, **DOI:10.3233/JAE-131648**.

[37] Aljanaideh, O., Rakheja, S., Su, C. Y. (2013). A Prandtl-Ishlinskii model for characterizing asymmetric and saturated hysteresis of smart material actuators. *Intelligent Robotics and Applications, Lecture Notes in Computer Science*, vol. 8103, p. 635-643, **DOI:10.1007/978-3-642-40849-6_63**.

[38] Jiang, H., Ji, H.L., Qiu, J.H., Chen, J.Q. (2010). A modified Prandtl-Ishlinskii model for modeling asymmetric hysteresis of piezoelectric actuators. *IEEE Transactions on Ultrasonics, Ferroelectrics, and Frequency Control*, vol. 57, no. 5, p. 1200-1210, **DOI:10.1109/TUFFC.2010.1533**.

Strojniški vestnik - Journal of Mechanical Engineering 63(2017)1, 65-77
DOI:10.5545/sv-jme.2016.3450
Original Scientific Paper
Received for review: 2016-01-27
Received revised form: 2016-07-11
Accepted for publication: 2016-09-15

Model Reduction of a Load-Sensing Hydraulic System via Activity Index Analysis

Quanyi Hu[1,*] – Hong Zhang[1] – Shujun Tian[1] – Xuxin Qin[2]
[1] Dalian University of Technology, School of Mechanical Engineering, China
[2] Linde Hydraulics GmbH & Co. KG, Germany

A load-sensing hydraulic system is an energy-saving fluid power transmission that supplies "on-demand" flow at a prescribed pressure margin greater than load pressure. In the paper, based on bond graph methodology, a complex and non-linear load-lensing (LS) hydraulic system model is constructed, in which the dynamic behaviours of an LS valve are taken into account. Moreover, a series of experiments are performed to validate the model. Two reduced models based on activity index analysis are obtained to achieve a balance between accuracy and complexity. The results indicate that the system order and computation time can be reduced. By quantifying the relative importance of the elements based on activity index analysis, it shows that the inner leakage of the pump plays a major role in system dynamics due to its correlation to the damping coefficient. Furthermore, the results prove the rationality of representing LS pump dynamics with a fourth-order differential equation and the fact that the dynamics of LS valves have not been well-covered in the literature.
Keywords: load-sensing, bond graph, modelling, model reduction, activity index, MORA

Highlights
- *Bond graph modelling of the load-sensing hydraulic system.*
- *Valid bond graph model verified by a series of experiments.*
- *Two reduced models achieving a balance between accuracy and complexity.*
- *The rationality representing the LS pump dynamic with a fourth-order differential equation.*

0 INTRODUCTION

A Load-Sensing hydraulic system (LS) is an energy-saving fluid power transmission that has been widely used in mobile hydraulic applications **[1]** and **[2]**, such as excavator, material handling, and agricultural machines, etc. Furthermore, the combination of electronics and LS system can offer new solutions for accurate motion control.

In principle, the LS system supplies "on-demand" flow at a prescribed pressure margin greater than the highest load pressure and eliminates the bypass losses due to the closed centre. However, the LS system is prone to oscillation, and sometimes becomes unstable due to the feedback of the load-sensing mechanism. Furthermore, as presented by Backe **[3]** and Kim **[4]**, it is also difficult to obtain a satisfactory overall performance because a contradiction exists between energy efficiency and rapid dynamic response, especially over a wide range of operating conditions. Thus, the efforts for the design of the LS system are in general significantly more than that for the conventional hydraulic system with constant delivery pressure or constant delivery flow rate.

To obtain better insight into the performance characteristics of the LS system, a mathematical model is needed. Up to now, considerable research has been conducted into the modelling of the LS system. Most of them used simplified mathematical models with a fourth-order differential equation for the LS pump and ignored the dynamic effects of the LS valve and the cut-off valve. In the literature, Krus **[5]**, Jayaraman **[6]**, Axin **[7]** and Xu **[8]** provided a detailed model of an LS system based on transfer function and a block diagram. Koivumaki and Mattila **[9]** presented a nonlinear model based on a motion control scheme. Wagner **[10]** and Wu **[11]** presented a stability analysis in the frequency domain, but the model did not consider the dynamic of the LS valve and the LS pump was simplified with a second-order system. Sakurai **[12]** and Sakurai et al. **[13]** proposed a design method for the intelligent LS system and studied the computation of the overall efficiency by a simple bond graph model, which neglected the dynamic of the LS pump.

From the viewpoint of modelling, the LS system is essentially a complex, highly nonlinear system which comprises interacting components from mechanical, electrical, hydraulic and control subsystems. Compared to other modelling methods such as block diagram, signal flow graph, etc., bond graph methodology **[14]** to **[16]** is a better graphical representation suitable for modelling the multi-disciplinary dynamic engineering system. As a core representation, the bond graph model can preserve the computational and topological structure. Moreover, it

*Corr. Author's Address: Dalian University of Technology, No.2 Linggong Road, Dalian, China, hqy281@126.com

can be systematically converted into state-equations, transfer functions, block diagrams and signal flow graphs, etc.

In general, the proper model should be as simple as possible for a particular application. However, the modeling procedure often ends with an excessively complex model. Compared to the complex model, a reduced model has several advantages. Firstly, the reduced model is generally a lower-order system, which is conducive to controller design, because the lower-order controller is easier to implement. Secondly, the reduced model can achieve a balance between model accuracy and computation speed, which is crucial for applications requiring both accuracy and efficient computation, such as system optimization and hardware-in-the-loop (HIL) simulation which needs real-time computation. Furthermore, the reduced model is easier to inspect and interpret from physical insights. Finally, reduced model is tractable for the lower number of parameters needed to be identified in system identification and optimization.

The literature for model reduction can be classified into frequency, projection, optimization, and energy-based [17]. Among them, the energy-based model reduction technology is particularly suitable for bond graph models due to the common energy-based nature. The Rayleigh–Ritz methodology [17] exemplifies the core metric for quantifying the relative importance of the elements for a given system. Rosenberg and Zhou [18] proposed a power-based model reduction algorithm. Louca et al. [19] [20] extended Rosenberg and Zhou's algorithm by proposing a new energy-based model reduction metric called activity which avoids the immediate and time-varying decisions about the importance of elements, subsequently, an activity-based model order reduction algorithm (MORA) is proposed.

In this paper, based on the bond graph methodology, an accurate but overly complex LS system model taking into account the dynamic characteristics of the LS valve and the cut-off valve is constructed. Moreover, a series of experiments are performed to validate the bond graph model. Then, based on the activity index analysis, two reduced models with different thresholds are obtained directly from the bond graph level. Thus, a balance between accuracy and complexity is achieved. Furthermore, by quantifying the relative importance of the elements based on the activity index analysis, it proves the rationality representing LS pump dynamics with the fourth-order differential equation in the literature. Finally, the effects of the user-defined threshold on the model accuracy are explored.

1 PRINCIPLE OF THE LS SYSTEM

As shown in Fig. 1, the LS system driving a simple inertial load with damping resistance is illustrated.

In Fig. 1, the heart of the LS system is the LS pump, which is often a swash-plate-type variable displacement piston pump integrating an LS valve and a cut-off valve. The LS valve is essentially a pressure-flow compensator, which compares pump delivery

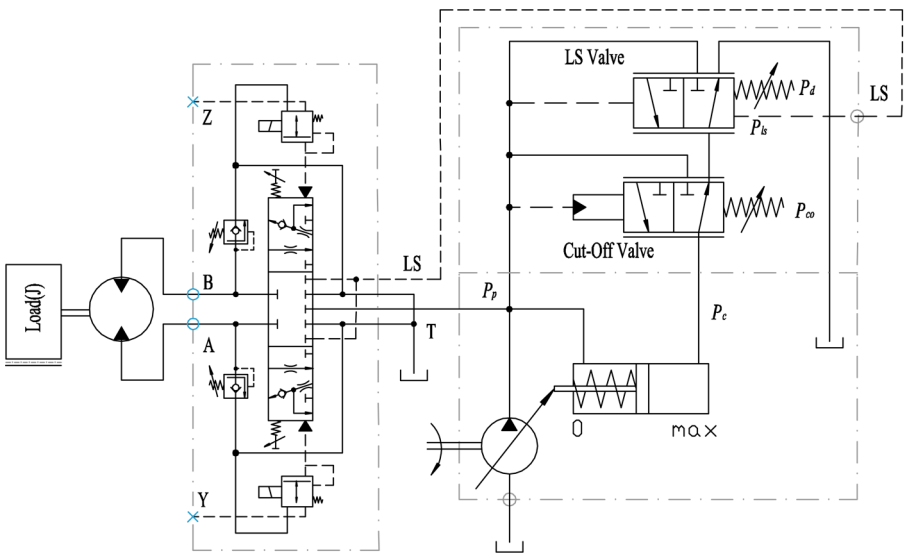

Fig. 1. *Schematic of the LS system*

pressure P_p with load pressure P_{ls} transmitted through the LS port of the directional valve. The operation principles of the LS system are described in detail as follows:

When the directional valve is positioned at the certain opening, the LS valve will sense the pressure difference of pump delivery pressure P_p and load pressure P_{ls} ($\Delta P = P_p - P_{ls}$), and the position of the spool is determined by the acting force generated by the pressure difference ΔP and the initial pre-compression force of the LS spring. The setting value of the LS spring determines the prescribed pressure margin P_d. When the pressure difference ΔP is smaller than the prescribed pressure margin P_d, the spool of the LS valve will be positioned at the right side, as shown in Fig. 1; the pressure oil in the displacement control piston will be released to the reservoir through the cut-off valve and the LS valve; thus the pump displacement will increase. In contrast, when the pressure difference ΔP is larger than the prescribed pressure margin P_d, the pump delivery oil will flow into the displacement control piston; thus, the pump displacement will decrease. Consequently, the pressure difference ΔP is regulated to be retained constant, approximately equal to the prescribed pressure margin P_d.

In addition, the volumetric flow through the directional valve at a given opening can be assessed using Eq. (1):

$$Q_v = C_d \times A \times \sqrt{\frac{2 \times \Delta P}{\rho}}, \tag{1}$$

where Q_v is volumetric flow rate, C_d is flow coefficient of directional valve, and ρ is the density of the oil.

As indicated by Eq. (1), due to the approximately constant pressure difference ΔP, the delivery volumetric flow from the pump is only related to the opening of the directional valve, irrespective of the load pressure, which leads to an "on demand" flow at a prescribed pressure margin higher than the load pressure.

When the LS system is running in an idle condition, the directional valve will be closed, and the LS valve will de-stroke the pump displacement until the output flow is nearly zero, which should be sufficient for covering system leakages and for heat removal. Moreover, the pump delivery pressure goes up to the standby pressure, which is decided by the prescribed pressure margin P_d. The standby pressure is approximately 0.3 MPa higher than the prescribed pressure margin, which is caused by the friction and flow forces acting on the LS spool.

The maximum pump delivery pressure is set for safety by a cut-off valve which will de-stroke the pump displacement when the pump delivery pressure is over the setting value P_{co}.

2 SYSTEM MODELLING BASED ON BOND GRAPH

The LS system is essentially a complex, highly nonlinear system. This section starts from bond graph principles, and then develop the LS model. Finally, a series of experiments are carried out to validate the model.

2.1 Bond Graph Modelling Principles

The bond graph was proposed by Paynter in 1959 [14]. It is a unified modelling method that is particularly suited for modelling multi-disciplinary engineering systems.

The bond graph methodology established a group of unified variables, $\{e(t), f(t), p(t), q(t)\}$, associated with power and energy to model the physical systems. Among them, the effort $e(t)$ and flow $f(t)$ are power variables; the momentum $p(t)$ and displacement $q(t)$ are energy variables.

The power $P(t)$ and energy $E(t)$ flowing into or out of a port can be expressed as Eq. (2) and Eq. (3), respectively.

$$P(t) = e(t) \cdot f(t), \tag{2}$$

$$E(t) = \int^t e(t) f(t) dt = \int^q e(q) dq = \int^p f(p) dp. \tag{3}$$

The bond graph model represents the physical processes in which energy is distributed, transferred and transformed between interconnected ports from different domains with the basic elements $\{R, C, I, S_e, S_f, TF, GY, 0, 1\}$. Inertance "$I$", capacitance "$C$", resistance R, flow source "S_f", and effort source "S_e" represent the physical phenomena which have the definite constitutive relations. Junction structures are assemblages of "0" and "1" junctions, transformer "TF", and gyrator "GY", which enforce the energy conservation constraints among parts of the system. Furthermore, it reflects the topological structure of the physical system.

Bonds denote point-to-point connections between power ports of the subsystems or elements where energy flows into or out of the ports, as shown in Fig. 2a, A and B represent the subsystem or element. The harpoon indicates the instantaneous power flow

direction. Each bond simultaneously brings a pair of conjugated variables, effort $e(t)$ and flow $f(t)$, where the product gives the transmitted power.

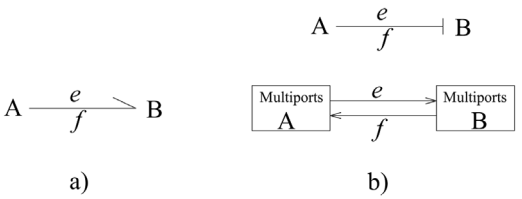

Fig. 2. *Power bond; a) power direction, b) causality assignment*

When formulating the system equations for simulation, causality plays a key role which represents the computational structure of the model. The assigned causality dictates which port variable will be computed as a result, and consequently, the other port variable will be the cause. In the bond graph, the causal stroke in a bond indicates the direction in which the effort variable is directed, as shown in Fig. 2b.

After developing the casual bond graph model, it is straightforward to derive system equations in an orderly fashion, and then to obtain the numerical solutions of the conjugated variables, effort $e(t)$ and flow $f(t)$, on all bonds by many available numerical solvers.

2.2 LS System Modelling

As shown in Fig. 1, the LS system consists of the LS pump, directional valve, fixed displacement motor and inertial load with damping resistance.

2.2.1 LS Pump Modelling

As shown in Fig. 1, the LS pump is a pressure-flow compensated variable displacement pump which is often a swash-plate-type axial piston pump integrating the LS valve and cut-off valve.

Fig. 3a shows the physical structure of the swash-plate-type piston pump that comprises the rotating components and the adjusting mechanism for control of pump displacement [21] and [22]. The pump displacement is a function of the inclination angle α of the swash-plate that is controlled by the control piston, the bias piston, and the return spring.

The governing equation describing the motion of the swash-plate can be written as Eq. (4).

$$J_p\ddot{\alpha} + B_p\dot{\alpha} + (G_p - R)\alpha = D_bP_p - D_cP_c + G_p\alpha_0, \quad (4)$$

where α is the angle of the swash-plate, and P_p, P_c is the pressure of pump output and LS valve outlet, respectively.

The rotating components can be represented by a controlled flow source MS_f, and the pump displacement is controlled by the inclination angle α of the swash-plate. The torque generation on the swash-plate is a function of the geometrical data of the pump and the operating conditions. The flow continuity into the pump discharge chamber and the displacement control piston are both represented by "0" junction. The bond graph model of the LS pump is shown in Fig. 3b.

In the model, the torque coefficient $(G\text{-}R)$ is represented by an equivalent capacitance element K_p.

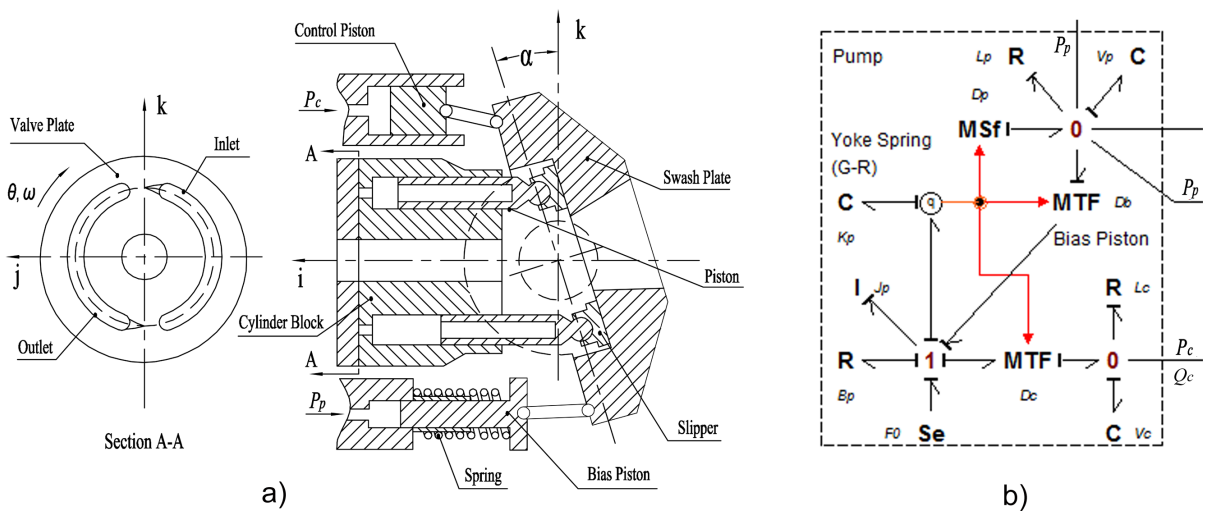

Fig. 3. *LS pump modelling; a) physical structure, b) bond graph model*

The initial setting of the return spring is described with an effort source F_0.

2.2.2 LS valve and Cut-off Valve Modelling

The LS valve is devoted to sensing the pressure difference ΔP between pump delivery pressure P_p and load pressure P_{ls}, the position of the spool is regulated by the acting force generated by the pressure difference ΔP and the initial pre-compression force of the LS spring. The cut-off valve is set for safety by de-stroking the pump when the pump delivery pressure is over the setting value. The physical structure of the LS valve and the cut-off valve is shown in Fig. 4a.

The volumetric flow through the LS valve and the cut-off valve can be expressed in Eq. (5) and Eq. (6).

$$Q_{ls} = \begin{cases} K_{MR3}(P_{ls} + P_d - P_p)\sqrt{P_{ls}} & P_{ls} + P_d > P_p \\ K_{MR4}(P_{ls} + P_d - P_p)\sqrt{P_p - P_{ls}} & P_{ls} + P_d \le P_p \end{cases}, \quad (5)$$

$$Q_c = \begin{cases} K_{MR1}(P_p - P_{co})\sqrt{P_p - P_c} & P_p > P_{co} \\ K_{MR2}(P_p - P_{co})\sqrt{P_c} & P_p \le P_{co} \end{cases}, \quad (6)$$

where Q_{ls}, Q_c are flows to LS valve and cut-off valve, respectively, P_d, P_{co} are the setting pressure of LS valve and cut-off valve, respectively, and P_{ls} is load pressure from the directional valve.

Fig. 4b shows the bond graph model of the LS valve and the cut-off valve. In the model, the dynamic effects in the LS valve and the cut-off valve are considered, including inertia, resistance, and capacitance.

2.2.3 Full LS System Modelling

Based on the above component modelling, an accurate but overly complex bond graph model of the LS system is constructed, as shown in Fig. 5.

As shown in Fig. 5, an electro-proportional directional valve integrating an LS port to transmit the load pressure is used in the system. The dynamics of the valve can be considered as an equivalent first-order model since its dynamics are much faster than that of the pump and load dynamics, the equation can be written as

$$\tau \dot{x}_v + x_v = Ki, \quad (7)$$

where x_v is the opening of the directional valve, and i is an input signal.

As for the fixed displacement piston motor, the inner leakage is considered by coefficient L_m, the capacitance effect between the directional valve and motor are considered by V_{m1} and V_{m2}, respectively.

Generally, the built model is generic, and it can be used for the simulation of various kinds of LS system so long as the schematic is similar to this.

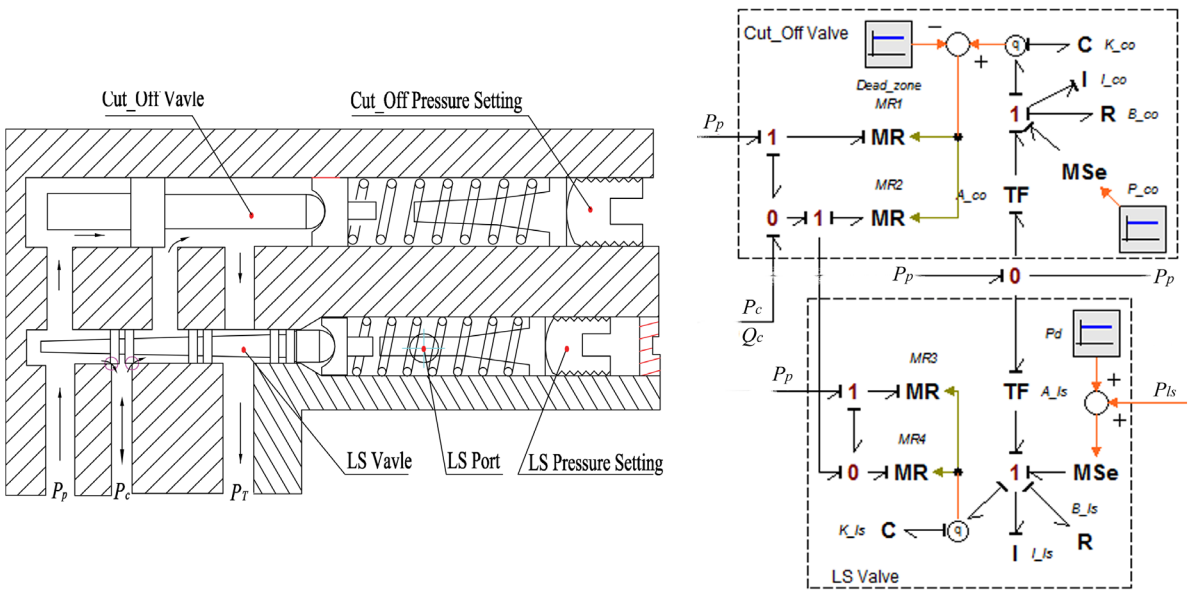

Fig. 4. *LS valve and cut-off valve modelling; a) physical structure, b) bond graph model*

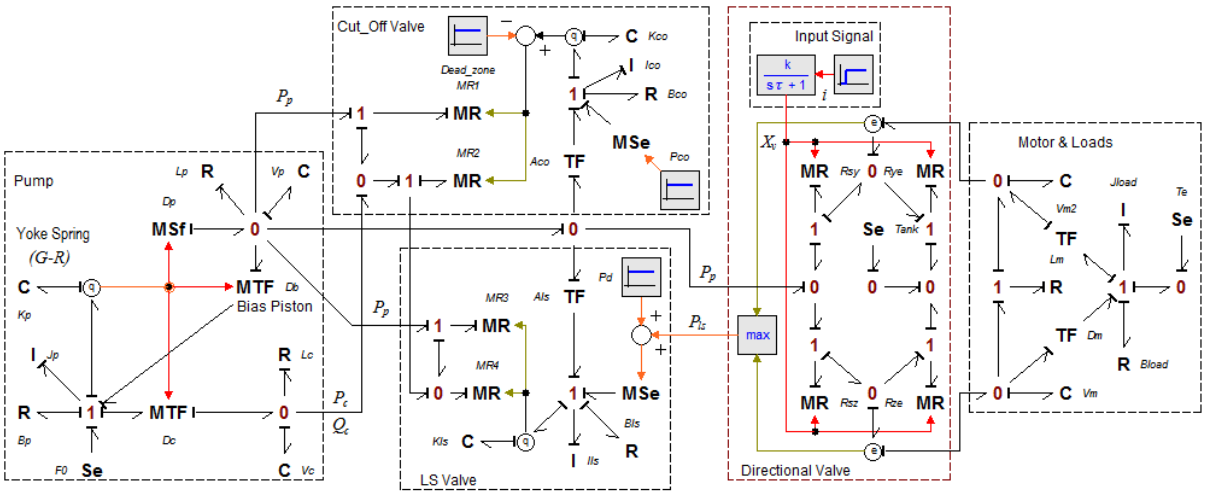

Fig. 5. *The full bond graph model of the LS system*

2.3 Simulation and Experimental Validations

In order to verify the validation of the bond graph model, a series of experiments and computer simulations was performed.

The set-up used in the experiments is shown in Fig. 6. A multifunction data acquisition device, NI USB-6003 (8 AI, 100 kHz; 2 AO, 5 kHz; 1 Counter/Timer, 5 MHz) is used for the measurements and the control function with the LabVIEW software on

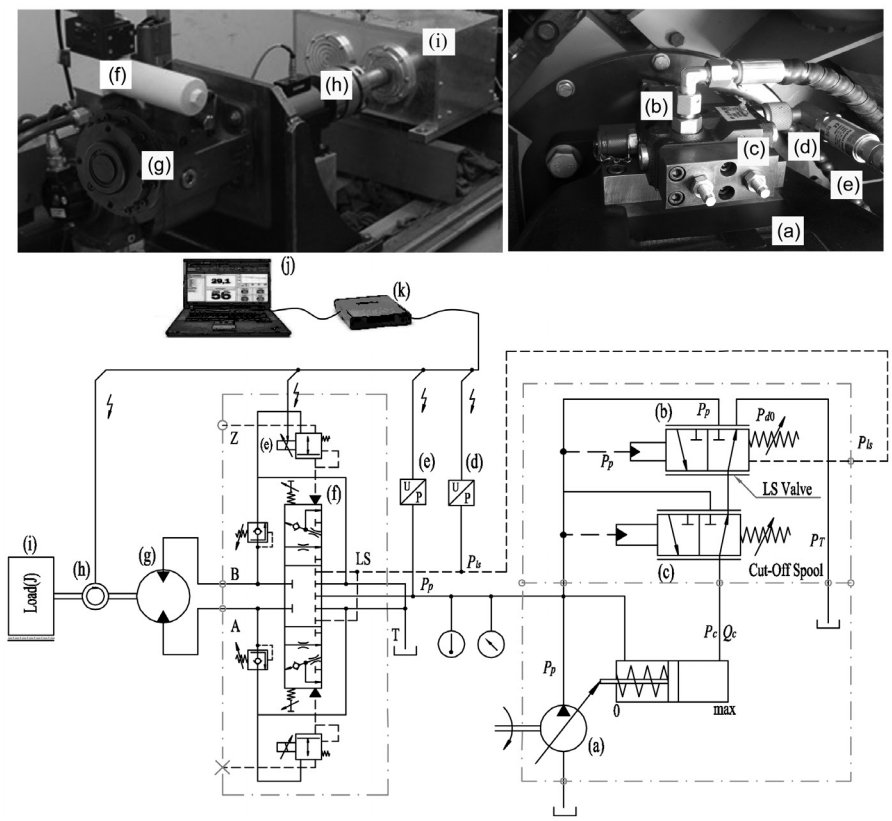

Fig. 6. *Experimental set-up: (a) pump, (b) LS valve, (c) cut-off valve, (d) Pls pressure transducer, (e) Pp pressure transducer, (f) directional valve, (g) motor, (h) tachometer, (i) load, (j) computer, (k) DAQ.*

a ThinkPad E445 laptop computer. NI DIAdem is used for the analysis of the measurement results. An LS pump with 20 cm³/rev displacement volume is selected, and the speed of the E-motor is 800 rpm. A rotating inertial load (J = 0.032 kg·m²) with damping resistance (viscous friction coefficient B_{load} = 0.03 Nm/rad/s) driven by a fixed displacement motor (20 cm³/rev) will be the case to be tested.

As shown in Fig. 6, the pump output pressure and load speed are measured, and one analogue output signal is used for the control of the directional valve. A thermometer is used to measure the fluid temperature, which should be controlled below 60 ºC. The measurement results are filtered by an analogue filter with a cut-off frequency of 25 Hz to remove the high-frequency components.

The main system parameters are listed in Table 1.

Table 1. *The main system parameters*

Name	Value	Unit
β	6.86E+08	Pa
D_p	5.58E–03	(m³/s)/rad
L_p	1.58E–12	(m³/s)/Pa
V_p	1.70E–03	m³
D_b	1.28E–05	m³/rad
L_c	3.51E–12	(m³/s)/Pa
V_c	3.03E–05	m³
D_c	4.43E–05	m³/rad
K_{ls}	4.43E+04	N/m
A_{ls}	3.16E–05	m²
K_c	2.48E–05	(m³/(N$^{1/2}$ s)
K_{co}	3.24E+03	N/m
A_{co}	5.30E–06	m²
K_d	7.45E–05	(m³/s)/m
D_m	5.58E–03	(m³/s)/rad
L_m	3.88E–12	(m³/s)/Pa
V_m	1.83E–04	m³
J	0.032	kg·m²
T_e	0	N·m
B_{load}	0.03	(Nm/rad)/s

The initial state of the directional valve opening is fully closed, and the inertial load is standing still. The setting pressure of the cut-off valve is 12 MPa; the initial prescribed pressure margin P_{d0} is 2.8 MPa. The simulations are performed on an AMD A10-5750M CPU using the open-source OpenModelica software which supports the bond graph library developed with the Modelica language. The derived mathematical equation is solved by the Backward Differentiation Formula (BDF) solver, and the tolerance error is 0.0001.

Two group experiments and simulations are carried out: a) i=10 mA, P_d=0.7 MPa, b) i=20 mA, P_d=1.07 MPa. The opening step signal of the directional valve is ignited at 1 s.

The dynamic responses of pump delivery pressure P_p, load pressure P_{ls}, load speed and load displacement are selected as the comparison variables of the experiments and simulations.

Fig. 7 shows the comparisons of the selected variables between experimental tests and simulation results with operating conditions i=10 mA, P_d=0.7 MPa. Fig. 8 shows the comparisons with operating conditions i=20 mA, P_d=1.07 MPa.

As shown in Figs. 7 and 8, both experiments and simulations indicate that, before the input signal is ignited, the LS system is in the idle condition, the pump displacement is de-stroked until the delivery flow is nearly zero, which only complements system leakages and used for heat removal. The pump supplies only a lower pressure which is decided by the prescribed pressure margin P_d and the residual pressure of the LS port.

When the input signal is ignited at 1s, the pump delivery pressure P_p increases approximately at a prescribed pressure margin P_d greater than the load pressure P_{ls}, until rising to 12 MPa then the cut-off valve plays a role. As the load rotates, inspection of the variations of the pump pressure and the load speed shown in Fig. 7, an oscillatory process exists at the beginning, then they become stable after the oscillatory process lasting about 3 seconds, which means that the LS system is stable at the operating conditions i=10 mA, P_d=0.7 MPa. In Fig. 8, the oscillatory process will continue, which means that the LS system is in an unstable condition at the operating conditions i=20 mA, P_d=1.07 MPa. Krus **[5]** has proven that the instability of the LS system is critically influenced by the mechanical resonance between load dynamic and pump dynamic.

From the comparisons of pump delivery pressure P_p and load pressure P_{ls} between experimental tests and simulation results, as shown in Fig. 7a and 8a, the model, reflects the characteristic of the LS system which supplies "on-demand" flow at a prescribed pressure margin greater than the load pressure of the system. Furthermore, the comparisons of load speed and displacement as shown in Figs. 7b and c and Figs. 8b and c, indicate that the full bond graph model is a close representation of the actual LS system at the given operating conditions.

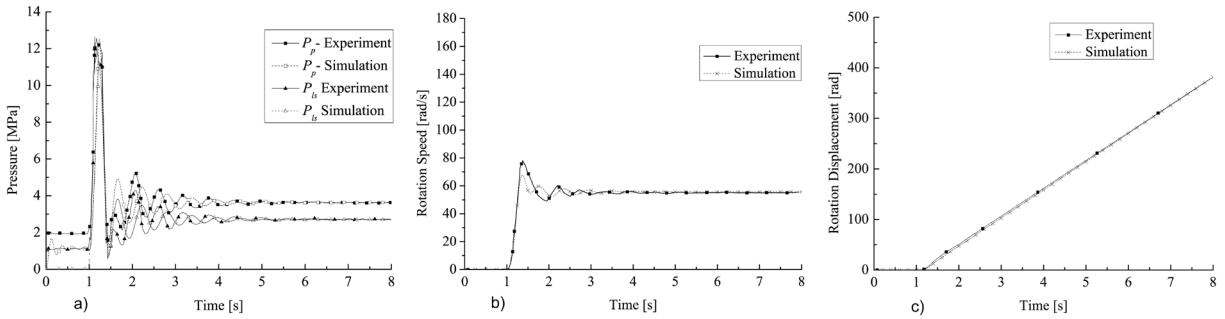

Fig. 7. *Comparisons of experimental tests and simulation results (i = 10 mA, P_d = 0.7 MPa); a) pump delivery pressure and load pressure, b) load speed, c) load displacement*

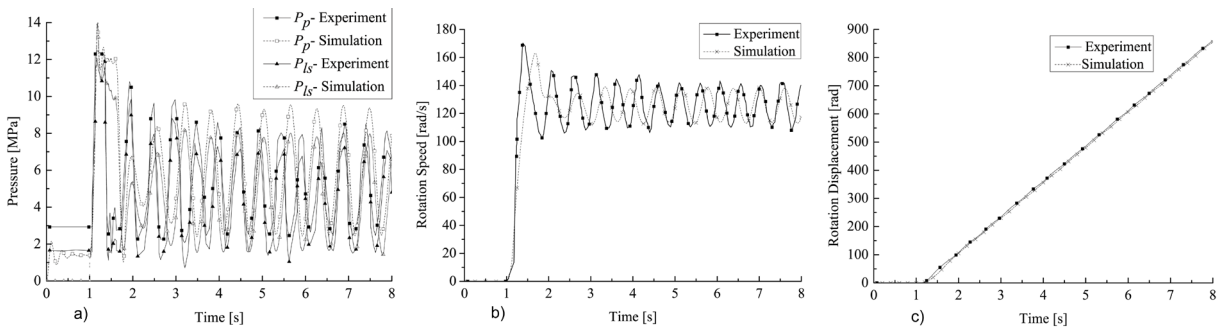

Fig. 8. *Comparisons of experimental tests and simulation results (i = 20 mA, P_d = 1.07 MPa); a) pump delivery pressure and load pressure, b) load speed, c) load displacement*

3 MODEL REDUCTION BASED ON ACTIVITY INDEX ANALYSIS

In the previous section, considering the dynamic characteristics of the LS valve and the cut-off valve, an accurate but overly complex bond graph model of the LS system is obtained. In this section, based on activity index analysis, two reduced models with the different threshold are obtained directly from the bond graph level in order to achieve a balance between accuracy and complexity.

3.1 Theoretical Background

Rosenberg and Zhou proposed a power-based model reduction algorithm **[18]** which would lead to instantaneous and time-varying decisions about the importance of elements. Instead of instantaneous power, Louca and Stein **[20]** proposed the concept of activity, which is defined as the aggregate measure of power flow in or out of an element during the specified time window T. The temporal integration of the absolute power value through an element can be expressed as

$$A_i(t) = \int_{t_0}^{t_0+T} |P(t)| dt = \int_{t_0}^{t_0+T} |e(t) f(t)| dt, \qquad (8)$$

where is $A_i(t)$ the activity of the i^{th} energy element, $e(t)$, $f(t)$ are generalized effort variable and flow variable in the bond, respectively, and T is the specified time window.

In Eq. (8), the time histories of the effort variables $e(t)$ and flow variables $f(t)$ can be obtained for all elements when simulating the bond graph model.

The activity index of the i^{th} element in a submodel is the ratio between the activity of the element to be considered and the total activity of the system, and yields as follows:

$$AI_i = \frac{A_i}{\sum_{total} A_i} \times 100. \qquad (9)$$

The core metric for quantifying the relative importance of the elements for a given system based on activity index analysis is that the most important elements are those characterized by the largest magnitudes of the activity index, which have important contributions to the system dynamic. In contrast, the elements with low activity have small contributions. Thus they are unnecessary to the given scenario and can be eliminated from the model to generate a reduced model.

The procedure of model order reduction algorithm (MORA) based on activity index analysis is shown in Fig. 9.

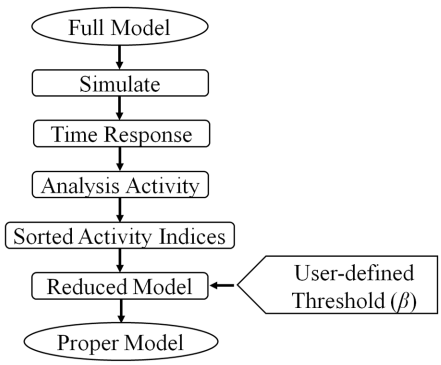

Fig. 9. *Procedure of model order reduction algorithm*

Firstly, the model is simulated, and the time response of the variables in Eq. (8) is available for the activity computation. Then, the activity index for each energy storage and dissipation element is calculated by Eq. (9). Finally, the activity indices are sorted in descending order, the result of the sorting process is the ranking of the element importance. Based on a user-defined threshold β for a specific scenario, the surplus elements with low activity index can be identified and eliminated directly from the bond graph model while retaining sufficiently accurate predictions.

The activity index analysis is an energy-based model reduction method; it is especially suitable for the bond graph models due to the common energy-based nature. Moreover, by analysing the activity index, the model can be simplified directly at the bond graph level.

3.2 Reduced Model

A full bond graph model of the LS system has been constructed, as displayed in Fig. 5, the model has 26 energy storage and dissipation elements, and it is an eleventh-order dynamic system.

The model simulations are carried out with the operating conditions P_d=1.07 MPa and two different input signals, i=20 mA and i=5 mA, the time window T is from 0 s to 8 s, and the user-defined threshold is β=99.5. The differential equation is solved by the BDF solver, and the tolerance error is 0.0001.

The activity index of all the energy storage and dissipation elements are calculated, and the activity indices are sorted according to i=20 mA groups in descending order. The result is listed in Table 2.

By setting the threshold β=99.5, the elements with low activity index, which are less important and can be eliminated from the bond graph model with few effects on the system dynamics, are identified and enclosed in a grey, as shown in Table 2.

Table 2. *Sorting of the activity index*

Energy Element	i = 20 mA		i = 5 mA	
	Activity	AI	Activity	AI
L_p	5247.33	29.43	1825.6	50.67
B_{load}	3245.57	18.20	203.46	5.65
V_p	2564.83	14.38	429.52	11.92
J_{load}	2420.61	13.58	62.74	1.74
R_{ve}	1591.00	8.92	394.11	10.94
R_{sz}	1578.84	8.85	390.47	10.84
MR_3	426.47	2.39	141.37	3.92
L_m	230.18	1.29	18.29	0.51
L_c	164.04	0.92	80.17	2.23
V_{m1}	117.59	0.66	14.85	0.41
MR_1	79.35	0.45	0.00	0.00
MR_2	74.59	0.42	18.78	0.52
V_c	30.94	0.17	1.24	0.03
MR_4	25.910	0.145	5.686	0.158
K_{co}	15.350	0.086	11.493	0.319
J_p	6.804	0.038	0.216	0.006
V_{m2}	6.301	0.035	1.553	0.043
I_{co}	2.695	0.015	2.694	0.075
K_{ls}	0.860	0.005	0.258	0.007
K_p	0.512	0.003	0.059	0.002
B_{co}	0.368	0.002	0.365	0.010
I_{ls}	0.113	0.001	0.042	0.001
B_p	0.106	0.001	0.015	0.000
B_{ls}	0.005	0.000	0.002	0.000
R_{ze}	0.000	0.000	0.000	0.000
R_{sy}	0.000	0.000	0.000	0.000

The components in gray include the inertia, resistance, and capacitance effects of the LS valve, the cut-off valve and the motion dynamic of the swash-plate, respectively, which have smaller contributions to the system dynamics. It proves the rationality representing the LS pump dynamics with a fourth-order differential equation and neglecting the dynamics of the LS valve and the cut-off valve in the literature. Furthermore, the leakage of the pump and motor play important roles in the system dynamics due to its correlation to the damping coefficient.

When determining the eliminated elements among the enclosed elements, MR_4, R_{ze} and R_{sy} are retained in order to keep the bond graph structure in accordance with the topologic structure of the real LS

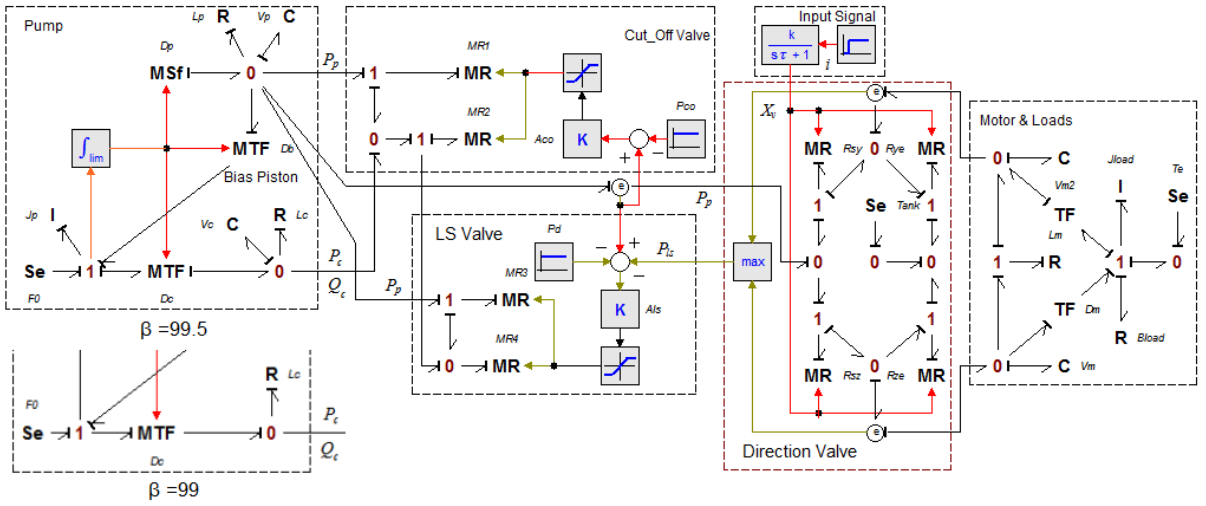

Fig. 10. *The reduced LS system with threshold β = 99.5 and β = 99*

system. J_p is also retained in order to eliminate the derivative causality assigned to the V_c capacitance element which implies the difficulty when solving the differential algebraic equations (DAEs). The elements can be eliminated directly at the bond graph level. Thus, the reduced model with threshold β = 99.5 can be obtained, as shown in Fig. 10.

Now turning to the low activity indices of i = 5 mA, as shown in Table 2, there are intersections of $\{B_p\ B_{ls}\ I_{ls}\ B_{co}\ K_{ls}\ I_{co}\ K_{co}\}$ to be eliminated among the three different operating conditions. This indicates that the reduced bond graph model with threshold β = 99.5 is suitable for the input signal range of i = 5 mA to 20 mA.

Also by setting the threshold β = 99, the elements MR_1, MR_2 and V_c can be eliminated. For the same reason preserving the bond graph structure, MR_1, MR_2 are retained, and V_c is eliminated, because there is no derivative causality assigned to V_c, so J_p can be eliminated. Thus the intersections of $\{B_p\ J_p\ V_c\ B_{ls}\ I_{ls}\ K_{ls}\ B_{co}\ I_{co}\ K_{co}\}$ to be eliminated among the three different operating conditions are listed, and the reduced model with threshold β = 99 is available. Compared to the reduced model with threshold β = 99.5, the model is almost the same; in addition, J_p and V_c are eliminated, as shown in the left corner of Fig. 10.

3.3 Accuracy Assessment and Discussions

To assess the accuracy quantitatively, the average relative error ε is calculated using Eq. (10):

$$\varepsilon = \frac{\int_{t_0}^{t_0+T} |\omega(t) - \omega_r(t)|dt}{\int_{t_0}^{t_0+T} |\omega(t)|dt} \times 100, \tag{10}$$

where $\omega(t)$ is the response of evaluated variable in the full model, and $\omega_r(t)$ is the response of evaluated variable in the reduced model.

In order to assess the accuracy of the reduced bond graph model of the LS system, the important state variables that are easy to measure are selected as the evaluation metrics. In the paper, the dynamic responses of pump delivery pressure P_p, load pressure P_{ls}, load speed and load displacement are selected as the comparison variables of the full model and the reduced model with threshold β=99.5 and β=99, respectively.

Using Eq. (10), the average relative error of pump delivery pressure P_p, load pressure P_{ls}, load speed and load displacement respectively is 1.27%, 1.25%, 0.3%, and 0.13%, when setting threshold β=99.5. While the average relative error respectively is 27.3%, 25.17%, 5.34%, and 0.49%, when setting threshold β=99. The results are shown in Table 3.

In order to visualize the comparisons, the dynamic responses and relative errors of the delivery pressure P_p, load pressure P_{ls}, load speed and load displacement of the full model and the reduced model with threshold β=99.5 and β=99 are compared, the results are shown in Fig. 11.

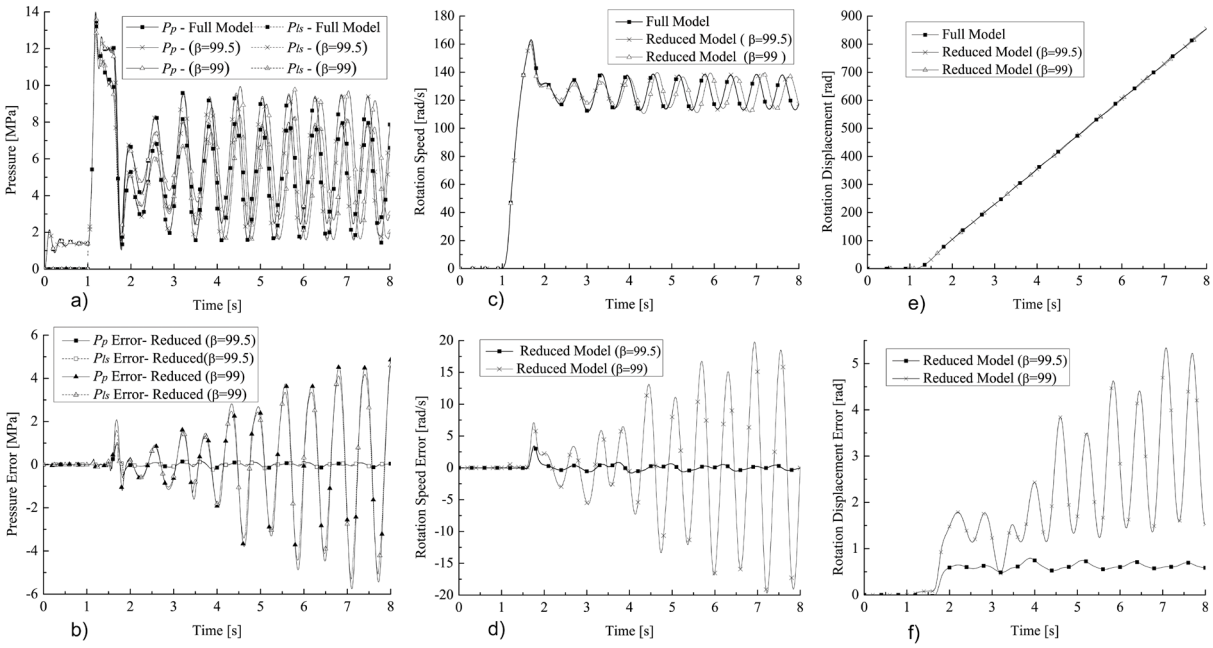

Fig. 11. *Comparisons of full model and reduced models; a) pump delivery pressure and load pressure, b) pressure errors, c) load speed response, d) speed errors, e) load-displacement response, f) displacement errors*

Table 3. *Accuracy level of reduced model [%]*

β	Eliminated Element	P_p Error	P_{ls} Error	Speed Error	Disp. Error
99.5	$B_{ls}\ B_p\ I_{ls}\ B_{co}\ K_{ls}\ I_{co}\ K_{co}$	1.27	1.25	0.30	0.13
99	$B_{ls}\ B_p\ I_{ls}\ B_{co}\ K_{ls}\ I_{co}\ J_p\ K_{co}\ V_c$	27.26	25.17	5.34	0.49

As shown in Table 2, by analysing the activity index, it can be found out that the leakage of the pump and the viscous friction coefficients of the load are the most important parameters to the system dynamics.

Table 4 shows the system order and the computational load in seconds of the full model, and the reduced models with threshold $\beta=99.5$ and $\beta=99$, respectively.

Table 4. *Accuracy level of reduced model*

Model	System order	Computation time [s]
Full	11	3.225
$\beta = 99.5$	7	2.830
$\beta = 99$	4	2.667

4 CONCLUSIONS

Based on the bond graph methodology, an accurate but overly complex eleventh-order bond graph model of the LS system model is constructed, which takes into account the dynamic characteristics of the LS valve and the cut-off valve. A series of experiments are performed to verify the validation of the model, the results of which indicate that the full bond graph model is a close representation of the actual LS system at given operating conditions. Furthermore, compared to the simplified abstract mathematical models, the bond graph model preserves the computational structure and the topological structure of the LS system, and it is convenient to modify the model directly at the graphical representation level.

To simplify the full model of the LS system to achieve a balance between accuracy and complexity, the model reduction technology based on the activity index analysis is used, and two reduced models with threshold $\beta=99.5$ and $\beta=99$ are obtained. The relative error of pump delivery pressure, load pressure, load speed and load displacement is 1.27%, 1.25%, 0.3%, and 0.13%, respectively, when setting the threshold $\beta=99.5$. While the relative error is 27.3%, 25.17%, 5.34%, and 0.49%, respectively, when setting threshold $\beta=99$. Meanwhile, the order of the full system is decreased from eleventh-order to seventh-order and fourth-order respectively, and the computation time is reduced from 3.714 s to 3.236 s and 2.667 s, respectively. Results indicate that the reduced model with threshold $\beta=99.5$ have almost identical predictions for system dynamics.

Furthermore, by quantifying the relative importance of the elements of the LS system based on activity index analysis, it proves the rationality representing the LS pump dynamics with a fourth-order differential equation, and neglecting the dynamics of the LS valve and the cut-off valve in the literature, also the leakage of the pump plays an important role in the system dynamics due to its correlation to the damping coefficient of the LS system.

5 ACKNOWLEDGEMENTS

The authors gratefully acknowledge the support by the National Natural Science Foundation of China through the grant number 51275068.

6 NOMENCLATURES

B equivalent bulk modulus, [Pa]
D_p equivalent bulk modulus of pump, [(m³/s)/rad]
L_p leakage coefficient of the pump, [(m³/s)/Pa]
V_p volume in pump chamber and the line, [m³]
D_b volumetric displacement of bias piston, [m³/rad]
Lc leakage coefficient of control piston, [(m³/s)/Pa]
V_c volume of displacement control piston, [m³]
D_c volumetric displacement of control cylinder, [m³/rad]
G coefficient of displacement control spring, [Nm/rad]
R inertia force of piston and attachments, [Nm/rad]
K_{ls} coefficient of the LS spring, [N/m]
A_{ls} area of the LS valve piston [m²]
K_c flow coefficient of LS & cut-off valve, [m³/(N$^{1/2}$s)]
K_{co} coefficient of cut-off valve spring, [N/m]
A_{co} spool area of cut-off valve, [m²]
K gain of spool displacement [m/A]
τ time constant of the reduce valve, [s]
K_d flow coefficient of direction valve, [(m³/s)/m]
D_m volumetric displacement of motor, [(m³/s)/rad]
L_m leakage coefficient of motor, [(m³/s)/Pa]
V_m volume in motor chamber and the line, [m³]
J moment inertia of motor and loads, [kg·m²]
T_e external torque, [N·m]
B_{load} viscous friction coefficient of the load, [(Nm/rad)/s]

7 REFERENCES

[1] Xu, B., Cheng M., Yang H.Y. (2012). A new electrohydraulic load sensing control system for hydraulic excavators. *Proceedings of the 8th International Fluid Power Conference* vol. 1, p. 553-565.

[2] Carpena, A.G., Hijes, F.C.G.D.E., García, M.A., Moreno, F.M.M. (2015). Checking load sensing valves at vehicle inspections stations. *Mechanics Industry*, vol. 16, no. 3, p. **DOI:10.1051/meca/2015006**.

[3] Backe, W., Zahe, B. (1993). Electrohydraulic loadsensing. Research Projects in Hydraulics. *Fluid Power*, p. 1-27.

[4] Kim, S.D., Cho, H.S. (1991). A suboptimal controller-design method for the energy efficiency of a load-sensing hydraulic servo system. *Journal of Dynamic Systems, Measurement, and Control*, vol. 113, no. 3, p. 487-493, **DOI:10.1115/1.2896436**.

[5] Krus, P. (1988). *On Load Sensing Fluid Power Systems*. Ph.D thesis, no. 198. Linkoping University, Linkoping.

[6] Jayaraman, G.P., Lunzman, S.V. (2011). Modeling and analysis of an electronic load sensing pump. *IEEE International Conference on Control Applications*, **DOI:10.1109/CCA.2011.6044497**.

[7] Axin, M., Eriksson, B., Krus, P. (2014). Flow versus pressure control of pumps in mobile hydraulic systems. *Proceedings of the Institution of Mechanical Engineers, Part I: Journal of Systems and Control Engineering*, vol. 228, no. 4, p. 245-56, **DOI:10.1177/0959651813512820**.

[8] Xu, B., Cheng, M., Yang, H.Y. (2015). A hybrid displacement/pressure control scheme for an electrohydraulic flow matching system. *IEEE/ASME Transactions on Mechatronics*, vol. 20, no. 6, p. 2771-2782, **DOI:10.1109/TMECH.2015.2411315**.

[9] Koivumaki, J., Mattila, J. (2014). Stable and high performance energy-efficient motion control of electric load sensing controlled hydraulic manipulators. *Proceedings of the Asme/Bath Symposium on Fluid Power and Motion Control*, Sarasota.

[10] Wagner, Z.D, Fales, R. (2014). Modeling and stability of a hydraulic load-sensing pump with investigation of a hard nonlinearity in the pump displacement control system. *Proceedings of the Asme/Bath Symposium on Fluid Power and Motion Control*, Bath, **DOI:10.1115/FPMC2014-7802**.

[11] Wu, D. (2003). *Modeling and Experimental Evaluation of a Load-Sensing and Pressure Compensated Hydraulic System*, Ph.D. thesis, University of Saskatchewan, Saskatchewan.

[12] Sakurai, Y. (2000). Calculation of dynamic overall efficiency of a load sensing hydraulic system by bondgraphs. *26th Annual Confjerence of the IEEE Industrial Electronics Society*, vol. 3, p. 1568-1573, **DOI:10.1109/iecon.2000.972508**.

[13] Sakurai, Y., Nakada, T., Tanaka, K. (2002). Design method of an intelligent oil-hydraulic system (load sensing oil-hydraulic system). *Proceedings of the IEEE International Symposium on Intelligent Control*, p. 626-630, **DOI:10.1109/ISIC.2002.1157835**.

[14] Karnopp, D.C., Margolis, D.L., Rosenberg, R.C. (2012). *System Dynamics: Modeling, Simulation, and Control of Mechatronic Systems, 5th rd.*, John Wiley & Sons, New York, **DOI:10.1002/9781118152812.**

[15] Borutzky, W. (2010). *Bond Graph Methodology – Development and Analysis of Multidisciplinary Dynamic System Models*. Springer, London.

[16] Tian, S.J, Hu, Q.Y, Zhang, H. (2012). *Dynamic Simulation of Hydraulic Systems, 2nd ed.* Dalian University of Technology Press, Dalian. (in Chinese)

[17] Ersal, T., Fathy, H.K., Rideout, D.G., Louca, L.S., Stein, J.L. (2008). A review of proper modeling techniques. *Journal of Dynamic Systems, Measurement, and Control*, vol. 130, no. 6, **DOI:10.1115/1.2977484**.

[18] Rosenberg, R.C., Zhou, T. (1988). Power-Based Simplification of Dynamic System Models. *Proceedings of Advances in Design Automation*, Kissimmee, vol. 14, p. 487-492.

[19] Louca, L.S., Stein, J.L., Hulbert, G.M. (2010). Energy-Based Model Reduction Methodology for Automated Modeling. *Journal of Dynamic Systems Measurement and Control*, vol.132, no. 6, **DOI:10.1115/1.4002473**.

[20] Louca, L.S., Stein, J.L. (1998). Physical interpretation of reduced bond graphs. *Proceedings of 2nd IMACS International Multiconference: Computational Engineering in Systems and Applications*, Nabeul-Hammamet.

[21] Ivantysyn, J., Ivantysynova, M. (2001). *Hydrostatic Pumps and Motors: Principles, Design, Performance, Modeling, Analysis, Control and Testing*. India Akademic Books International, New Delhi.

[22] Manring, N.D. (2013). *Fluid Power Pumps and Motors: Analysis, Design and Control*, McGraw-Hill, New York.

List of reviewers who reviewed manuscripts in 2016

Rosminazuin Ab Rahim, Malaysia
Hamidreza Abbasi, Iran
Farid Abed-Meraim, France
Boris Aberšek, Slovenia
Abd Rahim Abu Bakar, Malaysia
Mike Adams, UK
Hafiz Muhammad Ali, Pakistan
Yahia M. Al-Smadi, USA
Sebhi Amar, Algeria
Miha Ambrož, Slovenia
Sanjeev Anand, India
Ciril Arkar, Slovenia
Gianmario Arnulfi, Italia
Fausto Arpino, Italy
Kamil Arslan, Turkey
Viktor P. Astakhov, USA
Ayyanar Athijayamani, India
Azridjal Aziz, Indonesia
Bernd Bachert, Germany
Azhar B. Abu Bakar, Malaysia
Jože Balič, Slovenia
Sebastian Baloš, Serbia
Milan Batista, Slovenia
Branko Bauer, Croatia
Tom Bajcar, Slovenia
Valter Böhm, Germany
Bernd-Arno Behrens, Germany
Mostefa Bendouba, Algeria
Josep M. Bergada, Spain
Tomaž Berlec, Slovenia
Arndt Birkert, Germany
Grega Bizjak, Slovenia
Benjamin Bizjan, Slovenia
Dieter Boer, Spain
Ana Madevska Bogdanova, Macedonia
Gunnar Bolmsjö, Sweden
Miha Boltežar, Slovenia
Éd Claudio Bordinassi, Brazil
Tomaž Brajlih, Slovenia
Kristijan Brecl, Slovenia
Mihael Bruncko, Slovenia
Charles-Henri Bruneau, France
Andreas Bück, Germany
Adam Bureček, Czech Republic
Peter Butala, Slovenia
Vincenc Butala, Slovenia
Miroslav Byrtus, Czech Republic
Michele Calì, Italy
Ken Caluwaerts, USA
Marina Campolo, Italy
Paolo Casoli, Italy
Kadir Cavdar, Turkey
Onur Çavuşoğlu, Turkey
H. Kursat Celik, Turkey
Yikai Chen, China
Peng Cheng, USA
Eliodoro Chiavazzo, Italy
Janusz Tadeusz Cieśliński, Poland
Snezana Ciric-Kostic, Serbia
Roberto Guglielmo Citarella, Italy
Franco Concli, Italy
J. S. Cotton, Canada
Alexander Czinki, Germany
Gregor Čepon, Slovenia
Franci Čuš, Slovenia
Doriana Marilena D'Addona, Italy
José Gilberto Dalfré Filho, Brazil
Jos Darling, UK
J. Paulo Davim, Portugal
Marta Cristina Cardoso de Oliveira, Morocco
Mihael Debevec, Slovenia
Mariusz Deja, Poland
Antonio Del Prete, Italy
Paul A. Dellenback, USA
Cristoforo Demartino, Italy
Jos Derksen, UK
C.J. Deschamps, Brazil
Edvard Deticek, Slovenia
Janez Diaci, Slovenia
Radovan Dražumerič, Slovenia
Mihai Dupac, UK
Pierre Duquesne, Canada
Milan Edl, Slovenia
Igor Emri, Slovenia
Hakan Ersoy, Turkey
Xavier Escaler, Spain
Patrice Estellé, France
Javad Jafari Fesharaki, Iran
Cuneyt Fetvaci, Turkey
Mirko Ficko, Slovenia
Tomasz Figlus, Poland
Rastko Fišer, Slovenia
Anders Flodin, Sweden
Livan Fratini, Italy
Lidia Galda, Poland
Massimo Garai, Italy
Andrés Gabriel García, Argentina
Albert R. George, USA
Hossein Gholizadeh, Canada
Mir Hamid Reza Ghoreishy, Iran
Gilbert-Rainer Gillich, Romania
Srecko Glodez, Slovenia
Patrick Glouannec, France
Sandro Goñi, Argentina
Darko Goričanec, Slovenia
Aleš Gosar, Slovenia
Adriana Greco, Italy
Niccolo Grossi, Italy
Janez Grum, Slovenia
Leo Gusel, Slovenia
Shivakanth Gutta, USA
Virginija Gyliene, Lithuania

The Editorial would like to thank all the reviewers in participating in reviewing process.
We appreciate the time and effort and greatly value the assistance as a manuscript reviewer for Strojniški vestnik – Journal of Mechanical Engineering.

Vsebina

Strojniški vestnik - Journal of Mechanical Engineering
letnik 63, (2017), številka 1
Ljubljana, januar 2017
ISSN 0039-2480

Izhaja mesečno

Razširjeni povzetki (extended abstracts)

Strojniški vestnik - Journal of Mechanical Engineering 63(2017)1, SI 3

Prejeto v recenzijo: 2016-08-24
Prejeto popravljeno: 2016-11-02
Odobreno za objavo: 2016-11-18

Izbira optimalne valčne transformacije za ocenjevanje velikosti napak v izdelavi koničnih kotalnih ležajev z merjenjem vibracij in po kriteriju shannonove entropije

Krisztián Deák* – Tamás Mankovits – Imre Kocsis
Univerza v Debrecenu, Tehniška fakulteta, Madžarska

Odkrivanje napak v izdelavi je ključnega pomena za izboljšanje kakovosti proizvodnje ležajev. Namen članka je analiza možnosti odkrivanja napak v izdelavi koničnih kotalnih ležajev iz signala vibracij ter ugotavljanje geometrijske velikosti napak na zunanjem obroču.

Tradicionalne metode, kot je Fourierjeva transformacija, zaradi posebne narave signalov niso dovolj uspešne pri zaznavanju prehodnih impulzov. Konični kotalni ležaji so le redko predmet znanstvenih člankov, čeprav predstavljajo pomemben del avtomobilskih menjalnikov in sistemov prenosa moči. Večina znanstvenih člankov, ki se ukvarjajo z obrabo, se kljub pomenu te problematike ne posveča težavam pri izdelavi. V članku je zato predstavljena nova rešitev, ki bi jo bilo mogoče učinkovito uporabiti v industriji.

Postopek uporablja valčno transformacijo kot prikladno orodje za analizo signala vibracij ležajev. Transformacija lahko zazna nenadne spremembe in prehodne impulze v signalu, ki se pojavijo zaradi drobnih napak v ležajnih elementih. Analizirani so bili štirje zunanji obroči z napakami pri brušenju različnih velikosti. Primerjanih je devet različnih valčnih transformacij: Symlet-2, Symlet-5, Symlet-8, db02, db06, db10, db14, Meyer in Morlet. Postopki odkrivanja napak na podlagi časovno-frekvenčnih metod se običajno zanašajo na vizualno analizo konturnih grafikonov. Da bi se izognili napakam pri vizualni analizi, je bil v pričujoči raziskavi preučen natančnejši način za določanje najprimernejše valčne transformacije na podlagi razmerja med energijo in Shannonovo entropijo. S Fourierjevo transformacijo se določi glavna frekvenčna vsebina prehodnih impulzov, ki je pomembna za opredelitev srednje frekvence za pravilno primerjavo različnih valčnih transformacij.

Za potrebe študije je bilo zasnovano in postavljeno preizkuševališče z regulacijo hitrosti in visokoločljivostnim sistemom DAQ, namenjeno pravilnemu merjenju značilnih vibracij koničnih kotalnih ležajev. Edinstvena konstrukcija s sistemom za izolacijo vibracij zagotavlja minimalno količino škodljivih vibracij, ki bi lahko motile natančne meritve. Velikost napake je mogoče izračunati iz signala vibracij in glavnih parametrov ležaja. Po večločljivostni analizi (MRA) je bil podrobno analiziran frekvenčni pas prehodnega impulza. Razkrita je bila točka prihoda kotalnega elementa na napako na zunanjem obroču, točka maksimalne razbremenitve napetosti in točka, kjer kotalni element zapusti napako. Eksperimentalno je bilo izmerjenih 20 impulzov in nato so bile za vse štiri zunanje obroče določene povprečne vrednosti časa prihoda, razbremenitve napetosti in odhoda. Tako je bilo pridobljenih 240 podatkovnih točk.

Zaradi preverjanja natančnosti predhodnih meritev je bila uporabljena metoda obdelave slikovnih podatkov za določitev točne geometrične velikosti napake na zunanjem obroču. Sledi brušenja na obročih so bile izmerjene z videomikroskopom Garant MM1-200, za merjenje okroglosti zunanjih obročev in določitev sledi brušenja na obročih pa je bil uporabljen kontaktni instrument za merjenje oblike Mahr MMQ 200. Za učinkovitejšo določitev robov sledi od brušenja sta bila uporabljena algoritma za zaznavanje robov po Prewittu in Soblu, pri čemer se je izkazalo, da je učinkovitejši Prewittov algoritem.

Največje odstopanje v višini 4,12 % za napako širine 0,6311 mm je bilo ugotovljeno pri valčni transformaciji db02. Srednje odstopanje pri transformaciji Symlet-5 je bilo 1,68 %, najboljše srednje odstopanje pa je bilo 1,49 % pri transformaciji Morlet. Transformacija Morlet je tako dala najbolj točno meritev širine iz signala vibracij. Nizek odstotek odstopanja dokazuje uspešnost predstavljene metode in njeno primernost za odkrivanje napak v ležajih med proizvodnjo.

Potrebne bi bile še nadaljnje raziskave na področju analize napak v izdelavi za ostale dele koničnih kotalnih ležajev, kot so notranji obroč in kotalni elementi.

Ključne besede: nadzor stanja, težave v izdelavi, analiza vibracij ležajev, valčna transformacija, entropija, dinamični model, preizkuševališče

*Naslov avtorja za dopisovanje: Univerza v Debrecenu, Tehniška fakulteta, 2-4 Ótemető, 4028 Debrecen, Madžarska, deak.krisztian@eng.unideb.hu

Strojniški vestnik - Journal of Mechanical Engineering 63(2017)1, SI 4

Prejeto v recenzijo: 2016-05-20
Prejeto popravljeno: 2016-08-06
Odobreno za objavo: 2016-09-06

Izboljšanje mazalne sposobnosti RBD palmovega stearina kot alternativnega maziva pri različnih drsnih hitrostih

Nurul Farhanah Azman* – Syahrullail Samion
Malezijska tehniška univerza, Fakulteta za strojništvo, Malezija

Rastlinska olja so pritegnila pozornost strokovnjakov po vsem svetu kot alternativno mazivo, ki bi lahko zmanjšalo odvisnost od naravnih virov pri mazivih na osnovi nafte in s tem pripomoglo k ohranitvi okolja.

Maziva na osnovi nafte so namreč dokazano visokotoksična in niso biorazgradljiva. Rastlinska olja pa imajo kljub svojim ekološkim prednostim le omejeno oksidacijsko in toplotno stabilnost in za uveljavitev palmovega olja kot alternativnega maziva bi bilo treba najprej odpraviti njihove omejitve. Eden od možnih pristopov za zagotavljanje odlične mazalne sposobnosti je mešanje palmovega olja s pravo koncentracijo dodatka cink dialkil ditiofosfat (ZDDP). Če bi bila mazalna sposobnost palmovega olja konkurenčna naftnim oljem, bi lahko zaradi svojih okoljskih prednosti postalo prva izbira za uporabo pri mazivih.

V predstavljeni študiji je bil za osnovno mazivo uporabljen rafiniran, beljen in dezodoriran (RBD) palmov stearin, njegova mazalna sposobnost pa je bila preizkušena s tribometrom v izvedbi konice na disku (čisti aluminij A1100 in disk iz orodnega jekla SKD11) po standardu ASTM G99. RBD palmov stearin kot osnovno mazivo je bil zmešan z 1 ut. %, 3 ut. % in 5 ut. % dodatka ZDDP za izboljšanje mazalne sposobnosti. Za primerjavo je bilo uporabljeno komercialno polsintetično olje (SAE15W50).

Eksperimenti so bili opravljeni na sobni temperaturi pri različnih drsnih hitrostih 1,5 m/s, 2,5 m/s in 3,5 m/s pri normalni sili 9,81 N, trajali pa so eno uro. Mazalna sposobnost preizkušenih maziv je bila ocenjena na osnovi koeficienta trenja, premera sledi obrabe, stopnje obrabe, površinske hrapavosti in obrabljene površine vzorca. Rezultati kažejo, da prisotnost dodatka ZDDP v RBD palmovem stearinu zmanjša trenje in izboljša protiobrabne lastnosti maziva, s povečevanjem koncentracije ZDDP pa se tudi izboljšuje mazalna sposobnost RBD palmovega stearina. Pri RBD palmovem stearinu s 5 ut. % dodatka ZDDP je bil ugotovljen manjši koeficient trenja kot pri olju SAE15W50, medtem ko sta bila premer sledi obrabe in stopnja obrabe nekoliko večja.

Analiza obrabljene površine z optičnim mikroskopom je pokazala, da je dominantni mehanizem obrabe tako pri RBD palmovem stearinu z dodatkom ZDDP in brez dodatka kakor tudi pri olju SAE15W50 abrazivna obraba. Pri čistem RBD palmovem stearinu se pojavljajo znaki oksidacije v obliki temnejših območij na obrabljeni površini. S povečevanjem koncentracije ZDDP se zmanjšuje število abrazivnih raz na obrabljeni površini. Za primerjalno mazivo je bilo uporabljeno olje SAE15W50 zato, da imajo preučevane formulacije na osnovi rastlinskih olj vsaj enake tribološke lastnosti kot avtomobilska motorna olja.

Da bi mazivo na osnovi RBD palmovega stearina lahko postalo konkurenčno v avtomobilski industriji, pa bi bilo treba raziskati tudi njegove ostale lastnosti, npr. oksidacijsko in toplotno stabilnost. To bo tudi predmet prihodnjih raziskav.

Ključne besede: tribometer v izvedbi konice na disku, RBD palmov stearin, ZDDP, koeficient trenja, stopnja obrabe, površinska hrapavost

*Naslov avtorja za dopisovanje: Malezijska tehniška univerza, Fakulteta za strojništvo, 81310 UTM Johor Bahru, Johor, Malezija, nurulfarhanahazman@gmail.com

Strojniški vestnik - Journal of Mechanical Engineering 63(2017)1, SI 5

Prejeto v recenzijo: 2016-02-23
Prejeto popravljeno: 2016-06-01
Odobreno za objavo: 2016-07-14

Linearni in kvadratični telesno-lupinski elementi za kvazistatično in dinamično simulacijo tankostenskih 3D-konstrukcij: uporaba pri postopkih globokega vleka

Peng Wang – Hocine Chalal – Farid Abed-Meraim*
Arts et Métiers ParisTech, LEM3, Francija

Članek podaja predlog za oblikovanje družine linearnih in kvadratičnih telesno-lupinskih elementov, primernih za tridimenzionalno modeliranje tankostenskih konstrukcij v kontekstu kvazistatične (implicitne) in dinamične (eksplicitne) analize, kakor tudi za simulacijo preoblikovanja pločevine.

Tankostenske konstrukcije se tradicionalno modelirajo s konvencionalnimi lupinskimi elementi ali pa s telesnimi elementi nizkega reda. Konvencionalni lupinski elementi so pogosto le omejeno uporabni pri simulacijah različnih procesov preoblikovanja pločevine, pri telesnih elementih kontinuuma pa se pojavljajo težave z blokiranjem. V članku so kot možna rešitev za odpravo naštetih omejitev predstavljeni telesno-lupinski elementi za točno in učinkovito simulacijo tankostenskih konstrukcij. Telesno-lupinski elementi s svojo tridimenzionalno formulacijo združujejo prednosti formulacije teles in lupin za bolj realistično modeliranje različnih konstrukcij, saj se pri formulaciji izognemo geometrijskim (sredinska ravnina) ali kinematičnim domnevam, kakor tudi konstitutivnim (ravninske napetosti) omejitvam.

Formulacija predlagane družine prizmatičnih in heksaedrskih telesno-lupinskih (SHB) elementov v linearni in kvadratični različici uporablja čisti tridimenzionalni pristop, pri katerem edino prostostno stopnjo predstavljajo odmiki. Uvedena je ravninska reducirana integracijska shema s poljubnim številom integracijskih točk po debelini, ki omogoča modeliranje tankostenskih konstrukcij z eno samo plastjo elementov. Elementi SHB so deležni več posebnih obdelav v izogib vsem pojavom blokiranja ter zagotavljajo točnost in učinkovitost simulacij. Ustvarjeni elementi SHB so implementirani v programskem paketu ABAQUS in v namenskih paketih za kvazistatično in dinamično analizo tankostenskih 3D-konstrukcij.

Učinkovitost elementov SHB je najprej ovrednotena z vrsto selektivnih in reprezentančnih statičnih in dinamičnih nelinearnih primerjalnih testov. Predlagani elementi SHB so bili nato uporabljeni za simulacijo globokega vleka cilindrične skodele s kompleksnim nelinearnim potekom obremenitve, anizotropno plastičnostjo in dvostranskim stikom. Numerične simulacije so pokazale, da se rezultati, pridobljeni z elementi SHB, dobro ujemajo z referenčnimi rešitvami pri obeh vrstah analize (kvazistatični in dinamični).

Čeprav se rezultati numerične simulacije postopka globokega vleka cilindrične skodele dobro ujemajo z eksperimenti, bi bilo simulacijo v prihodnje mogoče še izboljšati z uporabo naprednih nekvadratičnih funkcij anizotropične plastičnosti, ki so primernejše za določene materiale, kot so aluminijeve zlitine.

Tehnologija telesno-lupinskih končnih elementov (SHB) s privzetimi deformacijami je v predstavljenem delu razširjena na eksplicitno dinamično analizo ter je povezana z naprednimi anizotropičnimi modeli plastičnosti pri modeliranju tankostenskih tridimenzionalnih konstrukcij, v pogojih kvazistatičnih ali dinamičnih obremenitev, kakor tudi pri procesih preoblikovanja pločevine. Predstavljeni rezultati numeričnih simulacij razkrivajo zmožnosti elementov SHB in dober potencial za njihovo uporabo pri simulaciji tankostenskih 3D-konstrukcij.

Ključne besede: metoda domnevnih deformacij, končni elementi, linearni in kvadratični telesno-lupinski elementi, kvazistatične in dinamične obremenitve, tankostenske 3D-konstrukcije, globoki vlek

*Naslov avtorja za dopisovanje: LEM3, Arts et Métiers ParisTech, 4, rue Augustin Fresnel, 57078 Metz Cedex 03, Francija, farid.abed-meraim@ensam.eu

Strojniški vestnik - Journal of Mechanical Engineering 63(2017)1, SI 6

Prejeto v recenzijo: 2016-04-04
Prejeto popravljeno: 2016-09-12
Odobreno za objavo: 2016-11-29

Robustno in na napake neobčutljivo vodenje avtobusa z elektromotorji v kolesih in minimalno rabo energije pri zavijanju

András Mihály[1,*] – Péter Gáspár[1,2] – Balázs Németh[1,2]

[1]Univerza za tehniko in ekonomijo v Budimpešti, Oddelek za upravljanje transportnih sistemov in vozil, Madžarska
[2]Madžarska akademija znanosti, Institut za računalništvo in upravljanje, Laboratorij za sisteme in upravljanje, Madžarska

Gospodarna in do okolja prijazna cestna vozila postajajo vse bolj priljubljena, raziskave vozil s pogonskimi elektromotorji v kolesih pa v tem kontekstu pridobivajo na pomenu zaradi prednosti te arhitekture. Največja korist od vgradnje pogonskih elektromotorjev v kolesa je v tem, da omogoča snovanje visokoučinkovitih in na napake neobčutljivih krmilnikov gibanja. Štirikolesna vozila z neodvisnimi kolesnimi pogoni (FWIA) so sama po sebi prekrmiljena, zato se pri njih ponujajo širše priložnosti za analizo različnih nalog vodenja.

Namen članka je zasnova na napake neobčutljivega in energijsko optimalnega sistema sledilnega vodenja po trajektoriji za električni avtobus s pogonskimi motorji v kolesih in električnim krmilnim sistemom. Cilj raziskave je predstavitev večkriterijske in rekonfigurabilne metode vodenja, ki je primerna za uporabo pri težkih vozilih s pogonskimi motorji v kolesih. Predstavljena metoda vodenja je usmerjena v zagotavljanje varnosti in gospodarnosti gibanja vozila tudi tedaj, ko nastopijo napake na izvršnih členih. Arhitektura predlaganega krmilnika avtobusu v normalnih pogojih vožnje omogoča izbiro energijsko optimalne delitve med krmilnimi posegi in vektorskim pogonom z neodvisno vodenimi elektromotorji v kolesih, pri čemer je tudi zmanjšan na minimum upor avtobusa proti zavijanju. V primeru zdrsa, napake ali zmanjšane sposobnosti elektromotorjev v kolesih oz. električnega krmilnega sistema se krmilni signali prerazporedijo tako, da avtobus ohrani zmožnost sledenja trajektoriji.

Cilji vodenja so doseženi z visokonivojsko rekonfiguracijo vodenja na podlagi tehnik linearnega spreminjanja parametrov (LPV) in ob uvedbi posebne spremenljivke za energijsko optimalno razporeditev posegov izvršnih členov med normalno vožnjo. V primeru odpovedi kolesnih elektromotorjev ali krmilnega sistema ima prednost krmiljenje ali ustvarjanje diferencialnega momenta. Gospodarno vodenje je zagotovljeno z optimizacijsko metodo, ki zmanjšuje upor avtobusa med zavijanjem, za varno delovanje pa je poskrbljeno z zaznavanjem napak, izolacijskimi filtri in ocenjevanjem kolesne sile.

Novost članka je v predstavljeni metodi rekonfiguracije na podlagi posebne oblike utežnih funkcij pri izbiri izvršnih členov. Ob upoštevanju varnosti in gospodarnosti avtobusa s pogonskimi elektromotorji v kolesih je tako dosežena delitev med krmiljenjem in ustvarjanjem momenta okrog vertikalne osi, ki ustreza dejanskemu gibanju vozila in stanju izvršnih členov. Glavni prispevek v primerjavi z ostalimi sodobnimi metodami je torej v integraciji varnosti in gospodarnosti v isto nadzorno shemo vodenja. Tak pristop je uporaben za praktične aplikacije.

Delovanje predlagane rekonfiguracijske metode je prikazano v okolju programske opreme v zanki (SIL). Dinamika avtobusa je bila simulirana v okolju TruckSim/Simulink, zasnovani visokonivojski krmilnik pa je na podlagi izmerjenih in ocenjenih signalov deloval v napravi dSPACE MicroAutoBox II, elektronski krmilni enoti za hitro izdelavo prototipov. Za komunikacijo med simuliranim vodilom in krmilnikom je bil uporabljen komunikacijski protokol CAN. Ustvarjeno platformo je tako mogoče preprosto predelati v sistem strojne opreme v zanki (HIL) z vključitvijo naprave dSPACE MicroAutoBox II v omrežje CAN fizičnega avtobusa. Rezultati simulacij dokazujejo učinkovitost predlagane metode vodenja s primerjavo dveh scenarijev sledenja trajektoriji, prvega brez napak in drugega s simulirano okvaro kolesnega motorja.

Ključne besede: pogonski motor v kolesu, avtobus FWIA, rekonfigurabilno vodenje, upor pri zavijanju

*Naslov avtorja za dopisovanje: Univerza za tehniko in ekonomijo v Budimpešti, Oddelek za upravljanje transportnih sistemov in vozil, , H-1111 2. Stoczek street, Budapest, Madžarska, mihaly.andras@mail.bme.hu

Strojniški vestnik - Journal of Mechanical Engineering 63(2017)1, SI 7

Prejeto v recenzijo: 2016-06-16
Prejeto popravljeno: 2016-10-20
Odobreno za objavo: 2016-11-03

Raziskava diagnosticiranja napak planetnih gonil na podlagi večskalne fraktalne škatlaste dimenzije CEEMD in ELM

Xihui Chen – Gang Cheng* – Hongyu Li – Yong Li
Kitajska rudarska in tehniška univerza, Šola za mehatroniko, Kitajska

Planetna gonila so razširjena v raznovrstnih pogonih velikih elektromehanskih naprav in predstavljajo najbolj kritični del sistema za prenos moči. Okvare planetnega gonila vplivajo na zanesljivost opreme in lahko privedejo tudi do nesreč, diagnostika okvar planetnih gonil pa je zato pomembno raziskovalno področje.

Predlagana je metoda za diagnosticiranje okvar planetnih gonil na podlagi večskalne fraktalne škatlaste dimenzije empirične dekompozicije oblik s komplementarnimi seti (CEEMD) in nevronske mreže – stroja za ekstremno učenje (ELM). Konstrukcija planetnega gonila je kompleksna in parametri delovanja kot sta hitrost in obremenitev se nenehno spreminjajo, zato je signal vibracij planetnega gonila nestacionaren ter ima lastnosti frekvenčne (FM) in amplitudne modulacije (AM).

Predlagana je uporaba metode CEEMD za dekompozicijo signala vibracij, ki odpravlja problem mešanja oblik in uhajanja energije, problem napake rekonstrukcije pa je ublažen z uporabo komplementarnih parov signalov Gaussovega belega šuma. Pri metodi CEEMD se velik del vibracijskih motenj, ki nastajajo v drugih komponentah prenosnika, in informacije o delovanju planetnega gonila porazdelijo v različne funkcije lastnih oblik (IMF). Le nekatere IMF so povezane z informacijami o delovanju, ki nastanejo zaradi napak planetnega gonila, medtem ko ostale ne vsebujejo želenih informacij. Funkcije IMF, ki nosijo najpomembnejše informacije za odkrivanje napak na planetnih gonilih, se izbirajo po merilu sploščenosti. Rekonstruirani signal je obdelan z večskalno analizo in razdeljen v več signalov na različnih skalah. Nato so s fraktalno škatlasto dimenzijo kvantificirane informacije o lastnostih delovanja v signalih. Ta dimenzija je obenem tudi končni podatek, ki opredeljuje vsako napako. Za točno razlikovanje med različnimi tipi napak pri planetnih gonilih je v tem članku uporabljena metoda ELM, ki omogoča preprosto izbiro parametrov, hitro učenje, dobro generalizacijo in uspešno prepoznavanje različnih napak.

Predlagana metoda za diagnosticiranje napak na planetnih gonilih je bila verificirana eksperimentalno v laboratoriju in v praktični industrijski aplikaciji.

Eksperimenti so pokazali, da je predlagana metoda na podlagi večskalne fraktalne škatlaste dimenzije CEEMD in ELM primerna za ugotavljanje stanja planetnih gonil in uspešna pri diagnosticiranju napak na njih. Sistem za diagnosticiranje napak po predlagani metodi je trenutno ločen od sistema za krmiljenje mehanske opreme, zato bo naslednji korak povezovanje obeh sistemov.

Predlagano metodo za diagnosticiranje napak na planetnih gonilih bi bilo mogoče z določenimi prilagoditvami modela prenesti tudi na druge prenosnike.

Ključne besede: diagnosticiranje napak, planetno gonilo, CEEMD, večskalna analiza, fraktalna škatlasta dimenzija, ELM

*Naslov avtorja za dopisovanje: Kitajska rudarska in tehniška univerza, Šola za mehatroniko, No 1, Daxue Rd. Xuzhou 22116, Jiangsu, Kitajska, chenxh@cumt.edu.cn

Strojniški vestnik - Journal of Mechanical Engineering 63(2017)1, SI 8

Prejeto v recenzijo: 2016-09-03
Prejeto popravljeno: 2016-10-14
Odobreno za objavo: 2016-11-03

Modeliranje histereze dolžine/tlaka pri pnevmatičnih umetnih mišicah po modelu Prandtl-Ishlinskii

Yixiang Liu – Xizhe Zang* – Zhenkun Lin – Xinyu Liu – Jie Zhao
Inštitut za tehnologijo v Harbinu, Državni laboratorij za robotiko in sisteme, Kitajska

Pnevmatične umetne mišice (PAM) so razmeroma nova vrsta elastičnih pnevmatičnih izvršnih členov. Zaradi svoje netogosti ter velikega razmerja med močjo in maso so se uveljavile na različnih področjih uporabe. Njihova naravna nelinearnost, ki vključuje histerezo dolžine/tlaka in histerezo sile/tlaka, pa povečuje sistemsko nelinearnost ter zmanjšuje sposobnost natančnega sledenja. Ena od rešitev za premostitev te težave je postavitev matematičnega modela histereze ter uporaba njegovega inverza za kompenzacijo histereze in doseganje približno linearnega odziva PAM. Članek obravnava modeliranje histereze dolžine/tlaka pri PAM. Histereza dolžine/tlaka se meri z izotoničnim testom ob predpostavki kvazistatičnosti procesa, meritve pa nakazujejo obstoj večje in manjše histerezne zanke med hitrostjo krčenja in notranjm tlakom PAM. Te histerezne zanke so asimetrične ter niso odvisne od manjših zunanjih obremenitev.

Ker je klasični model Prandtl-Ishlinskii učinkovit le pri simetrični histerezi, je za opis histereze dolžine/tlaka predlagan prilagojen model Prandtl-Ishlinskii. Glede na spremembe vhodnih signalov je mogoče celotno histerezno zanko razdeliti na dva dela – na vzpenjajočo se vejo za povečevanje vhoda in na spuščajočo se vejo za zmanjševanje vhoda. Model MPI zato temelji na neodvisnih asimetričnih operatorjih ohlapa za vzpenjajočo in za spuščajočo se vejo. Operatorja ohlapa opisujeta nelinearnost sistema pri vzpenjanju in pri spuščanju, z njunim kombiniranjem pa je mogoče modelirati celotno histerezno zanko. Parametri modela so določeni z rekurzivnim algoritmom najmanjših kvadratov. Primerjava med rezultati simulacij in eksperimentalnimi meritvami je pokazala, da je predlagani model primeren za zelo točno karakterizacijo asimetričnih zank večje in manjše histereze.

Prednost predlaganega modela MPI v primerjavi z obstoječimi modeli histereze je v bolj koncizni matematični obliki, visoki stopnji veljavnosti ter uspešnosti pri reproduciranju asimetrične histereze dolžine/tlaka, vključno z večjo in manjšo histerezno zanko. Model MPI poleg tega omogoča tudi poenostavljeno izpeljavo inverza modela histereze. Le-tega je mogoče določiti neposredno na podlagi meritev po predlaganem modelu MPI, pri čemer hitrost krčenja predstavlja vhod, tlak pa izhod. Ugotovitve nakazujejo, da bi lahko novi model MPI odigral svojo vlogo pri kompenzaciji histereze PAM in zato bo zanimivo preučevati možnosti njegove implementacije pri krmiljenju položaja posameznih PAM in/ali robotskih zgibov, ki so opremljeni s PAM kot izvršnimi členi. V tem delu je preučeno samo kvazistatično histerezno vedenje PAM, saj bi bilo natančno modeliranje dinamične histereze preveč zapleteno. Če se model MPI uporablja pri dinamičnih sistemih, obstajajo različne negotovosti v modelu in zunanje motnje, ki vsekakor vplivajo na njegovo uspešnost. Možna rešitev za omenjeni problem je v uporabi nelinearnega adaptivnega krmiljenja in nelinearnega robustnega krmiljenja. V prihodnje se bomo zato posvetili raziskavam položajnega krmilnika, v katerem bosta združena načelo robustnega povratnozančnega krmiljenja in kompenzacija histereze na osnovi modela MPI za boljše sledenje položaju pri PAM.

Ključne besede: pnevmatične umetne mišice, asimetrična histereza, histereza dolžine/tlaka, kompenzacija histereze, modificiran model Prandtl-Ishlinskii, rekurziven algoritem najmanjših kvadratov

*Naslov avtorja za dopis.: Inštitut za tehnologijo v Harbinu, Državni laboratorij za robotiko in sisteme, 2 Yikuang Street, Harbin 150080, Kitajska, zangxizhe@hit.edu.cn

Strojniški vestnik - Journal of Mechanical Engineering 63(2017)1, SI 9

Prejeto v recenzijo: 2016-01-27
Prejeto popravljeno: 2016-07-11
Odobreno za objavo: 2016-09-15

Analiza indeksa aktivnosti za redukcijo modela hidravličnega sistema z zaznavanjem obremenitve

Quanyi Hu[1,*] – Hong Zhang[1] – Shujun Tian[1] – Xuxin Qin[2]
[1] Tehniška univerza v Dalianu, Fakulteta za strojništvo, Kitajska
[2] Linde Hydraulics GmbH & Co. KG, Nemčija

Hidravlični sistemi z zaznavanjem obremenitve (sistemi LS) so energijsko varčni prenosniki z delovnim fluidom, ki zagotavljajo pretok na zahtevo s specificiranim dodatkom nad tlakom obremenitve. Sistemi LS so nagnjeni k oscilacijam in lahko včasih postanejo nestabilni zaradi povratne zanke mehanizma za zaznavanje obremenitve. Tudi zagotavljanje celotne zmogljivosti ni preprosto zaradi nasprotujočih si zahtev po energijski učinkovitosti in hitrem dinamičnem odzivu, še posebej v širokem razponu obratovalnih pogojev. Snovanje sistemov LS je zato običajno bistveno zahtevnejše kot snovanje konvencionalnih hidravličnih sistemov.

Sistem LS je kompleksen in močno nelinearen sistem, sestavljen iz mehanskih, električnih, hidravličnih in krmilnih podsistemov v interakciji. Za boljši vpogled v zmogljivosti takšnega sistema zato potrebujemo matematični model. Metoda grafa povezav omogoča boljši grafični prikaz za modeliranje multidisciplinarnih dinamičnih tehničnih sistemov. Model z grafom povezav lahko ohrani računsko in topološko zgradbo, omogoča pa tudi sistematično pretvorbo v enačbe stanj, prenosne funkcije, blokovne diagrame, signalne grafe itd.

V članku je predstavljen razvoj modela kompleksnega, nelinearnega sistema LS na osnovi metodologije grafa povezav, ki upošteva dinamiko ventila LS. Opravljena je bila tudi vrsta eksperimentov za validacijo modela. Rezultati eksperimentov kažejo, da model grafa povezav dobro opisuje dejanski sistem LS pri danih obratovalnih pogojih. Model grafa povezav ohranja tudi računsko in topološko zgradbo sistema LS ter je priročno sredstvo za modifikacijo modelov neposredno na ravni grafične ponazoritve.

Vsak dober model mora biti kar se da preprost za dani namen uporabe, postopki modeliranja pa pogosto vodijo do zelo kompleksnih modelov. Reducirani modeli imajo vrsto prednosti pred kompleksnimi modeli. Prvič, reducirani modeli so nižjega reda in zato primernejši za snovanje krmilnikov. Drugič je z njimi lažje dosegljivo ravnovesje med točnostjo modela in hitrostjo računanja. Reducirane modele je tudi lažje pregledovati in fizikalno interpretirati. Takšni modeli so končno tudi lažje obvladljivi zaradi manjšega števila parametrov, ki jih je treba izbrati pri identifikaciji sistema in optimizaciji.

Medtem ko metodologija redukcije modelov na osnovi moči zahteva trenutne in časovno odvisne odločitve o pomembnosti elementov, pa je analiza indeksa aktivnosti metoda redukcije modelov na osnovi energije, ki je še posebej primerna za modele z grafi povezav. Analiza indeksa aktivnosti omogoča poenostavitev modela neposredno na ravni grafa povezav.

V tej raziskavi je bila uporabljena metodologija analize indeksa aktivnosti za poenostavitev celotnega modela LS in pridobljena sta bila dva modela s pragom $\beta = 99{,}5$ in $\beta = 99$. Rezultati kažejo, da modela dosegata želeno ravnovesje med točnostjo in kompleksnostjo. Red sistema je manjši in računski čas je krajši. Kvantifikacija relativnega vpliva elementov na podlagi analize indeksa aktivnosti je pokazala, da ima notranja lekaža v črpalki pomembno vlogo pri dinamiki sistema zaradi svoje korelacije s koeficientom blaženja. Rezultati simulacij kažejo, da ima reducirani model s pragom $\beta = 99{,}5$ praktično identično sposobnost napovedovanja dinamike sistema kot polni model. S tem je dokazana racionalnost opisa dinamike črpalke LS z diferencialnimi enačbami četrtega reda in opustitve dinamike ventila LS, ki ju najdemo v literaturi.

V članku je predstavljen popoln model na osnovi grafa povezav, ki upošteva dinamiko ventila LS in je bil validiran z eksperimenti. Z analizo indeksa aktivnosti sta bila pridobljena dva reducirana modela za ravnovesje med točnostjo in kompleksnostjo. Modela sta praktično uporabna za različne namene, npr. pri snovanju, optimizaciji sistemov in razvoju krmilnih sistemov, saj dajeta boljši vpogled v zmogljivosti sistema LS.

Ključne besede: zaznavanje obremenitve, graf povezav, modeliranje, redukcija modela, indeks aktivnosti, MORA

*Naslov avtorja za dopisovanje: Tehniška univerza v Dalianu, Fakulteta za strojništvo, No.2 Linggong Road, Dalian, Kitajska, hqy281@126.com

DOKTORSKE DISERTACIJE

Na Fakulteti za strojništvo Univerze v Ljubljani je obranil svojo doktorsko disertacijo:

- dne *19. decembra 2016* **Jaka PRIBOŠEK** z naslovom: »Sistem za nadzor topografije površine med laserskimi mikroobdelavami« (mentor: prof. dr. Janez Diaci);

Doktorsko delo obravnava raziskave na področju diagnostike in aplikacij laserskih mikroobdelovalnih procesov. Osredotočeno je na razvoj novih metod in sistemov za brezdotični zajem oblike površine med laserskimi obdelavami. Kot ključni del tovrstnih metod je bila pri tem razvita izvirna tehnologija izdelave mikrooptičnih elementov ter lasten adaptivno-optični sistem, na osnovi piezoelektričnih deformabilnih zrcal. Na osnovi obeh podsistemov smo razvili dva izvirna konfokalna merilna sistema. Prvi temelji na prostorskem multipleksiranju, ki omogoča merjenje topografije obdelovancev na polnem polju, brez potrebe po rastrskem vodenju v prečni smeri. Drugi temelji na izvirnem konceptu časovno-prostorskega kodiranja optične zaslonke, ki omogoča sočasno izmero naklona in položaja površine. Za analizo tovrstnih sistemov smo razvili lastno orodje za valovnooptične simulacije v neparaksialni aproksimaciji. Izvedljivost obeh predlaganih sistemov smo preverili eksperimentalno.

*

Na Fakulteti za strojništvo Univerze v Mariboru je obranil svojo doktorsko disertacijo:

- dne *16. decembra 2016* **Zlatko BOTAK** z naslovom: »Inteligentni sistem za večkriterijsko optimizacijo tehnološkega načrta dvoosnega struženja« (mentor: prof. dr. Jože Balič);

Obdelovalni proces je pod stalnim vplivom razvoja in posodabljanja komponent v sistemu stroj-orodje-obdelovanec. Bolj kot so poznana zapletena razmerja med vhodnimi in izhodnimi veličinami, uspešnejši je končni rezultat obdelave s tehničnega in ekonomskega vidika. Obdelava množice medsebojno odvisnih podatkov in omejitev v realnem procesu s klasičnimi metodami ni več primerna, temveč se za optimizacijo poskuša narediti model, ki vključuje določeno stopnjo umetne inteligence.

V disertaciji je predstavljen model inteligentnega sistema za samodejno programiranje obdelave struženja na rotacijskih izdelkih. Sistem je zmožen na osnovi 3D-modela izdelka samostojno prepoznati izdelovalnost s postopkom dvoosnega struženja, določiti obdelovalna orodja, zaporedje obdelave, izvesti optimalizacijo in pripraviti NC-program.

Nastali NC-program bo glede na izbrane kriterije optimalen glede na čas in učinkovitost obdelave. Razviti inteligentni sistem deluje popolnoma samostojno, brez posega izkušenega strokovnjaka v potek priprave tehnologije. Obdelava se sočasno optimalizira po več kriterijih, po odrezovalnem času, odvzemu materiala, strošku orodja in številu prehodov orodja. Kriteriji se merijo v različnih enotah in se pogosto medsebojno izključujejo, kar pomeni, da izboljšanje obdelave po enem kriteriju pripelje do poslabšanja po drugem.

V sistem za samodejno programiranje obdelave je vključena metoda za večkriterijsko optimiranje, analitični hierarhični proces. Metoda temelji razčlenjevanju problema na več ravni, primerjavi kriterijev po parih, izračun vpliva posamezne alternative na končni cilj in preverjanje doslednosti. Rezultati so dodatno preverjeni z metodo za večkriterijsko odločanje ELECTRE II in programom SuperDecisions.

Predstavljeni model se lahko uporabi za analizo in optimalizacijo realnih problemov obdelave s struženjem v praksi.

Information for Authors

All manuscripts must be in English. Pages should be numbered sequentially. The manuscript should be composed in accordance with the Article Template given above. The maximum length of contributions is 10 pages. Longer contributions will only be accepted if authors provide juastification in a cover letter. For full instructions see the Information for Authors section on the journal's website: http://en.sv-jme.eu .

SUBMISSION:

Submission to SV-JME is made with the implicit understanding that neither the manuscript nor the essence of its content has been published previously either in whole or in part and that it is not being considered for publication elsewhere. All the listed authors should have agreed on the content and the corresponding (submitting) author is responsible for having ensured that this agreement has been reached. The acceptance of an article is based entirely on its scientific merit, as judged by peer review. Scientific articles comprising simulations only will not be accepted for publication; simulations must be accompanied by experimental results carried out to confirm or deny the accuracy of the simulation. Every manuscript submitted to the SV-JME undergoes a peer-review process.

The authors are kindly invited to submit the paper through our web site: http://ojs.sv-jme.eu. The Author is able to track the submission through the editorial process - as well as participate in the copyediting and proofreading of submissions accepted for publication - by logging in, and using the username and password provided.

SUBMISSION CONTENT:

The typical submission material consists of:

- A **manuscript** (A PDF file, with title, all authors with affiliations, abstract, keywords, highlights, inserted figures and tables and references),
- Supplementary files:
  - a **manuscript** in a WORD file format
  - a **cover letter** (please see instructions for composing the cover letter)
  - a ZIP file containing **figures** in high resolution in one of the graphical formats (please see instructions for preparing the figure files)
  - possible **appendicies** (optional), cover materials, video materials, etc.

Incomplete or improperly prepared submissions will be rejected with explanatory comments provided. In this case we will kindly ask the authors to carefully read the Information for Authors and to resubmit their manuscripts taking into consideration our comments.

COVER LETTER INSTRUCTIONS:

Please add a **cover letter** stating the following information about the submitted paper:

1. Paper **title**, list of **authors** and their **affiliations**.
2. **Type of paper**: original scientific paper (1.01), review scientific paper (1.02) or short scientific paper (1.03).
3. A **declaration** that neither the manuscript nor the essence of its content has been published in whole or in part previously and that it is not being considered for publication elsewhere.
4. State the **value of the paper** or its practical, theoretical and scientific implications. What is new in the paper with respect to the state-of-the-art in the published papers? Do not repeat the content of your abstract for this purpose.
5. We kindly ask you to suggest at least two **reviewers** for your paper and give us their names, their full affiliation and contact information, and their scientific research interest. The suggested reviewers should have at least two relevant references (with an impact factor) to the scientific field concerned; they should not be from the same country as the authors and should have no close connection with the authors.

FORMAT OF THE MANUSCRIPT:

The manuscript should be composed in accordance with the Article Template. The manuscript should be written in the following format:

- A **Title** that adequately describes the content of the manuscript.
- A list of **Authors** and their **affiliations**.
- An **Abstract** that should not exceed 250 words. The Abstract should state the principal objectives and the scope of the investigation, as well as the methodology employed. It should summarize the results and state the principal conclusions.
- 4 to 6 significant **key words** should follow the abstract to aid indexing.
- 4 to 6 **highlights;** a short collection of bullet points that convey the core findings and provide readers with a quick textual overview of the article. These four to six bullet points should describe the essence of the research (e.g. results or conclusions) and highlight what is distinctive about it.
- An **Introduction** that should provide a review of recent literature and sufficient background information to allow the results of the article to be understood and evaluated.
- A **Methods** section detailing the theoretical or experimental methods used.
- An **Experimental section** that should provide details of the experimental set-up and the methods used to obtain the results.
- A **Results** section that should clearly and concisely present the data, using figures and tables where appropriate.
- A **Discussion** section that should describe the relationships and generalizations shown by the results and discuss the significance of the results, making comparisons with previously published work. (It may be appropriate to combine the Results and Discussion sections into a single section to improve clarity.)
- A **Conclusions** section that should present one or more conclusions drawn from the results and subsequent discussion and should not duplicate the Abstract.
- **Acknowledgement** (optional) of collaboration or preparation assistance may be included. Please note the source of funding for the research.
- **Nomenclature** (optional). Papers with many symbols should have a nomenclature that defines all symbols with units, inserted above the references. If one is used, it must contain all the symbols used in the manuscript and the definitions should not be repeated in the text. In all cases, identify the symbols used if they are not widely recognized in the profession. Define acronyms in the text, not in the nomenclature.
- **References** must be cited consecutively in the text using square brackets [1] and collected together in a reference list at the end of the manuscript.
- **Appendix(-icies)** if any.

SPECIAL NOTES

Units: The SI system of units for nomenclature, symbols and abbreviations should be followed closely. Symbols for physical quantities in the text should be written in italics (e.g. *v*, *T*, *n*, etc.). Symbols for units that consist of letters should be in plain text (e.g. ms^{-1}, K, min, mm, etc.). Please also see: http://physics.nist.gov/cuu/pdf/sp811.pdf .

Abbreviations should be spelt out in full on first appearance followed by the abbreviation in parentheses, e.g. variable time geometry (VTG). The meaning of symbols and units belonging to symbols should be explained in each case or cited in a **nomenclature** section at the end of the manuscript before the References.

Figures (figures, graphs, illustrations digital images, photographs) must be cited in consecutive numerical order in the text and referred to in both the text and the captions as Fig. 1, Fig. 2, etc. Figures should be prepared without borders and on white grounding and should be sent separately in their original formats. If a figure is composed of several parts, please mark each part with a), b), c), etc. and provide an explanation for each part in Figure caption. The caption should be self-explanatory. Letters and numbers should be readable (Arial or Times New Roman, min 6 pt with equal sizes and fonts in all figures). Graphics (submitted as supplementary files) may be exported in resolution good enough for printing (min. 300 dpi) in any common format, e.g. TIFF, BMP or JPG, PDF and should be named Fig1.jpg, Fig2.tif, etc. However, graphs and line drawings should be prepared as vector images, e.g. CDR, AI. Multi-curve graphs should have individual curves marked with a symbol or otherwise provide distinguishing differences using, for example, different thicknesses or dashing.

Tables should carry separate titles and must be numbered in consecutive numerical order in the text and referred to in both the text and the captions as Table 1, Table 2, etc. In addition to the physical quantities, such as *t* (in italics), the units [s] (normal text) should be added in square brackets. Tables should not duplicate data found elsewhere in the manuscript. Tables should be prepared using a table editor and not inserted as a graphic.

REFERENCES:

A reference list must be included using the following information as a guide. Only cited text references are to be included. Each reference is to be referred to in the text by a number enclosed in a square bracket (i.e. [3] or [2] to [4] for more references; do not combine more than 3 references, explain each). No reference to the author is necessary.

References must be numbered and ordered according to where they are first mentioned in the paper, not alphabetically. All references must be complete and accurate. Please add DOI code when available. Examples follow.

Journal Papers:

Surname 1, Initials, Surname 2, Initials (year). Title. Journal, volume, number, pages, DOI code.

[1] Hackenschmidt, R., Alber-Laukant, B., Rieg, F. (2010). Simulating nonlinear materials under centrifugal forces by using intelligent cross-linked simulations. *Strojniški vestnik - Journal of Mechanical Engineering,* vol. 57, no. 7-8, p. 531-538, DOI:10.5545/sv-jme.2011.013.

Journal titles should not be abbreviated. Note that journal title is set in italics.

Books:

Surname 1, Initials, Surname 2, Initials (year). Title. Publisher, place of publication.

[2] Groover, M.P. (2007). *Fundamentals of Modern Manufacturing*. John Wiley & Sons, Hoboken.

Note that the title of the book is italicized.

Chapters in Books:

Surname 1, Initials, Surname 2, Initials (year). Chapter title. Editor(s) of book, book title. Publisher, place of publication, pages.

[3] Carbone, G., Ceccarelli, M. (2005). Legged robotic systems. Kordić, V., Lazinica, A., Merdan, M. (Eds.), Cutting Edge Robotics. Pro literatur Verlag, Mammendorf, p. 553-576.

Proceedings Papers:

Surname 1, Initials, Surname 2, Initials (year). Paper title. Proceedings title, pages.

[4] Štefanić, N., Martinčević-Mikić, S., Tošanović, N. (2009). Applied lean system in process industry. *MOTSP Conference Proceedings*, p. 422-427.

Standards:

Standard-Code (year). Title. Organisation. Place.

[5] ISO/DIS 16000-6.2:2002. *Indoor Air – Part 6: Determination of Volatile Organic Compounds in Indoor and Chamber Air by Active Sampling on TENAX TA Sorbent, Thermal Desorption and Gas Chromatography using MSD/FID.* International Organization for Standardization. Geneva.

WWW pages:

Surname, Initials or Company name. Title, from http://address, date of access.

[6] Rockwell Automation. Arena, from *http://www.arenasimulation.com,* accessed on 2009-09-07.

EXTENDED ABSTRACT:

When the paper is accepted for publishing, the authors will be requested to send an **extended abstract** (approx. one A4 page or 3500 to 4000 characters). The instruction for composing the extended abstract are published on-line: http://www.sv-jme.eu/information-for-authors/ .

COPYRIGHT:

Authors submitting a manuscript do so on the understanding that the work has not been published before, is not being considered for publication elsewhere and has been read and approved by all authors. The submission of the manuscript by the authors means that the authors automatically agree to transfer copyright to SV-JME when the manuscript is accepted for publication. All accepted manuscripts must be accompanied by a Copyright Transfer Agreement, which should be sent to the editor. The work should be original work by the authors and not be published elsewhere in any language without the written consent of the publisher. The proof will be sent to the author showing the final layout of the article. Proof correction must be minimal and executed quickly. Thus it is essential that manuscripts are accurate when submitted. Authors can track the status of their accepted articles on http://en.sv-jme.eu/.

PUBLICATION FEE:

Authors will be asked to pay a publication fee for each article prior to the article appearing in the journal. However, this fee only needs to be paid after the article has been accepted for publishing. The fee is 240.00 EUR (for articles with maximum of 6 pages), 300.00 EUR (for articles with maximum of 10 pages), plus 30.00 EUR for each additional page. The additional cost for a color page is 90.00 EUR. These fees do not include tax.

Strojniški vestnik -Journal of Mechanical Engineering
Aškerčeva 6, 1000 Ljubljana, Slovenia,
e-mail: info@sv-jme.eu

9 770039 248001
ISSN 0039-2480

http://www.sv-jme.eu

Contents

Papers